To the Graduate Council:

I am submitting herewith a dissertation written by Toshiyuki Misu entitled "*Deformation Properties of Drip-Line Nuclei*". I have examined the final copy of this dissertation for form and content and recommended that it be accepted in partial fulfillment of the requirements for the degree of Doctor of Philosophy, with a major in Physics.

Witold Nazarewicz

Witold Nazarewicz, Major Professor

We have read this dissertation
and recommend its acceptance:

M W Guidry

Lee L. Riedinger

Carrol Bingham

Robert N. Compton

Accepted for the Council:

Cunninghame

Associate Vice Chancellor and
Dean of The Graduate School

# Deformation Properties
# of
# Drip-Line Nuclei

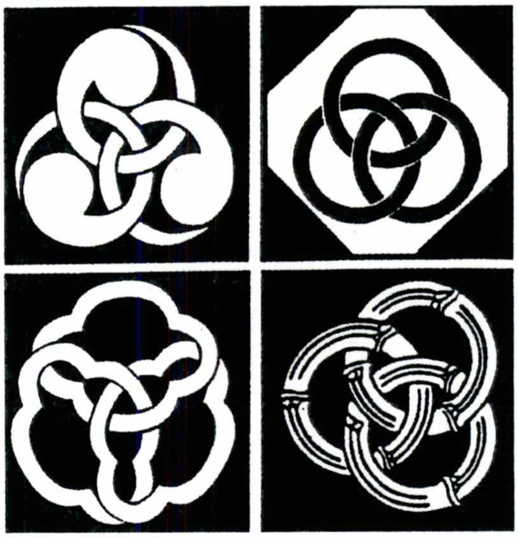

A Dissertation
Presented for the
Doctor of Philosophy
Degree

The University of Tennessee, Knoxville

TOSHIYUKI MISU
May 1997

*To*

*Chieko Misu, My Mother who is now in heaven sharing my joy*

*Hisato Misu, My Father who tought me the values and who hopes for my prosperity*

*Friends all across the nation and overseas who believe in my sincerity*

心

# Acknowledgments

Without the help of many individuals, I would not have been able to accomplish this academic goal. First, I would like to express my cordial thanks to my mentor Dr. W. Nazarewicz, for his endurance and guidance. It has been my pleasure to know him personally and learn the essence of physics from him. I would also like to thank my committee members, Dr. L. L. Riedinger, Dr. C. R. Bingham, Dr. M. W. Guidry, and Dr. R. N. Compton, for sharing their valuable time to support my advancement. I appreciate the support from my colleagues (especially, Bradley Smith, Wilhelm Mueller, and Shoujirou Mizutori) and the staff members of the nuclear physics group from the University of Tennessee at Knoxville and Oak Ridge National Laboratory. They have provided me with a wonderful and friendly environment.

My friends here in Knoxville have also been very supportive. I am grateful to Raymond Igharas for his helpful suggestions regarding my dissertation, Kandace Cody for comforting me throughout my stay in Knoxville, Winifred Ilic, Elizabeth Shaver, Boung Ditavong, Kara Gardner, Momi Yamanaka, the Knoxville Zoo personnel, and those who studied and laughed with me at U.T.K. I would also like to thank people across the nation and overseas: David Brown from Colorado and Ronald Pitner from Michigan for being my best friends, Mr. & Mrs. Heller in Colorado for giving me a first taste of American culture, Lori-Beth Jinkins of France for encouraging me to become an artist, Mendy Chu from Atlanta, Kimberly Goddard from Memphis, Keiko Sumiyoshi and Shuko Umetani in Japan, and all of my other friends who have supported me.

Lastly, I would deeply like to acknowledge my family members in Japan for giving me the opportunity to study at the University of Tennessee, Knoxville.

# Abstract

Deformation properties of weakly bound drip-line nuclei are discussed in the deformed single-particle model and, in particular, those of the drip-line sulfur isotopes are investigated in the framework of the self-consistent mean-field theory. In the deformed single-particle model, it is demonstrated that in the limit of very small binding energy the valence particles in specific orbitals, characterized by a very small projection of single-particle angular momentum onto the symmetry axis of a nucleus, can give rise to the halo structure which is completely decoupled from the rest of the system. The quadrupole deformation of the resulting halo is completely determined by the intrinsic structure of a weakly bound orbital, irrespective of the shape of the core. Similarly, the self-consistent mean-field calculations show large differences between the proton and neutron quadrupole deformations in the drip-line sulfur isotopes, which can be understood in terms of the significant radial contribution to the quadrupole moment in such spatially extended systems.

# Table of Contents

**Chapter**

# List of Figures

# Chapter 1

# Shapes and Forces

Shapes of physical objects range from most symmetric spherical ones to extremely irregular forms. From a scientific point of view, shapes of natural objects are governed by the laws of *physics* and reflect properties of basic interactions. Identification of a shape is often the first step towards better understanding of the underlying physical mechanisms. In this manuscript, which concentrates on properties of exotic nuclei, the concept of shape is explored in the language of nuclear physics.

Before approaching the realm of the actual nuclei, we first discuss the shapes of various physical objects found in nature. The link between shapes and forces is demonstrated through simple examples. The main objective of this introductory chapter is to stress the significance of shape deformations and their connections to the underlying physics.

Let us first consider an instructive example taken from our everyday life: soap bubbles. When we examine one soap bubble, we see it as a perfect sphere. This simplest form of a single soap bubble can be disturbed by adding other soap bubbles. For instance, if a second soap bubble is attached to the first bubble of the same size, a thin soap film would separate the two bubbles at the center, and the overall shape would resemble a 'snowman'. When four bubbles are joined together, they form a tetrahedron [1]. For a large number of soap bubbles of different sizes joined together, the overall shape becomes very complex. This shape change is, however, a simple consequence of the physical principle that a physical system seeks the shape minimizing its (surface) energy. In particular, shape changes of soap films have been the show-case model for the study of minimal surfaces [2]. Here a variety of applications have been found: the design of the roof of the Olympic Stadium in Munich, topological studies of minimal surfaces in mathematics, and the crystal formation in metals [1, 3, 4]. Many clustering phenomena reflecting the principle of minimal surfaces have been found in nuclear and molecular physics.

Moving to the microscopic world, the atomic model proposed by Lord Kelvin in 1867, generated a wide-spread interest not only in the field of fluid dynamics but also in mathematics. Based on the famous Helmholtz vorticity theorem and the remarkable experiments on smoke rings demonstrated by Tait, Lord Kelvin was convinced that the local disturbance (vortex ring) within a homogeneous ether was a good representation of atoms [5-7]. Because of the geometric shape of a ring, the properties of a vortex ring and the interaction between two vortex rings meet the physical descriptions of atoms. Under the vortex-atom hypothesis, Tait investigated various types of knotted and linked vortex rings to describe the differences in physical properties of chemical compounds [8] (see Fig. 1.1). This was one of the earliest

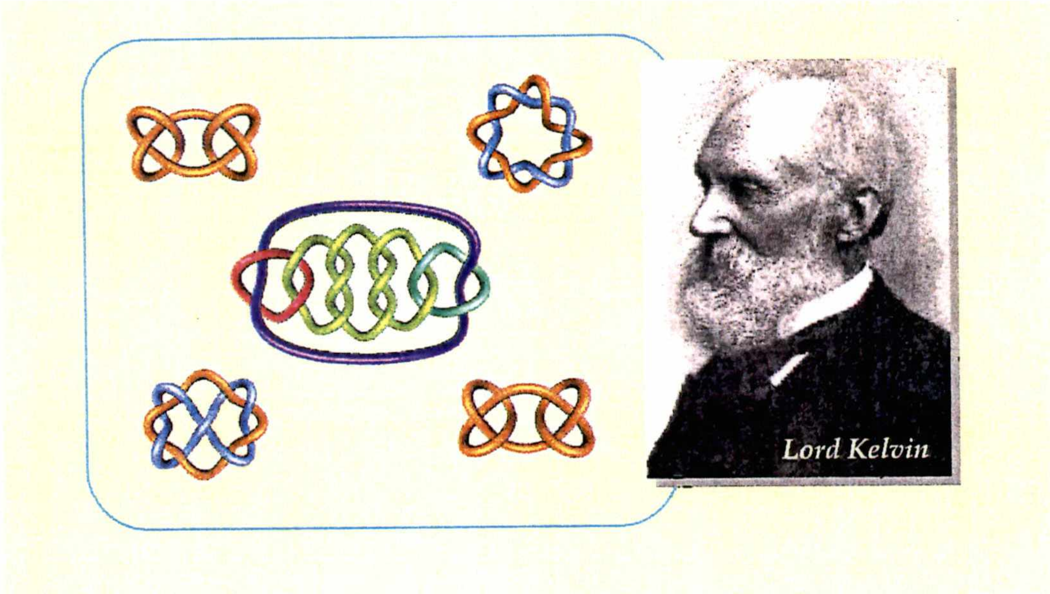


**Figure 1.1**: Lord Kelvin and various types of knotted and linked vortex rings.

attempts in the history of physics to unify all known physical phenomena, including electrical, chemical, and gravitational forces. Although today Lord Kelvin's atomic theory has only historical significance, it is interesting to note that its simple geometric structure has many striking similarities with the superstring theory [7, 9]. The intensive studies of the geometry of knotted rings opened up a new field in mathematics, the so-called knot theory, and their importance has been recognized in several scientific communities (e.g., synthesis of new chemical compounds, DNA research, quantum field theory [1, 10, 11]).

Throughout the history of science, shapes of macroscopic objects have been crucial for identifying fundamental laws of physics and for testing the validity of existing physical theories. One of the most famous examples is the dispute over the shape of the Earth in the Newtonian era. While, according to the Cartesian vortex theory, the shape of the Earth was to be prolate, the Newtonian theory predicted the oblate form as mathematically shown by Maupertuis (see Fig. 1.2). According to Maupertuis' investigation, a rotating liquid governed by any type of attractive force took an oblate-type spheroidal shape. The controversy about the shape of the Earth was later resolved by Maupertuis' famous geodetic measurement in Swedish Lapland in favor of Newton [12, 13].

Later on, the success of Newtonian mechanics guided Laplace to propose his famous nebular hypothesis of the origin of the Solar system. During this period, all the known planets and asteroids revolving around the Sun were observed to move from west to east. To explain such a collective vertical motion of the planets against the Sun's gravitational pull, a great German philosopher Kant invoked the existence of some (unknown) repulsive force. Laplace rejected Kant's hypothesis and

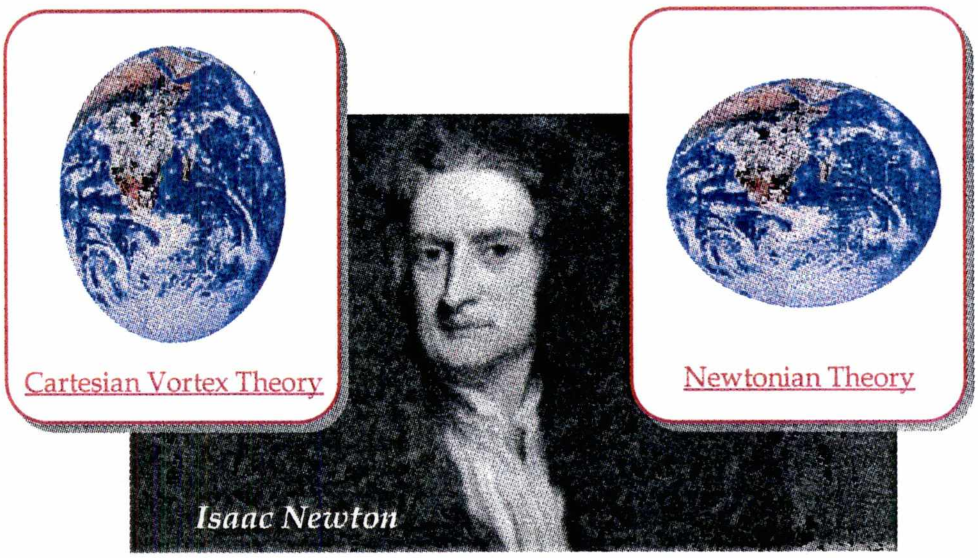


**Figure 1.2**: Newton and two theoretical predictions regarding the shape of the Earth. Left: Prolate form (or 'egg' shape) predicted by the Cartesian vortex theory. Right: Oblate form (or 'tomato' shape) predicted by the Newtonian theory.

suggested that the circular motion of planets was a remnant of the ancient formation process of our Solar system; the presence of the attractive gravitational force should be sufficient to account for the circular motion [12]. His model of the simultaneous formation of the Sun and its planets from a rotating gaseous cloud is the foundation of today's astronomy. Laplace's picture of evolutionary universe can be extended to explain the circular motions of galaxies and galaxy clusters. Conceivably, although there appears to be no clear indication of the rotational character in a vast supercluster (of a diameter of more than a billion light-years)[14, 15], the complex irregular form of a supercluster can also be understood from the picture proposed by Laplace.

The above discussion illustrates the inevitable correlation between shapes and the corresponding physical forces. For instance, shapes of macroscopic objects such as planets and galaxies are explained by means of the interplay between the gravitational force and the rotation-induced forces. The four known fundamental forces (excluding the hypothetical existence of the 5th and 6th forces [16]), which govern our universe, differ dramatically in their strengths and interaction ranges. It seems, however, that nature establishes some common ground for all sizes. In this context, a universal relation between the typical rotational period and dimension of various rotational objects was presented in Ref. [17] (see also Fig. 1.3). Interestingly, the typical rotational period $T$ and the characteristic dimension $L$ of a rotating object cluster along a line $T \approx 10^{-7} L^{1.09}$, where $T$ is expressed in sec and $L$ in cm.

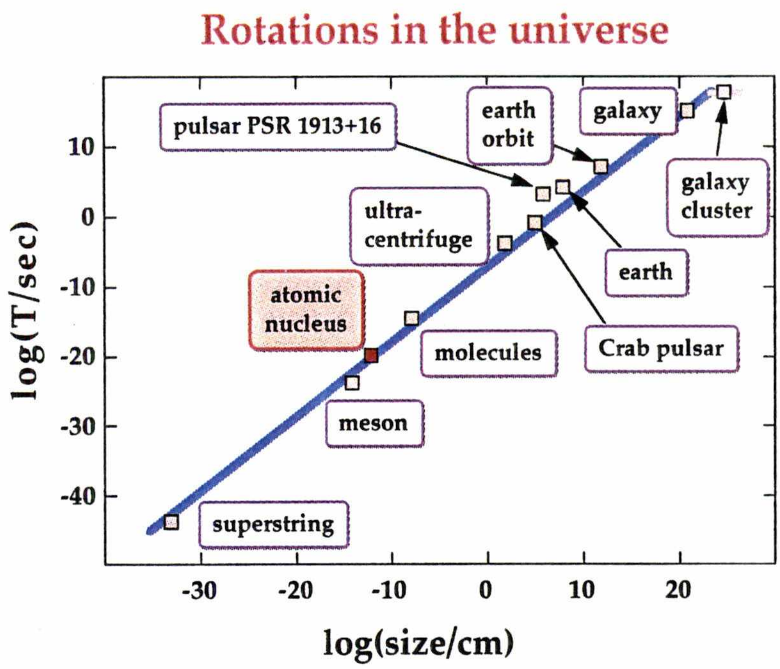


**Figure 1.3**: Typical period of rotation versus characteristic dimension of a rotating object [17].

In nuclear physics, shape deformations also play a significant role. They reflect properties of effective interactions acting between nucleons, and reflect the resulting shell effects. An example which nicely illustrates a correlation between nuclear shapes and the underlying forces is a rotating nuclear liquid drop. At low rotational frequencies, the shape of a liquid drop is oblate, while it can be triaxial or prolate at higher frequencies. It is the interplay between the Coulomb force and surface tension which is responsible for the rotation-induced shape change.

Recent experimental results on exotic nuclei close to the particle drip lines revealed many holes in our understanding of the nuclear many-body problem. In the new regime of a very weak binding, the well-established concept of shape deformations needs to be modified. The main objective of this study is to investigate the impact of weak binding on deformation properties of drip-line nuclei. Consequently, this study also raises the question regarding the concept of shape deformations in the weakly bound systems.

This manuscript is organized as follows: Chapter 2 briefly reviews the emerging field of exotic nuclei. The generic aspects of deformed halos are discussed in Chapter 3. Chapter 4 offers a closer look at some of the physical observables in deformed halos through a simple theoretical model based on the finite spheroidal potential. In Chapters 5 and 6, the deformation properties of drip-line nuclei are examined in the framework of the self-consistent mean-field approach. These microscopic results nicely illustrate the interplay between the weak binding and intrinsic deformation.

# Chapter 2

# New Regime of Nuclear Structure: Particle Drip Lines

The search for yet observed nuclear elements far from the valley of beta stability is an ongoing challenge for the nuclear physics community. In contrast to nuclear structure along the beta-stability line which has been well studied both experimentally and theoretically, the nuclei near particle drip lines with extreme-isospin excess reveal the variety of new physical phenomena that cannot be explained by conventional nuclear models. From a theoretical point of view, spectroscopy of exotic nuclei offers a unique test of those components of nuclear effective interactions that depend on isospin degrees of freedom. Many experimental facilities around the world, including the Holifield Radioactive Ion Beam Facility (HRIBF) at Oak Ridge National Laboratory, are currently searching for nuclear exotica. The recent experimental progress in the radioactive nuclear ion beam (RNB) technology enables us to investigate various physical properties of exotic nuclei [18].

One of the well-known features of nuclei far from stability is the large spatial extension of matter density, well beyond the typical size for the stable nuclei. In this context, two phenomena have currently attracted our attention, namely the nuclear *halo* and neutron *skin*. While the nuclear halo is the direct result of the small binding energy of valence nucleon(s), neutron skin can be associated with the large isospin excess. Although it is difficult to draw a clear boundary between nuclear skin and halo, one can possibly make the following distinction: the halo structure can be developed by only one or a few loosely bound particle(s), while the skin phenomenon involves many particles. While halo particles are expected to occupy single-particle states with low angular momenta [19], nuclear skin can be formed by particles in any orbitals [20].

The physics of nuclear halos is among the most vigorously pursued subjects in nuclear structure. The heaviest neutron-rich lithium isotope $^{11}$Li is the first and probably the most spectacular case of a two-neutron halo (i.e., it can be viewed as two weakly bound neutrons orbiting around $^{9}$Li core) [21]. There are also other examples (see Fig. 2.1 and Sec. 2.1). The intensive studies of those exotic nuclei have been carried out both experimentally and theoretically, but so far a consistent and microscopic theory of nuclear halo has not been developed.

The reaction processes involving neutron-rich nuclei are also of interest because of their astrophysical importance [23-26]. The region of neutron-rich nuclei offers crucial tests for the Big Bang nucleosynthesis. Two types of models of primordial nu-

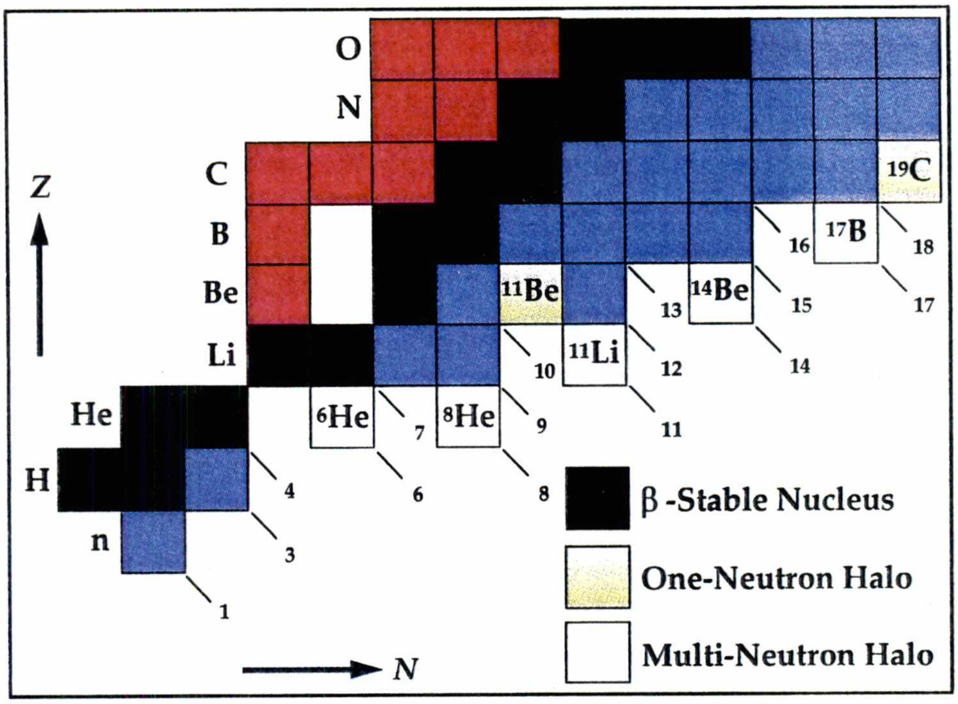


**Figure 2.1**: Experimentally observed one- and multi-neutron halos [22].

cleosynthesis are currently under investigation: the standard (homogeneous) model (SM) and the inhomogeneous model (IM) (corresponding references can be found in Refs. [26] and [27]). Both the SM and the IM predict rather similar abundances for the light nuclides, but different abundances for the heavier nuclides ($^{7}$Li, $^{9}$Be, $^{11}$B, and heavier) [28]. Therefore, studies of very neutron-rich medium-mass and heavy nuclei can possibly shed some light on the nature of the Big Bang nucleosynthesis.

## 2.1 Nuclear Halos

The phenomenon of halo can be found in various fields of physics. In astronomical scale, there appear the galactic halos which are 20 times as large as a typical diameter of a galaxy. The presence of these vast halos, composed primarily of cold dark matter particles, can account for the missing wavelengths of a quasar's light and the rotational character of galaxies [29, 30]. At the atomic and molecular levels, the halo phenomena are also known. The molecular halos such as $CH_3CN^-$ and $CS_2^-$ consist of a weakly bound electron and a neutral molecule. Their properties can be understood by assuming the presence of dipole and/or higher multipole fields in the otherwise neutral molecules [31]. Other examples of loosely bound systems can be found in $^4$He, namely the helium dimer (He-He) [32] and trimer (He-He-He) [33]. In particular, halo configurations (or 'Borromean' states, i.e., weakly bound states in a three-body system whose binary subsystems are unbound) in the loosely bound three-body systems, such as helium trimer, have been widely investigated in the framework of the hyperspherical coordinates [33-35].

The first indication of a nuclear halo was the discovery of the deuteron with its rms proton-neutron distance of about 4 fm. A spectacular example is the hypertriton $np\lambda$ (the lightest hypernucleus) [36], which has a $\lambda$-particle separation energy of $0.08\pm0.02$ MeV. The recent wide spread interest in weakly bound nuclei was stimulated by fragmentation studies of neutron-rich He, Li, and Be isotopes [21]. Here, two systems are of particular interest: $^{11}$Be and $^{11}$Li.

The nucleus $^{11}$Be may be viewed as a two-body system, consisting of a superdeformed $^{10}$Be core and one loosely bound neutron energetically located about 500 keV below the particle threshold. According to the shell-model picture, the expected ground state of $^{11}$Be is a $I^\pi=1/2^-$ state, whereas experimentally the $I^\pi=1/2^+$ state is found to be lower in energy. $^{11}$Be had been the only experimentally known one-neutron halo system until the recent discovery of $^{19}$C [37]. The narrow peak in the momentum distribution and a large cross section for the $^{19}C$ breakup were observed and explained in terms of a halo structure with one-neutron separation energy of $242 \pm 95$ keV.

A two-neutron halo nucleus $^{11}Li$ is one of the best examples (besides $^{6}He$ and $^{17}B$) of a Borromean system (see Fig. 2.2, and Ref. [38] for a review ). The reaction cross-section measurements on Li isotopes show the dramatic increase in rms radii when approaching $^{11}Li$. On the other hand, the measured charge cross-sections are consistent with the roughly constant proton distribution when going from $^{7}Li$ to $^{11}Li$ [39]. Furthermore, the measured magnetic and quadrupole moments are very similar in $^{9}Li$ and $^{11}Li$ [39]. These observations indicate the decoupling of the $^{9}Li$ core and two weakly bound neutrons in $^{11}Li$.

On the other hand, proton halos are less likely to exist due to the presence of the Coulomb barrier. It is to be noted, however, that $^{8}B$ is alleged to be a proton halo. It has a very small one-proton separation energy of 0.14 MeV [41] and a large quadrupole moment, and this can be qualitatively understood in terms of the proton halo-like structure [41]. According to the theoretical study of Ref. [42], a three-body Borromean nucleus $^{17}Ne$ is also claimed to be a proton halo. However, unlike neutron halos, the proton-halo phenomenon is not generally accepted. (See, e.g., Refs. [43] and [44] for discussion of the $^{8}B$ case. Similarly, neither microscopic calculations using the hyperspherical-coordinate method [45] nor a three-cluster generator-coordinate method of Ref. [46] support a proton halo scenario for $^{17}Ne$.)

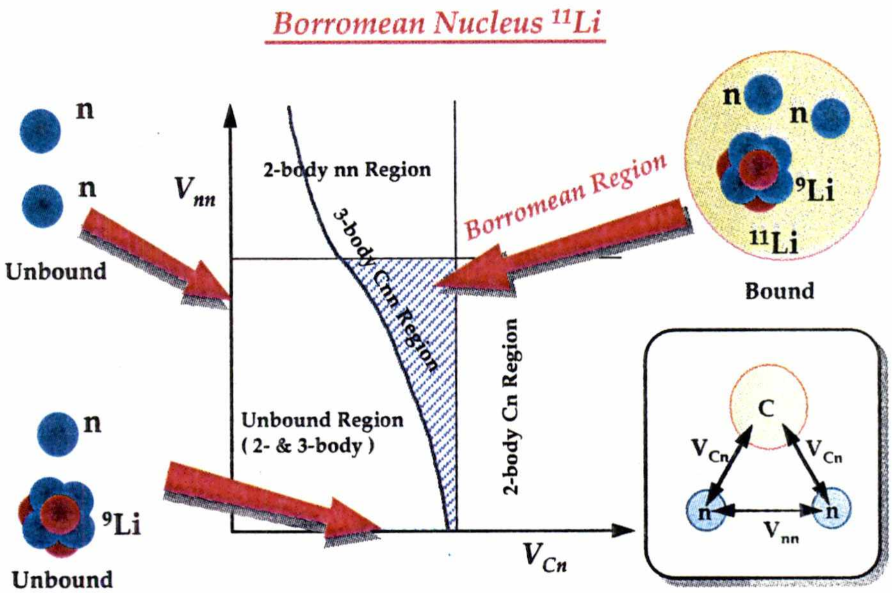


**Figure 2.2**: Schematic plot [40] for a three-body system (C-n-n) in terms of the strengths of two-body potentials ($V_{nn}$, $V_{Cn}$) and three-body potential ($V_{Cnn}$). Upper right: Nucleus $^{11}$Li composed of $^9$Li core and two weakly bound neutrons is located in the 'Borromean' region (shaded area). Upper left: Two neutrons do not form a bound state. Lower left: Binary subsystem composed of $^9$Li and one neutron does not have a bound state.

Many unusual features of neutron halos have been discovered experimentally [40]. The main signature of a neutron halo is the large spatial extension of matter density. The rms radii in $^{11}$Be and $^{11}$Li obtained from cross-section measurements are 2.71 $\pm$ 0.05 fm and 3.10 $\pm$ 0.17 fm, respectively. These should be compared with the corresponding matter radii in $^{10}$Be (2.28$\pm$ 0.02 fm) and $^9$Li (2.32$\pm$ 0.02 fm).

The narrow momentum distribution obtained through projectile fragmentation processes [47, 48] can also be interpreted in terms of a halo structure. It is known [49] that the momentum distribution of the outgoing fragment reflects the momentum distribution of the nucleon removed from the surface of the projectile. Due to the uncertainty principle, the narrow width of the momentum distribution corresponds to the large spatial dimensions of a system. The transverse-momentum distribution of $^{9}$Li ($^{8}$Li) obtained through the reaction $^{11}$Li+C shows both narrow- and wide-width structures [47]. The wide component of the momentum distribution is characteristic of a well-bound nucleus, whereas the narrow-width component can be interpreted as an evidence for a large-size halo structure.

The process of $\beta$ decay is an useful tool to examine properties of halo nuclei. Here, the well-known examples are $\beta$ transitions between the ground states of $^{6}$He ($\alpha$+di-neutron) and $^{6}$Li ($\alpha$+deuteron), and between the ground state of $^{11}$Li and the first excited state (320 keV) of $^{11}$Be. The emission of a $\beta$-delayed deuteron from $^{6}$He was first observed by Riisager *et al.* [50]. There are two main channels in this process. The first channel is the direct $\beta$ decay of $^{6}$He to $^{6}$Li followed by a break-up into alpha particle and deuteron. The second channel is the direct $\beta$ decay of $^{6}$He to the continuum. These two decay channels were not sufficient to reproduce the experimental deuteron spectrum. A better agreement was obtained by involving the third process: the break-up of $^{6}$He into an alpha particle and the di-neutron and the subsequent $\beta$ decay of the di-neutron [51] (see Fig. 2.3). The presence of the latter decay channel confirms the three-body nature of $^{6}$He. The $\beta$ transition from the ground state of $^{11}$Li to the first excited state of $^{11}$Be was studied in Ref. [52] in terms of a shell-model picture. The study indicates that a large log*ft* value of the Gamow-Teller transition can be obtained by taking into account the effect of a halo.

It has also been suggested in several theoretical studies [53-57] that the so-called *soft* dipole mode (or *pygmy* mode), i.e., the low-frequency oscillation of the well-bound core against the halo neutrons, may exist in weakly bound systems (see

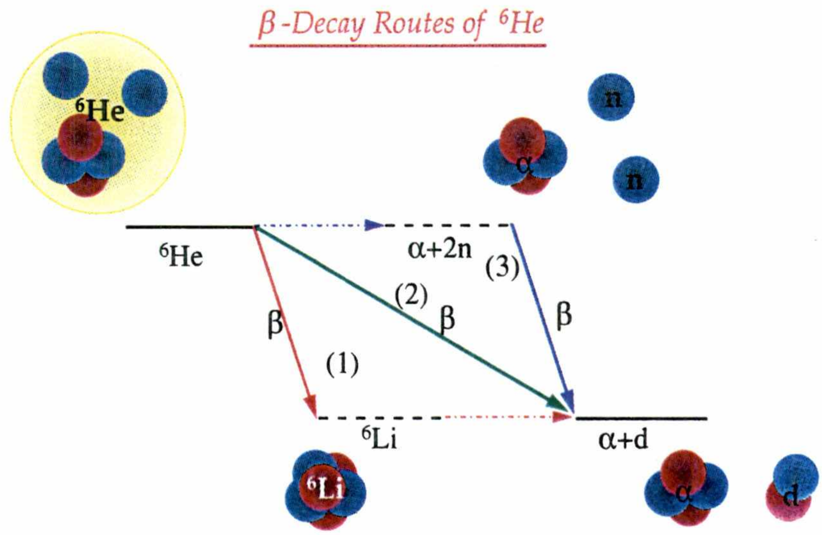


**Figure 2.3**: Schematic diagram [51] for the $\beta$-decay channels of $^6$He. (1) $\beta$ decay of $^6$He to $^6$Li and the subsequent break-up into $\alpha$+deuteron. (2) Direct $\beta$ decay of $^6$He into continuum states of $\alpha$+deuteron. (3) Break-up of $^6$He into $\alpha$+di-neutron and the subsequent $\beta$ decay of di-neutron. The dashed lines indicate the virtual states during $\beta$-decay process.

Fig. 2.4). According to the simple model of Ref. [55], the lowest excitation energy of the soft dipole mode is

$$\hbar\omega = \sqrt{\frac{Z(N - N_c)}{N(Z + N_c)}}\hbar\omega_{\mathrm{GDR}}, \tag{2.1}$$

where $\omega_{\mathrm{GDR}}$ is the frequency of the giant dipole resonance (GDR), and $Z$, $N$, and $N_c$ represent the total number of protons, neutrons, and core neutrons respectively. This indicates that the energy of the soft dipole mode should be reduced with respect to that of the normal GDR. According to the GDR model employed in Ref. [53], the energy of the soft dipole mode is expected to be around 0.9 MeV. This should be compared to the energy of the normal GDR which is around 22 MeV. In spite of many experimental efforts (e.g., the very recent Coulomb-dissociation studies [15, 43, 58]

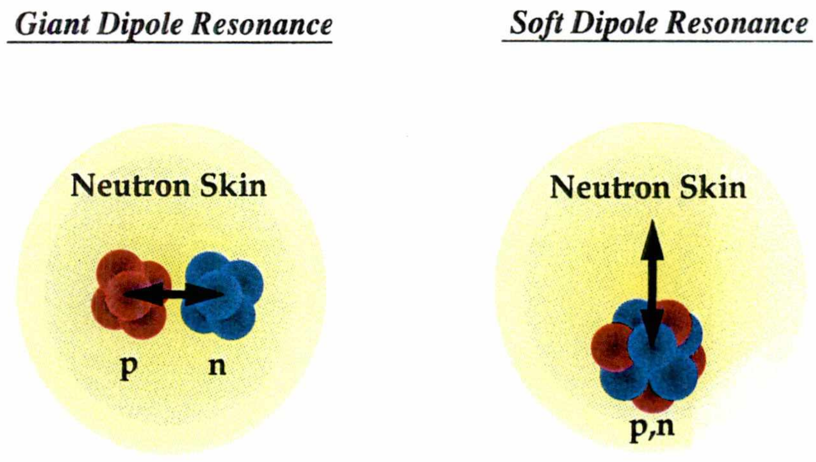


**Figure 2.4**: Left: Dipole oscillation of protons against neutrons in the core (usual isovector giant dipole resonance). Right: Dipole oscillation of the neutron skin (halo) against the core (soft dipole mode).

of $^{11}$Be and $^{11}$Li performed at RIKEN and MSU), no significant fingerprint of the soft dipole mode has been found. (In this context, it is worth mentioning that the recent study of Ref. [59] argues that the low-lying dipole strength in the continuum does not exhibit a *resonant* character.)

The above phenomena, which exist or are expected to exist in halo nuclei, can be attributed to weak binding. In Chapter 3, however, it is argued that shape deformation can also play a significant role in describing some of these effects. The main objective of this work is to explore the concept of 'shape' in loosely bound systems by simultaneously taking into account both deformation and weak binding.

## 2.2 General Properties of Neutron Drip-line Nuclei

Nuclei close to the particle drip lines exhibit or are expected to exhibit a rich variety of properties which do not occur, or are much less pronounced, in nuclei close to the beta stability valley. One of the characteristic features of nuclei near the neutron drip line is the presence of a neutron skin. According to the mean-field calculations of Ref. [60], there exists a clear correlation between the neutron-skin thickness and the energy difference between the neutron and the proton Fermi levels (see Fig. 2 of Ref. [60]). Those calculations predict the strongest effect in the neutron-rich $\beta$-unstable nuclei $^{6}$He, $^{8}$He, and $^{24}$O . The recent studies of $^{A}$Na isotopes ($A$=20-23, 25-32) [61] demonstrate the roughly linear correlation between the thickness of the neutron skin and the difference between the proton and neutron separation energies.

The shell structure of the $\beta$-unstable magic nuclei is also of interest. Experimentally, deformed states in magic nuclei are known in many cases (see Ref. [62]). In the *sd* region, the neutron-rich nuclei with $N\sim20$ are spectacular examples of coexistence between spherical and deformed configurations. A classic example of a magic nucleus with a deformed ground state is $^{32}_{12}$Mg$_{20}$, which has a very low-lying $2^{+}$ state at 886 keV [63] and an anomalously high value of two-neutron separation energy $S_{2n}$. Calculations based on the deformed mean-field theory predict deformed ground states around $^{32}$Mg and explain them in terms of neutron excitations to the $1f_{7/2}$ shell [64, 65]. A similar conclusion has been drawn in the shell-model calculations in the $(sd)(fp)$ model space [66, 67] and in the schematic analysis of Ref. [68].

In Chapter 5, the sulfur isotopes, especially the neutron-rich ones with $N{\sim}28$ will be discussed. This particular choice was motivated by recent experimental and astrophysical interest in this mass region [23-25]. From the perspective of the spherical shell model, the underlying proton wave functions are described in terms of the *sd* shell-model space, while the main components of the neutron wave functions come from the *fp* shell-model space. Such a schematic classification, however, easily breaks down due to the strong core polarization effect (i.e., the appearance of static shape deformations associated with the core-breaking excitations).

Experimentally, little is known about the neutron-rich nuclei around $^{44}$S. Recently, $\beta$-decay properties of $^{44}$S and $^{45-47}$Cl have been studied in GANIL [23, 69]. The half-life of $^{44}$S was found to be $T_{1/2}$=123±10 ms. (Observation of $^{42}$Si, $^{45,46}$P, $^{48}$S, and $^{51}$Cl has been reported in Ref. [70].) Another very recent experiment on the neutron-rich nuclei $^{38,40,42}$S and $^{44,46}$Ar, performed at MSU [71], indicates moderate deformations around $N$=28.

Theoretical information on the light $N{\approx}28$ nuclei is very scarce. The results of recent large-scale mass calculations using the finite-range droplet model (FRDM) [72] or the extended Thomas-Fermi with Strutinsky-integral model (ETFSI) [73] suggest the presence of deformation in some $N$=28 isotones (see, e.g., Table IV of Ref. [23]). Based on these calculations and on the theoretical analysis of $\beta$-decay properties of $^{44}$S, it has been suggested in Ref. [23] that the influence of the spherical shell $N$=28 is weakened below $^{48}$Ca.

In the regions near particle drip lines, the closeness of the unbound scattering states and extreme spatial extensions of weakly bound systems make neutron- or proton-rich nuclei very difficult to describe in terms of currently used models with their parameters determined so as to reproduce the properties of stable nuclei [74-78]. According to one theoretical finding [79], the single-particle potential of neutron drip-line nuclei resembles that of a harmonic oscillator with a spin-orbit term. Such changes in the shell structure due to weak binding and/or deformation can dramatically affect the location of the neutron drip line.

Experimental studies of nuclei close to the neutron drip line also raise many questions regarding the role of pairing interaction. In the vicinity of particle drip lines, the presence of pairing correlation implies the scattering of paired nucleons from bound states to the continuum. The models based on the Bardeen-Cooper-Schrieffer (BCS) type treatment give rise to an unphysical evaporation of particles into the continuum and hence the incorrect asymptotic form of the quasiparticle wave function [80, 81]. It was pointed out [77-82] that the Hartree-Fock-Bogoliubov (HFB) method with a realistic pairing interaction can overcome such difficulties. In this study, we concentrate on the particle-hole channel. Pairing correlations will either be ignored or assumed to be very weak.

So far, neutron drip lines have been determined for all light nuclei with $Z < 10$ [83, 84]. The advancements of the RNB experimentation can clarify basic features of heavier drip-line nuclei and possibly help to discriminate between various theoretical models. In this context, the present work offers model predictions for the position of the neutron drip line in the Si-Ca region.

# Chapter 3

# Deformed Halo Nuclei

The importance of non-spherical intrinsic shapes in halo nuclei has already been stressed in several papers, especially in the context of a one-neutron halo $^{11}$Be and an alleged one-proton halo $^{8}$B. The ground state of $^{11}$Be is a $1/2^{+}$ state. The low neutron separation energy, $S_n$=504 keV, allows for only one bound excited level ($1/2^{-}$ at 320 keV). The halo character of $^{11}$Be has been confirmed by studies of reaction cross sections [85] and the importance of deformation can be inferred from the large quadrupole moment of its core $^{10}$Be, $|Q|$=229 mb [86]. The halo character of $^{8}$B has been suggested in Ref. [41] where the large measured quadrupole moment of its $I^{\pi}=2^{+}$ ground state, $|Q|$=68 mb, has been attributed to the weak binding of the fifth proton in the $1p_{3/2}$ state. (The existence of a proton halo in $^{8}$B is still heavily debated [39, 87]. For instance, Nakada and Otsuka [43], in a shell-model calculation, demonstrated that the large value of $|Q|$ in $^{8}$B could be understood without introducing the proton halo.)

Figure 3.1 shows the interaction radii for a series of Be isotopes deduced from measured interaction cross sections [88]. The relatively large radius for $^{11}$Be has been interpreted as a sign of halo structure of this nucleus. It is, however, quite interesting to note that calculated deformations (as obtained in Nilsson-Strutinsky calculations) of the Be isotopes are found to vary in such a way that the corresponding nuclear radii reproduce the data quite well. In these calculations, no effects from the halo structure of $^{11}$Be have been considered since they are based on the (infinite) modified oscillator potential. Although these calculations are somewhat unrealistic, the result displayed in Fig. 3.1 clearly stresses the importance of simultaneously considering both deformation and halo effects in nuclei such as in $^{11}$Be.

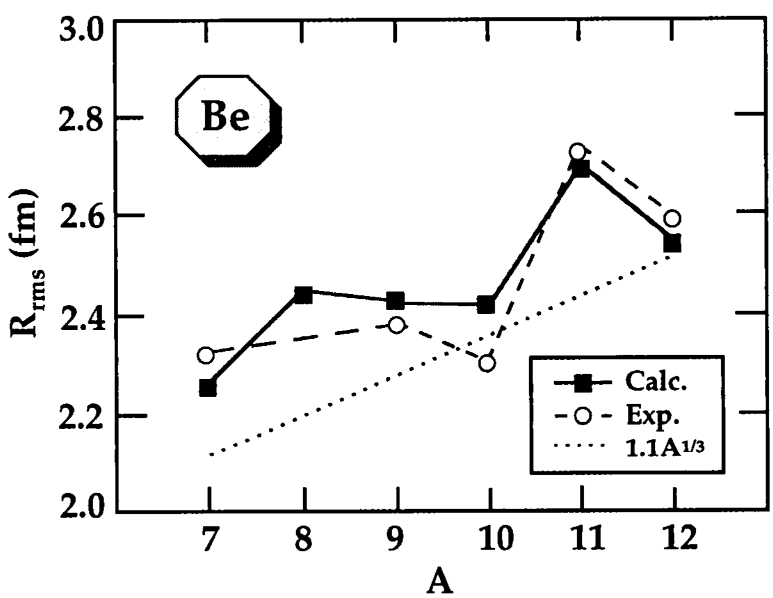


**Figure 3.1**: Nuclear rms radii calculated in the modified harmonic oscillator model (filled squares) for a series of Be isotopes. They are compared to measured [88] interaction radii (open circles). The calculated deviation from the smooth $1.1A^{1/3}$ behavior (dot-dash line) is due to deformation.

In this chapter, the question of deformed two-body halos is addressed by considering the single-particle motion in the axial reflection-symmetric central potential. The properties of the deformed single-particle states, especially in the subthreshold region, are analyzed by making the multipole decomposition in the spherical partial waves with well-defined orbital angular momentum.

## 3.1 Overview of Theoretical Approaches

The role of shape effects in lowering the excitation energy of the $1/2^+$ intruder level in $^{11}$Be has been recognized long ago. For instance Bouten *et al.* [89] pointed out that the position of the abnormal-parity intruder orbitals in odd $p$-shell nuclei can be dramatically lowered by deformation, and they performed the projected HF calculations for the parity doublet in $^{11}$Be. In another paper, based on the cranked Nilsson model, Ragnarsson *et al.* [90] demonstrated that the parity doublet could be naturally understood in terms of the [220]1/2 ($1d_{5/2} \otimes 2s_{1/2}$) Nilsson [91] orbital. In particular, they calculated very large prolate deformation for the positive-parity level, and spherical shape for the negative-parity state. Muta and Otsuka [44, 92] studied the structure of $^{11}$Be and $^{8}$B with a deformed Woods-Saxon potential considering quadrupole deformation as a free parameter adjusted to the data. Tanihata *et al.* [93] concluded, based on a spherical one-body potential, that the positions of experimental drip lines are consistent with the spherical picture; they emphasized the effect of increased binding of the low-$\ell$ shell model states near the threshold that can give rise to the level inversion. However, none of these above papers has considered simultaneously both effects, i.e., the loose binding and self-consistency.

Another, more microscopic, approach is the work by Kanada-En'yo *et al.* [94] based on antisymmetrized molecular dynamics with improved asymptotics. They obtained very large quadrupole deformation for the $1/2^+$ state in $^{11}$Be, and a less deformed $1/2^-$ state. A similar conclusion has been drawn in the recent self-consistent Skyrme-HF calculations [95].

Very recently, the notion of deformation in $^{11}$Be has been also pursued by several authors [96-100] within several variants of the weak coupling scheme. In these models, the odd neutron moving in a Woods-Saxon potential is weakly coupled to the deformed core of $^{10}$Be, and interacts with the core through the quadrupole field. The deformation of $^{11}$Be is not treated self-consistently; either the strength of the quadrupole coupling is adjusted to the data to reproduce the quadrupole moment of $^{10}$Be, or the deformation is adjusted to reproduce the energies of the $I$=1/2 doublet. The advantage of the weak coupling approach is that the total wave functions are eigenstates of the total angular momentum and they have correct asymptotic behavior. In this context, a nice molecular analogy, in which the adiabatic coupling of the valence particle to the deformed core is applied, is the weak binding of an electron to a rotationally excited dipolar system [101], or to a neutral symmetric molecule with a non-zero quadrupole moment [31].

## 3.2 Generic Features of Deformed Neutron Halos

This section contains some general arguments regarding the concept of shape deformation in two-body halo systems. The material contained in this section is the extension of the analysis of Ref. [19] carried out for the spherical case. (For the corresponding discussion of three-body halo asymptotics, see Ref. [102].) The following analysis also provides a qualitative understanding of the numerical results presented in the following Chapters 4 and 5.

### 3.2.1 Behavior of Radial Matrix Elements in The Limit of Weak Binding

Let us assume that the weakly bound neutron moves in a deformed average potential $U(\vec{r})$ (usually well approximated by a sum of the central potential and the spin-orbit potential). The neutron wave function can be obtained by solving the deformed single-particle Schrödinger equation

$$\left[\nabla^2 - \frac{2\mu}{\hbar^2}U(\vec{r}) - \kappa_\nu^2\right]\psi_\nu(\vec{r}) = 0, \tag{3.1}$$

where $\kappa_\nu = \sqrt{-2\mu\epsilon_\nu/\hbar^2}$ and $\epsilon_\nu$ is the corresponding single-particle energy. In the following, we assume the axial reflection-symmetric central potential. (The generalization to the triaxial and/or reflection-asymmetric case is straightforward.) Since the asymptotic properties of radial matrix elements depend very weakly on intrinsic spin, the spin-orbit term is neglected.

Owing to the axial-reflection symmetry, the single-particle states can be labeled by means of excitation quantum number $\nu$, projected angular momentum $\Lambda$, and parity $\pi$. Since the Hamiltonian considered is invariant with respect to the time-reversal symmetry, we shall only consider non-negative values of $\Lambda$.

The deformed wave function can be decomposed into spherical partial waves with the well-defined orbital angular momentum $\ell$:

$$\psi_{\nu\Lambda\pi}(\vec{r}) = \sum_{\ell}{}' R_{\nu\ell\Lambda}(r) Y_{\ell\Lambda}(\theta,\phi), \tag{3.2}$$

where $R_{\nu\ell\Lambda}$ and $Y_{\ell\Lambda}$ are spherical radial and angular functions respectively, and prime sign on summation symbol indicates $\ell = 0, 2, 4, ...$ for positive parity and $\ell = 1, 3, 5, ...$ for negative parity. At large distances ($r > R_0$, where $R_0$ defines the arbitrary but fixed distance at which the nuclear interaction becomes unimportant), $U(\vec{r})$ vanishes and the radial functions $R_{\nu\ell}(r)$ satisfy the free-particle radial Schrödinger equation

$$\left[\frac{d^2}{dr^2} + \frac{2}{r}\frac{d}{dr} - \kappa_\nu^2 - \frac{\ell(\ell+1)}{r^2}\right] R_{\nu\ell}(r) = 0. \tag{3.3}$$

(Of course, $R_{\nu\ell\Lambda}(r) = R_{\nu\ell}(r)$ for $r \geq R_0$.) The solution of Eq. (3.3) is $R_{\nu\ell}(r) = B_{\nu\ell} h_\ell^{(1)}(i\kappa_\nu r)$ where $h_\ell^{(1)}$ is the spherical Hankel function and $B_{\nu\ell}$ is a constant, given by

$$B_{\nu\ell} = R_{\nu\ell}(R_0)/h_\ell^{(1)}(i\kappa_\nu R_0). \tag{3.4}$$

The spatial properties of the system can be characterized by the $n$th radial moments $\langle\psi_{\nu\Lambda\pi}|r^n|\psi_{\nu\Lambda\pi}\rangle$ and multipole moments $\langle\psi_{\nu\Lambda\pi}|r^n Y_{n0}|\psi_{\nu\Lambda\pi}\rangle$. Both quantities require the evaluation of radial matrix elements

$$\langle R_{\nu\ell\Lambda}|r^n|R_{\nu\ell'\Lambda}\rangle = \int_0^\infty r^{n+2} R_{\nu\ell\Lambda}^*(r) R_{\nu\ell'\Lambda}(r) dr \equiv I_{\nu n\ell\ell'\Lambda} + O_{\nu n\ell\ell'}, \tag{3.5}$$

where $I_{\nu n\ell\ell'\Lambda}$ and $O_{\nu n\ell\ell'}$ represent the internal ($r \leq R_0$) and external ($r > R_0$) contributions, respectively. The inner integral $I_{\nu n\ell\ell'\Lambda}$ is, by definition, finite. The outer integral can be written as

$$\begin{aligned}
O_{\nu n\ell\ell'} &= \int_{R_0}^{\infty} r^{n+2} R^*_{\nu\ell}(r) R_{\nu\ell'}(r) dr && (3.6)\\
&= B^*_{\nu\ell} B_{\nu\ell'} \int_{R_0}^{\infty} r^{n+2} h^{(1)*}_{\ell}(i\kappa r) h^{(1)}_{\ell'}(i\kappa_\nu r) dr && (3.7)\\
&= B^*_{\nu\ell} B_{\nu\ell'} \kappa_\nu^{-(n+3)} \int_{R_0\kappa_\nu}^{\infty} x^{n+2} h^{(1)*}_{\ell}(ix) h^{(1)}_{\ell'}(ix) dx && (3.8)\\
&= B^*_{\nu\ell} B_{\nu\ell'} \kappa_\nu^{-(n+3)} \int_{R_0\kappa_\nu}^{a\kappa_\nu+\Delta} x^{n+2} h^{(1)*}_{\ell}(ix) h^{(1)}_{\ell'}(ix) dx \\
&\quad + B^*_{\nu\ell} B_{\nu\ell'} \kappa_\nu^{-(n+3)} \int_{R_0\kappa_\nu+\Delta}^{\infty} x^{n+2} h^{(1)*}_{\ell}(ix) h^{(1)}_{\ell'}(ix) dx, && (3.9)
\end{aligned}$$

where $\Delta$ is a small number. Since the analytic expansion of the spherical Hankel function is given by

$$h^{(1)}_{\ell}(z) = i^{-\ell-1} z^{-1} e^{iz} \sum_{k=0}^{\ell} \left(\ell + \frac{1}{2}, k\right) (-2iz)^{-k} \tag{3.10}$$

where

$$\left(\ell + \frac{1}{2}, k\right) = \frac{(\ell+k)!}{k!(\ell-k)!}, \tag{3.11}$$

the asymptotic form of spherical Hankel function can be written as

$$h^{(1)}_{\ell}(ix) \xrightarrow{x\to 0} -(2i)^{-\ell} \left(\ell + \frac{1}{2}, \ell\right) x^{-\ell-1}. \tag{3.12}$$

Consequently,

$$B_{\nu\ell} = \frac{R_{\nu\ell}(R_0)}{h^{(1)}_{\ell}(i\kappa_\nu R_0)} \to \frac{-(2i)^{\ell}}{\left(\ell + \frac{1}{2}, \ell\right)} (\kappa_\nu R_0)^{\ell+1}. \tag{3.13}$$

Following the arguments of Ref. [19], one can demonstrate that for small values of $\kappa_\nu$ the integral $O_{\nu n\ell\ell'}$ behaves asymptotically as

$$O_{\nu n\ell\ell'} \cong \kappa_\nu^{\ell+\ell'-n-1} R_0^{\ell+\ell'+2} \left[ \int_{R_0\kappa_\nu}^{R_0\kappa_\nu+\Delta} x^{n-\ell-\ell'} dx + \text{const.} \right]. \tag{3.14}$$

Therefore, the asymptotic behavior of $O_{\nu n\ell\ell'}$ in the limit of small $\epsilon_\nu$ strongly depends on quantum numbers $n$, $\ell$, and $\ell'$.

Let us consider three cases:

(i) $n-\ell-\ell' > -1$

Here, the integral $O_{\nu n\ell\ell'}$ can be approximated as

$$O_{\nu n\ell\ell'} \cong \kappa_\nu R_0^{\ell+\ell'+2}\left[\frac{(R_0\kappa_\nu+\Delta)^{n-\ell-\ell'+1}-(R_0\kappa)^{n-\ell-\ell'+1}}{n-\ell-\ell'+1}+\text{const.}\right]. \qquad (3.15)$$

Since $\Delta$ is finite, a first term in [ ] remains finite. Hence, $O_{\nu n\ell\ell'}$ diverges as $(-\epsilon_\nu)^{(\ell+\ell'-n-1)/2}$.

(ii) $n-\ell-\ell' = -1$

Here, $O_{\nu n\ell\ell'}$ behaves as

$$O_{\nu n\ell\ell'} \cong a^{n+3}\left[\ln\left(\frac{a\kappa_\nu+\Delta}{a\kappa_\nu}\right)+\text{const.}\right] \propto -\ln(\kappa_\nu). \qquad (3.16)$$

This indicates that $O_{\nu n\ell\ell'}$ diverges as $\ln(-\epsilon_\nu)$.

(iii) $n-\ell-\ell' < -1$

Here, the asymptotic expression for $O_{\nu n\ell\ell'}$ is exactly the same as in Eq.(3.15); however, a first term in [ ] of Eq.(3.15) diverges as $\kappa_\nu^{n-\ell-\ell'+1}$. As a result, $O_{\nu n\ell\ell'}$ remains finite.

### 3.2.2 The Normalization Integral

The norm of the deformed state (3.2), $\mathcal{N}_{\nu\Lambda\pi}$, can be expressed through the zeroth radial moment

$$(\mathcal{N}_{\nu\Lambda\pi})^2 = \langle\psi_{\nu\Lambda\pi}|\psi_{\nu\Lambda\pi}\rangle = \sum_\ell{}'\langle R_{\nu\ell\Lambda}|r^0|R_{\nu\ell\Lambda}\rangle = \sum_\ell{}'\left(I_{\nu 0\ell\ell\Lambda}+O_{\nu 0\ell\ell}\right). \qquad (3.17)$$

According to conditions (i)-(iii), the norm is divergent only if the deformed state contains an admixture of the $s$-wave. This is possible only for orbitals with $\pi$=+ and $\Lambda$=0. In this case, the norm behaves asymptotically as $\sqrt{O_{\nu 000}} \propto (-\epsilon_\nu)^{-1/4}$, and the probability to find the particle in the outer region ($r > R_0$),

$$P_{\nu\Lambda\pi}^{(\text{ext})} = \frac{\sum_\ell{}' O_{\nu 0\ell\ell}}{\sum_\ell{}'(I_{\nu 0\ell\ell\Lambda} + O_{\nu 0\ell\ell})}, \tag{3.18}$$

approaches one for zero binding.

### 3.2.3 The $n$th Radial Moment

The $n$th radial moment of a deformed orbital, $\langle\nu\Lambda\pi|r^n|\nu\Lambda\pi\rangle$, can be expanded in terms of $I_{\nu n\ell\ell\Lambda}$ and $O_{\nu n\ell\ell}$:

$$\langle\nu\Lambda\pi\,|r^n|\,\nu\Lambda\pi\rangle = (\mathcal{N}_{\nu\Lambda\pi})^{-2}\sum_\ell{}'\langle R_{\nu\ell\Lambda}|r^n|R_{\nu\ell\Lambda}\rangle = (\mathcal{N}_{\nu\Lambda\pi})^{-2}\sum_\ell{}'(I_{\nu n\ell\ell\Lambda} + O_{\nu n\ell\ell}). \tag{3.19}$$

Following the arguments of Sec. 3.2.2, the asymptotic behavior of the $n$th radial moment depends on $\Lambda$ and $\pi$ quantum numbers of the deformed orbital:

$$\pi = +,\ \Lambda = 0 \ :\ \langle\nu 0+|r^n|\nu 0+\rangle \text{ diverges as } (-\epsilon_\nu)^{-n/2}, \tag{3.20}$$

$$\pi = -,\ \Lambda = 0 \text{ or } 1 \ :\ \langle\nu\Lambda-|r^n|\nu\Lambda-\rangle \text{ diverges as } (-\epsilon_\nu)^{(1-n)/2}, \tag{3.21}$$

$$\text{otherwise} \ :\ \langle\nu\Lambda\pi|r^n|\nu\Lambda\pi\rangle \text{ remains finite.} \tag{3.22}$$

For the special case of $n = 2$, the root-mean-square radius diverges only if the deformed orbital in question contains $s$ or $p$ partial waves. This leaves only three classes of states, for which the spatial extension can be arbitrary large:

$$\pi = +,\ \Lambda = 0 \ :\ \langle\nu 0+|r^2|\nu 0+\rangle \text{ diverges as } (-\epsilon_\nu)^{-1}, \tag{3.23}$$

$$\pi = -, \ \Lambda = 0 \text{ or } 1 \quad : \quad \langle \nu\Lambda - |r^2|\nu\Lambda-\rangle \text{ diverges as } (-\epsilon_\nu)^{-1/2}. \tag{3.24}$$

In the following, these states are refered to as 'halo states' or 'halos'. Of course, this does not mean that other Nilsson orbitals cannot form very extended structures when their binding becomes very small. However, it is only for the states (3.23) and (3.24) that the rms radius becomes asymptotically infinite.

### 3.2.4 Multipole Moments

The average multipole moment of a deformed orbital, $\langle \nu\Lambda\pi|r^n Y_{n0}|\nu\Lambda\pi\rangle$, is given by

$$\langle \nu\Lambda\pi|r^n Y_{n0}|\nu\Lambda\pi\rangle \equiv (\mathcal{N}_{\nu\Lambda\pi})^{-2} \langle \psi_{\nu\Lambda\pi}|r^n Y_{n0}|\psi_{\nu\Lambda\pi}\rangle \tag{3.25}$$

$$= (\mathcal{N}_{\nu\Lambda\pi})^{-2} \sum_{\ell,\ell'}{}' \langle R_{\nu\ell\Lambda}|r^n|R_{\nu\ell'\Lambda}\rangle \langle Y_{\ell\Lambda}|Y_{n0}|Y_{\ell'\Lambda}\rangle. \tag{3.26}$$

The angular matrix elements $\langle Y_{\ell\Lambda}|Y_{n0}|Y_{\ell'\Lambda}\rangle$ can be expressed in terms of three-$j$ symbols by applying the Wigner-Eckart theorem:

$$\langle Y_{\ell\Lambda}|Y_{n0}|Y_{\ell'\Lambda}\rangle = (-1)^\Lambda \begin{pmatrix} \ell & n & \ell' \\ -\Lambda & 0 & \Lambda \end{pmatrix} \begin{pmatrix} \ell & n & \ell' \\ 0 & 0 & 0 \end{pmatrix} \sqrt{\frac{(2\ell+1)(2n+1)(2\ell'+1)}{4\pi}}, \tag{3.27}$$

where $\ell + \ell' + n$ is even. The above expression is non-zero, only if $\ell$, $\ell'$, and $n$ are less than or equal to $(\ell + \ell' + n)/2$. By taking into account these selection rules and the conditions (i)-(iii) of Sec. 3.2.1, one obtains:

$$\pi = +, \ \Lambda = 0 \quad : \quad \langle \nu 0 + |r^n Y_{n0}|\nu 0+\rangle \text{ remains finite for even-}n$$

$$\text{and vanishes for odd-}n, \tag{3.28}$$

$$\pi = -, \ \Lambda = 0 \text{ or } 1 \quad : \quad \langle \nu\Lambda - |r^n Y_{n0}|\nu\Lambda-\rangle \text{ diverges as } (-\epsilon_\nu)^{-1/2} \text{ for even-}n$$

$$\text{and diverges as } \ln(-\epsilon_\nu) \text{ for odd-}n. \tag{3.29}$$

In the particular case of a quadrupole moment, $\langle\nu\Lambda\pi|r^2Y_{20}|\nu\Lambda\pi\rangle$ , Eq.(3.27) reduces to

$$\langle Y_{\ell\Lambda}|Y_{20}|Y_{\ell'\Lambda}\rangle = \sqrt{\frac{5}{4\pi}}\sqrt{\frac{2\ell'+1}{2\ell+1}}\langle\ell'\Lambda 20|\ell\Lambda\rangle\langle\ell' 020|\ell 0\rangle. \tag{3.30}$$

Since the quadrupole moment of an $s$ state vanishes, the only diverging matrix element in the limit of small binding energies comes from an $s \leftrightarrow d$ coupling for positive-parity halos ($\pi = +$, $\Lambda = 0$). According to Eqs. (3.28) and (3.29), one obtains:

$$\pi = +,\ \Lambda = 0 \ :\ \langle\nu 0+|r^2Y_{20}|\nu 0+\rangle \text{ remains finite,} \tag{3.31}$$

$$\pi = -,\ \Lambda = 0 \text{ or } 1 \ :\ \langle\nu\Lambda -|r^2Y_{20}|\nu\Lambda -\rangle \text{ diverges as } (-\epsilon_\nu)^{-1/2}. \tag{3.32}$$

Sometimes it is useful to consider an external ($\xi > \xi_0$) contribution to the quadrupole moment, $\Theta^{(\text{ext})}_{\nu\Lambda\pi}$, defined by

$$\Theta^{(\text{ext})}_{\nu\Lambda\pi} \equiv \frac{\sum_{\ell,\ell'}{}' O_{\nu 2\ell\ell'}\langle Y_{\ell\Lambda}|Y_{20}|Y_{\ell'\Lambda}\rangle}{\sum_{\ell,\ell'}{}'(I_{\nu 2\ell\ell'\Lambda} + O_{\nu 2\ell\ell'})\langle Y_{\ell\Lambda}|Y_{20}|Y_{\ell'\Lambda}\rangle}. \tag{3.33}$$

According to the above results, the values of $\Theta^{(\text{ext})}_{\nu\Lambda\pi}$ for negative-parity halo states ($\pi = -$, $\Lambda = 0$ or 1) approach one at vanishing values of $\epsilon_\nu$.

### 3.2.5 Multipole Deformations

It is instructive to consider the multipole deformation $\beta_n$ extracted from the ratio

$$\beta_n(\nu\Lambda\pi) = \frac{4\pi}{n+3}\frac{\langle\nu\Lambda\pi|r^nY_{n0}|\nu\Lambda\pi\rangle}{\langle\nu\Lambda\pi|r^n|\nu\Lambda\pi\rangle}. \tag{3.34}$$

From previous discussions, one can conclude that the multipole deformation of a positive-parity halo state vanishes for all multipolarities, i.e.,

$$\beta_n(\pi = +, \Lambda = 0) \xrightarrow{\epsilon_\nu \to 0} 0. \tag{3.35}$$

For negative-parity halos, all multipole deformations with $n \neq 2$ also vanish at the limit of small $\epsilon_\nu$:

$$\beta_n(\pi = -, \Lambda) \xrightarrow{\epsilon_\nu \to 0} 0 \qquad n \neq 2. \tag{3.36}$$

However, quadrupole deformation ($n = 2$) approaches the finite limit:

$$\beta_2(\pi = -, \Lambda) \xrightarrow{\epsilon_\nu \to 0} \frac{4\pi}{5}\langle Y_{1\Lambda}|Y_{20}|Y_{1\Lambda}\rangle = \begin{cases} +0.63 & \text{if } \Lambda = 0 \\ -0.31 & \text{if } \Lambda = 1. \end{cases} \tag{3.37}$$

Let us now consider deformation properties of a halo system consisting of the core nucleons and loosely bound valence nucleon. The total multipole deformation of the system, denoted by $\beta_n$(total), can be split into two contributions, namely from the core (c) nucleons and from the valence (v) particles:

$$\begin{aligned} \beta_n(\text{total}) &= \frac{4\pi}{n+3}\frac{\langle r^n Y_{n0}\rangle_{\text{c}} + \langle r^n Y_{n0}\rangle_{\text{v}}}{\langle r^n\rangle_{\text{c}} + \langle r^n\rangle_{\text{v}}} && (3.38) \\ &= \frac{4\pi}{n+3}\frac{\langle r^n Y_{n0}\rangle_{\text{c}}/\langle r^n\rangle_{\text{v}} + \langle r^n Y_{n0}\rangle_{\text{v}}/\langle r^n\rangle_{\text{v}}}{1 + \langle r^n\rangle_{\text{c}}/\langle r^n\rangle_{\text{v}}}. && (3.39) \end{aligned}$$

Since in the limit of weak binding energies $\langle r^n\rangle_{\text{v}} \gg \langle r^n\rangle_{\text{c}}$, Eq.(3.39) can be approximated by the multipole deformation of the valence state:

$$\beta_n(\text{total}) \xrightarrow{\epsilon_\nu \to 0} \frac{4\pi}{n+3}\langle r^n Y_{n0}\rangle_{\text{v}}/\langle r^n\rangle_{\text{v}}. \tag{3.40}$$

That is, independently of the shape of the core, the deformation of the halo is solely determined by the spatial structure of the valence-state wave function. The deformed core merely establishes the quantization axis of the system, which is important for determining the projection $\Lambda$.

# Chapter 4

# Deformed Two-Body Halos: Spheroidal-Well Model

In the previous chapter, features of two-body halos were discussed qualitatively through expanding the deformed wave functions in spherical partial waves. Here, quantitative calculations are presented using the deformed potential $U(\vec{r})$ approximated by a *finite* square well in prolate spheroidal coordinates. A spheroidal *infinite* square well was early used by Moszkowski [103] to discuss the properties of single-particle deformed orbitals. Merchant and Rae [104] investigated the continuum spectrum ($\epsilon>0$) of the spheroidal finite square well potential to calculate the particle decay widths of deformed nuclei. Since the main focus of this work is the behavior of bound single-particle orbitals very close to the $\epsilon=0$ threshold, particular attention was paid to a precise numerical solution of the Schrödinger equation in the limit of very small binding energies and/or large deformations.

## 4.1 Prolate Spheroidal Coordinates and Parametrization of Nuclear Shapes

Assuming the $z$-axis to be a symmetry axis of the nucleus, the coordinate transformation between the prolate spheroidal coordinates ($\xi$, $\eta$, $\phi$) and the cartesian coordinates ($x$,$y$,$z$) reads [105, 106, 107]:

$$x = a\sqrt{(\xi^2-1)(1-\eta^2)}\cos\phi, \tag{4.1}$$

$$y = a\sqrt{(\xi^2-1)(1-\eta^2)}\sin\phi, \tag{4.2}$$

$$z = a\xi\eta, \tag{4.3}$$

where $a > 0$, $1 \leq \xi < \infty$, $-1 \leq \eta \leq 1$, and $0 \leq \phi \leq 2\pi$. (Since the purpose of this study is to investigate the generic features of weakly bound states in a deformed potential, the analysis is limited to prolate shapes. However, the calculations can easily be extended to the oblate side through a simple coordinate transformation.) The confocal ellipses corresponding to surface of constant $\xi = \xi_0$ can be expressed as

$$\frac{x^2+y^2}{a^2(\xi_0^2-1)} + \frac{z^2}{a^2\xi_0^2} = 1 \tag{4.4}$$

with foci at (0,0,$\pm a$), minor axis $R_\perp = a\sqrt{\xi_0^2-1}$, and major axis $R_\parallel = a\xi_0$. The equi-surfaces of $\xi$ and $\eta$ are shown in Fig. 4.1(a). It is seen from Eq. (4.4) that the parameter $\xi_0$ defines the shape deformation of a system. Indeed, for $\xi_0 \gg 1$, the surface (4.4) becomes that of a sphere with the radius $a\xi_0$, while the limit $\xi_0 \to 1$ corresponds to a line segment. Following Ref. [103], the deformation parameter $\delta$ is

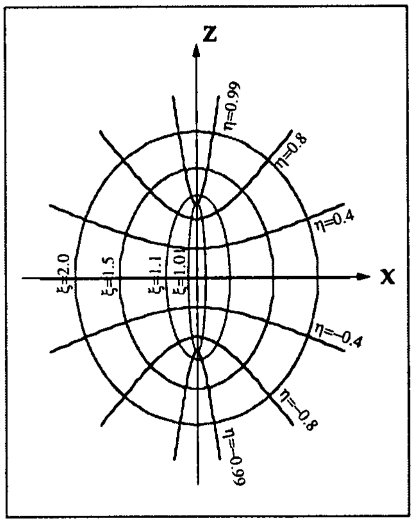


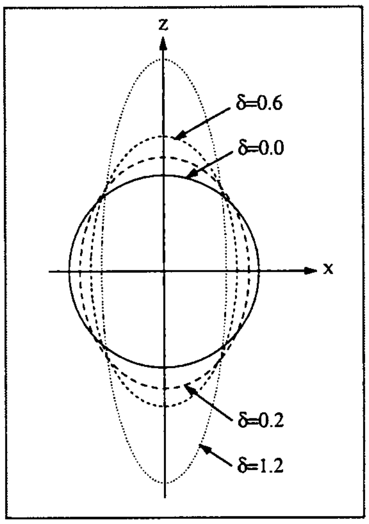


(a) (b)

**Figure 4.1**: (a) Prolate spheroidal coordinates $\xi$ and $\eta$ for a given value of $a$ and (b) shapes corresponding to quadrupole deformations $\delta$=0.0, 0.2, 0.6, and 1.2 assuming the volume conservation condition, Eq. (4.6).

introduced:

$$\delta = \left(\frac{R_\parallel}{R_\perp}\right)^{2/3} - 1 = \left(\frac{\xi_0^2}{\xi_0^2 - 1}\right)^{1/3} - 1. \tag{4.5}$$

The volume-conservation condition [the volume inside the surface (4.4) should not depend on $\delta$] yields

$$a = \frac{R_0}{(\xi_0^3 - \xi_0)^{1/3}}, \tag{4.6}$$

where $R_0$ is the corresponding spherical radius.

To find the relation between $\delta$ and other quadrupole deformation parameters, one can compare the macroscopic quadrupole moment of the surface (4.4)

$$Q_2 = \sqrt{\frac{16\pi}{5}}\langle r^2 Y_{20}\rangle = \frac{2}{5}R_0^2\delta\frac{\delta^2 + 3\delta + 3}{\delta + 1} \tag{4.7}$$

with those obtained using other shape parametrizations [108]. For instance, the parameter $\delta$ can be related to the oscillator deformation $\delta_{\rm osc}$ by

$$\delta = \left(\frac{3 + 1\delta_{\rm osc}}{3 - 2\delta_{\rm osc}}\right)^{2/3} - 1. \tag{4.8}$$

For small values of $\delta_{\rm osc}$, Eq. (4.8) gives $\delta = \frac{2}{3}\delta_{\rm osc}$. However, at a superdeformed shape ($\frac{R_\parallel}{R_\perp}$=2), both deformations are very close: $\delta_{\rm osc}$=0.6 while $\delta$=$2^{2/3}$–1=0.587. Figure 4.1(b) shows the family of shapes representing different deformations $\delta$ assuming the volume-conservation condition (4.6).

## 4.2 Schrödinger Equation in Prolate Spheroidal Coordinates

Consider a nucleon moving in the deformed spheroidal square-well potential given by

$$U(\xi) = \begin{cases} U_0 & \text{for } \xi \le \xi_0 \\ 0 & \text{for } \xi > \xi_0, \end{cases} \tag{4.9}$$

where $U_0$ is the depth of the potential well ($U_0$<0) and $\xi_0$ depends on $\delta$ through Eq. (4.5). Expressed in prolate spheroidal coordinates, the time-independent Schrödinger equation can be written as

$$\begin{aligned} \left\{\frac{\partial}{\partial\xi}\left[(\xi^2-1)\frac{\partial}{\partial\xi}\right] \right. &+ \left. \frac{\partial}{\partial\eta}\left[(1-\eta^2)\frac{\partial}{\partial\eta}\right] + \frac{\xi^2-\eta^2}{(\xi^2-1)(1-\eta^2)}\frac{\partial^2}{\partial\phi^2}\right\}\psi(\xi,\eta,\phi) \\ &= \frac{2ma^2(\xi^2-\eta^2)}{\hbar^2}\left[U(\xi)-\epsilon\right]\psi(\xi,\eta,\phi). \end{aligned} \tag{4.10}$$

Following Ref. [105], Eq. (4.10) can be separated by assuming $\psi(\xi,\eta,\phi) = R(\xi)S(\eta)\Phi(\phi)$. The functions $R$, $S$, and $\Phi$ are solutions of the ordinary differential equations:

$$\frac{d}{d\xi}\left[(\xi^2-1)\frac{dR_{\Lambda l}(c,\xi)}{d\xi}\right] - \left[\lambda_{\Lambda l} - c^2\xi^2 + \frac{\Lambda^2}{\xi^2-1}\right]R_{\Lambda l}(c,\xi) = 0, \quad (4.11)$$

$$\frac{d}{d\eta}\left[(1-\eta^2)\frac{dS_{\Lambda l}(c,\eta)}{d\eta}\right] + \left[\lambda_{\Lambda l} - c^2\eta^2 - \frac{\Lambda^2}{1-\eta^2}\right]S_{\Lambda l}(c,\eta) = 0, \quad (4.12)$$

$$\frac{d^2\Phi_\Lambda(\phi)}{d\phi^2} = -\Lambda^2\Phi_\Lambda(\phi), \quad (4.13)$$

where $\lambda_{\Lambda l}$ is the separation constant and

$$c = \begin{cases} c_{\text{int}} = a\sqrt{2m(\epsilon - U_0)}/\hbar & \text{for } \xi \le \xi_0 \\ ic_{\text{ext}} = ia\sqrt{-2m\epsilon}/\hbar & \text{for } \xi > \xi_0 \end{cases}. \quad (4.14)$$

In the following, $R_{\Lambda l}(c,\xi)$ and $S_{\Lambda l}(c,\eta)$ are referred to as the radial and angular spheroidal functions, respectively. For positive values of $\epsilon$, scattering solutions for the spheroidal square well were solved in Ref. [104]. Here we concentrate on bound states with $\epsilon < 0$.

The angular solutions in the present model, $S^{(1)}_{\Lambda l}(c,\eta)$, can be expressed in terms of a series of the associated Legendre functions of the first kind:

$$S^{(1)}_{\Lambda l}(c,\eta) = \sum_k^{\infty}{}' d_k^{\Lambda l}(c) P^{\Lambda}_{\Lambda+k}(\eta), \quad (4.15)$$

where the prime over the summation sign indicates that $k$=0, 2, ... if $(l-\Lambda)$ is even, and $k$=1, 3, ... if $(l-\Lambda)$ is odd [105, 107] (parity conservation).

The radial functions $R^{(p)}_{\Lambda l}(c,\xi)$ are expanded in terms of spherical Bessel functions $f_k^{(p)}(c\xi)$, where

$$f_k^{(p)}(c\xi) = \begin{cases} j_k(x) & \text{for } p = 1 \\ n_k(x) & \text{for } p = 2 \end{cases}. \quad (4.16)$$

Imposing usual boundary conditions on the radial wave functions, i.e., these functions must be finite at the origin and converge faster than $1/\xi$ at large distances, the internal radial function $R^{(1)}_{\Lambda l}(c,\xi)$ $(\xi \leq \xi_0)$ and the external radial function $R^{(3)}_{\Lambda l}(c,\xi)$ $(\xi > \xi_0)$ can be written as

$$\begin{aligned} R^{(p)}_{\Lambda l}(c,\xi) &= \left[\sum_k^{\infty}{}' \frac{(2\Lambda+k)!}{k!} d^{\Lambda l}_k(c)\right]^{-1} \left(\frac{\xi^2-1}{\xi^2}\right)^{\Lambda/2} \\ &\times \sum_k^{\infty}{}' i^{k+\Lambda-l} \frac{(2\Lambda+k)!}{k!} d^{\Lambda l}_k(c) f^{(p)}_{\Lambda+k}(c\xi), \end{aligned} \tag{4.17}$$

where $f^{(3)}_k(c\xi) = h^{(1)}_k(c\xi) = j_k(c\xi) + i n_k(c\xi)$.

The deformed single-particle wave function is given by

$$\psi_{\nu\Lambda\pi}(\xi,\eta,\phi) = \begin{cases} \sum_l^{\infty}{}' A_{\nu\Lambda l} R^{(1)}_{\Lambda l}(c_{\rm int},\xi) S^{(1)}_{\Lambda l}(c_{\rm int},\eta)\Phi_\Lambda(\phi) & \text{for } \xi \leq \xi_0 \\ \sum_l^{\infty}{}' B_{\nu\Lambda l} R^{(3)}_{\Lambda l}(ic_{\rm ext},\xi) S^{(1)}_{\Lambda l}(ic_{\rm ext},\eta)\Phi_\Lambda(\phi) & \text{for } \xi > \xi_0 \end{cases} \tag{4.18}$$

where $c_{\rm int}$ and $c_{\rm ext}$ are defined in Eq. (4.14) and $\nu$ is the excitation quantum number labeling orbitals having the same quantum numbers $\Lambda$ and $\pi$. By matching the internal and external wave functions at $\xi$=$\xi_0$ one finds the eigenenergies $\epsilon$ and the amplitudes $A_{\nu\Lambda l}$ and $B_{\nu\Lambda l}$ (cf. Appendix A for details).

## 4.3 Results

The single-particle energies of the finite spheroidal well with $U_0 = -80$ MeV and $R_0$=4 fm are shown in Fig. 4.2 as functions of deformation $\delta^\dagger$.

At spherical shape the orbitals are characterized by means of spherical quantum numbers $(n\ell)$. The deformed orbitals are labeled by parity $\pi$, angular momentum

$^\dagger$The plot of single-particle energies as a function of deformation is usually referred to as the Nilsson plot. The deformed single-particle states are usually called Nilsson orbitals [91].

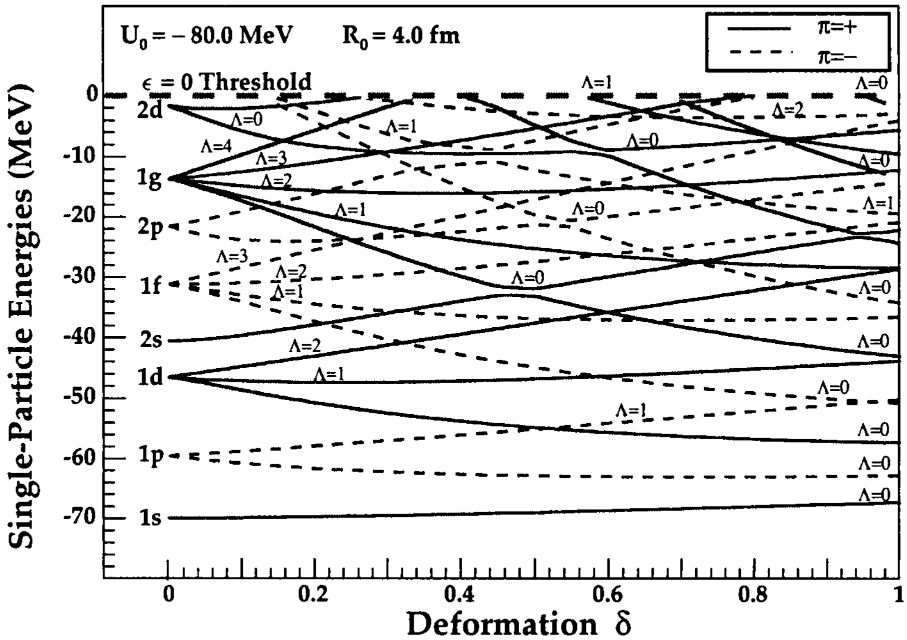


**Figure 4.2**: Single-particle energies of the finite spheroidal well with $U_0$=–80 MeV and $R_0$=4 fm as a function of deformation $\delta$. At spherical shape the orbitals are characterized by means of quantum numbers $(n\ell)$. The deformed orbitals are labeled by parity ($\pi$=+, solid line; $\pi$=–, dashed line) and orbital angular momentum projection onto the symmetry axis ($z$-axis), $\Lambda$.

projection $\Lambda$, and the excitation quantum number $\nu$ which specifies the energetic order of a single-particle orbital in a given $(\pi\Lambda)$-block, counting from the bottom of the well (e.g., $\nu$=1 corresponds to the lowest state, $\nu$=2 is the second state, and so on).

In the following, the deformed orbitals are labeled as $[\nu\Lambda\pi]$. For example, the $\Lambda$=1 orbital originating from the spherical shell $1d$ is referred to as [11+] (see Fig. 4.2). A fixed value of spherical radius $R_0$=4 fm (equivalent of the nuclear radius $r = r_0 A^{1/3}$, with $r_0$=1.2 fm and $A$=10) is used throughout all calculations. For a mere reference, some visual representations of deformed orbitals $[\nu\Lambda\pi]$ are also presented in Appendix C.

### 4.3.1 Properties of Deformed Halos

Figure 4.3 demonstrates the dependence of the single-particle rms radii on deformation $\delta$ for the [20+] and [20−] orbitals. It is clearly seen that deformation gives rise to the increase in the rms radii. This effect is particularly dramatic for the [20+] orbital. Only small deviation from spherical shape in the [20+] orbital (which originates from the spherical $1d$ state) is sufficient to produce a halo effect. As discussed below, this can be understood in terms of increased $s$ component in the [20+] wave function (see also Appendix B). For the negative-parity halo orbital [20−], the effect is less pronounced. However, its rms radius is still rather large at high deformations.

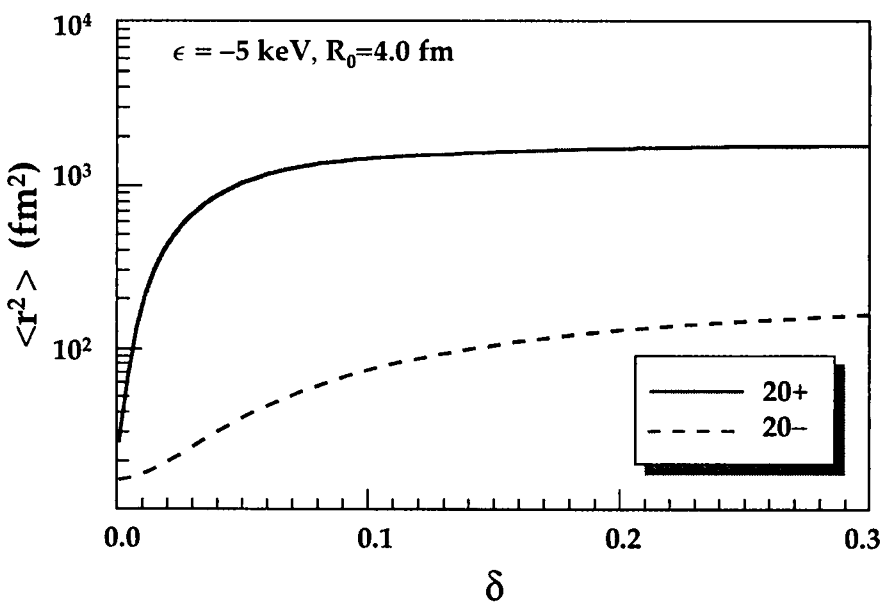


**Figure 4.3**: Single-particle rms radii for the [20+] and [20−] orbitals as functions of deformation $\delta$ at a fixed binding energy $\epsilon = -5$keV.

The dependence of the single-particle rms radius on binding energy is illustrated in Fig. 4.4 (spherical shape) and Fig. 4.5 (superdeformed shape). (In calculations, the binding energy was varied by adjusting the well depth $U_0$.) The spherical case has been discussed in detail in Ref. [19]; here it is shown for the mere reference only. In all cases the asymptotic conditions (3.23) and (3.24) are met rather quickly. Indeed, in the considered range of binding energy the values of $\langle r^2 \rangle$ for the $1s$ state shown in Fig. 4.4 and the [10+], [20+], and [30+] orbitals of Fig. 4.5(a) approach an asymptotic limit [$(-\epsilon)^{-1}$ dependence], and similar holds for the $1p$ state and [10–], [20–], [11–], and [21–] orbitals [see Fig. 4.5(b)] which behave as $(-\epsilon)^{-1/2}$ at low binding energy. The remaining states do not exhibit any halo effect, as expected.

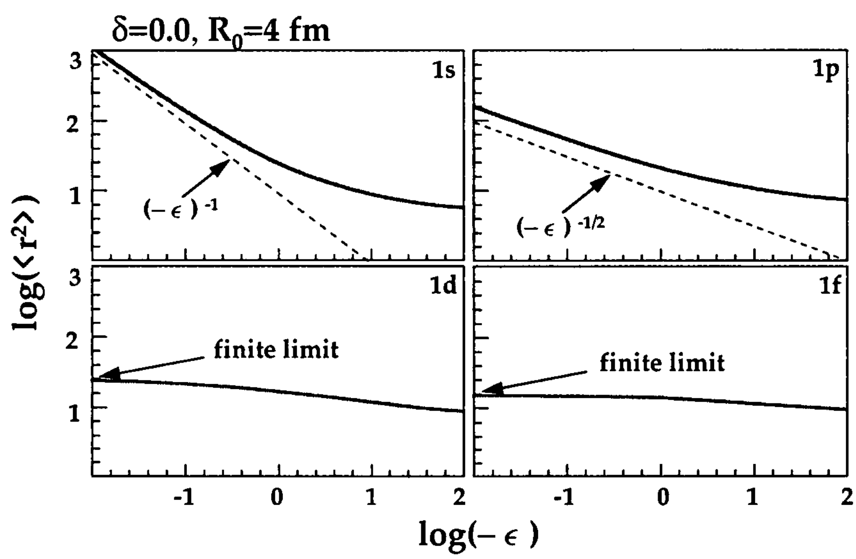


**Figure 4.4**: Dependence of the single-particle rms radius on binding energy $\epsilon$ at $\delta$=0 (spherical shape) and $R_0$=4 fm. The potential depth is adjusted in each case to obtain the desired value of $\epsilon$. The values of $\langle r^2 \rangle$ for $1s$ and $1p$ orbitals diverge at small binding energies according to Eqs. 3.23 and 3.24.

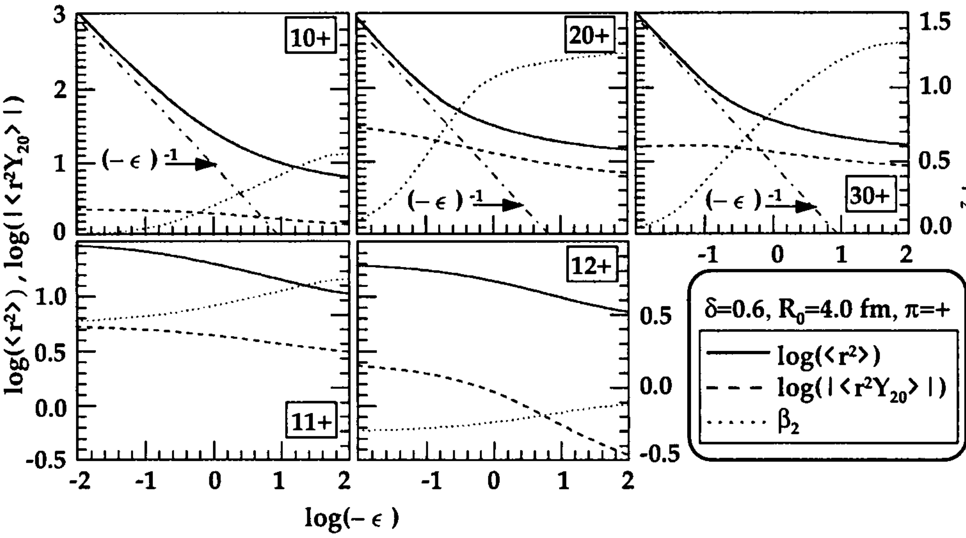


(a)

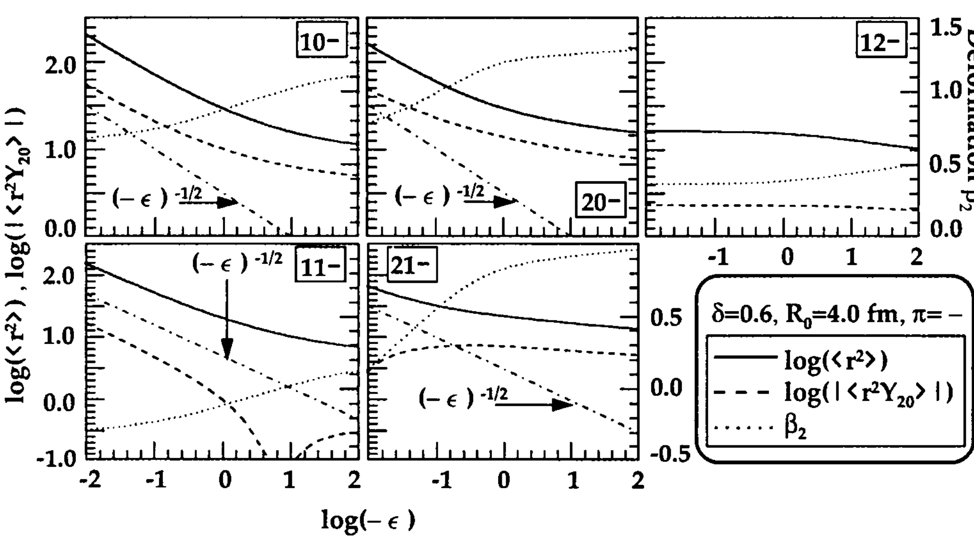


(b)

**Figure 4.5**: Binding energy dependence of $\langle r^2 \rangle$ (solid line), $\langle r^2 Y_{20} \rangle$ (dashed line), and $\beta_2$ (dotted line) for several (a) $\pi = +$ and (b) $\pi = -$ orbitals at $\delta$=0.6 (superdeformed shape). The asymptotic limits discussed in Sec. 3.2 are indicated.

In Fig. 4.5, deformation properties of single-particle orbitals, namely the intrinsic quadrupole moments $\langle r^2 Y_{20}\rangle$ and quadrupole deformations $\beta_2$, are also displayed as functions of binding energy at $\delta$=0.6. It is seen that the asymptotic limits discussed in Sec. 3.2 are reached at low values of $\epsilon$ practically in all cases. In particular, the values of $\beta_2$ for the positive-parity halo orbitals ($\pi$=+, $\Lambda$=0) approach zero with $\epsilon \to 0$ [see Eq. (3.35)], those for the negative-parity halo states with $\Lambda = 0$ approach the limit of 0.63, and the value of $\beta_2$ for the [11−] orbital is close to the value of −0.31 [see Eq. (3.37)]. The only exception is the [21−] orbital which at deformation $\delta = 0.6$ contains only 31% of the $\ell = 1$ component (see also discussion below), hence the positive contribution of the $1f$ state to $\langle r^2 Y_{20}\rangle$ still dominates.

To illustrate the interplay between the core deformation and that of the valence particle, the following quadrupole deformations are displayed in Fig. 4.6: (i) quadrupole deformation $\beta_2$ of the valence orbital, (ii) quadrupole deformation of the core, and (iii) total quadrupole deformation of the system. Here we assume that the core consists of *all* single-particle orbitals lying energetically below the valence orbital, and that each state (including the valence one) is occupied by two particles. Following the discussions in Chapter 3, it is convenient to rewrite Eq. (3.38) in the form:

$$\beta_2(\text{total}) = \frac{\beta_2(\text{c})\langle r^2\rangle_\text{c} + \beta_2(\text{v})\langle r^2\rangle_\text{v}}{\langle r^2\rangle_\text{c} + \langle r^2\rangle_\text{v}} = \frac{\beta_2(\text{v}) + \chi\beta_2(\text{c})}{1+\chi}, \tag{4.19}$$

where

$$\chi \equiv \frac{\langle r^2\rangle_\text{c}}{\langle r^2\rangle_\text{v}}. \tag{4.20}$$

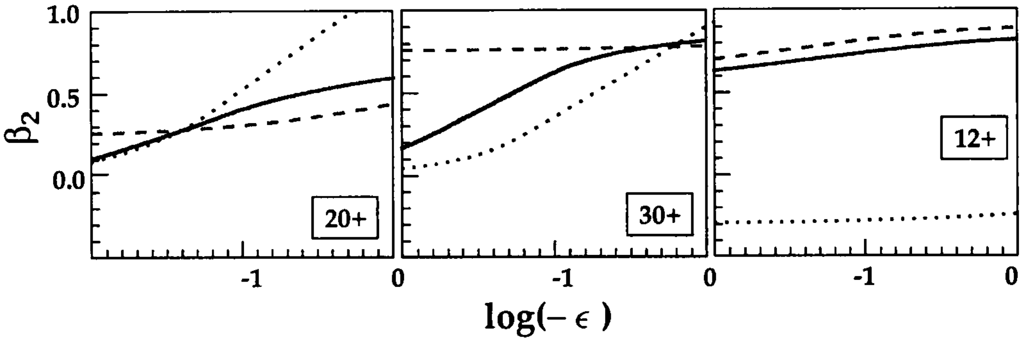


(a)

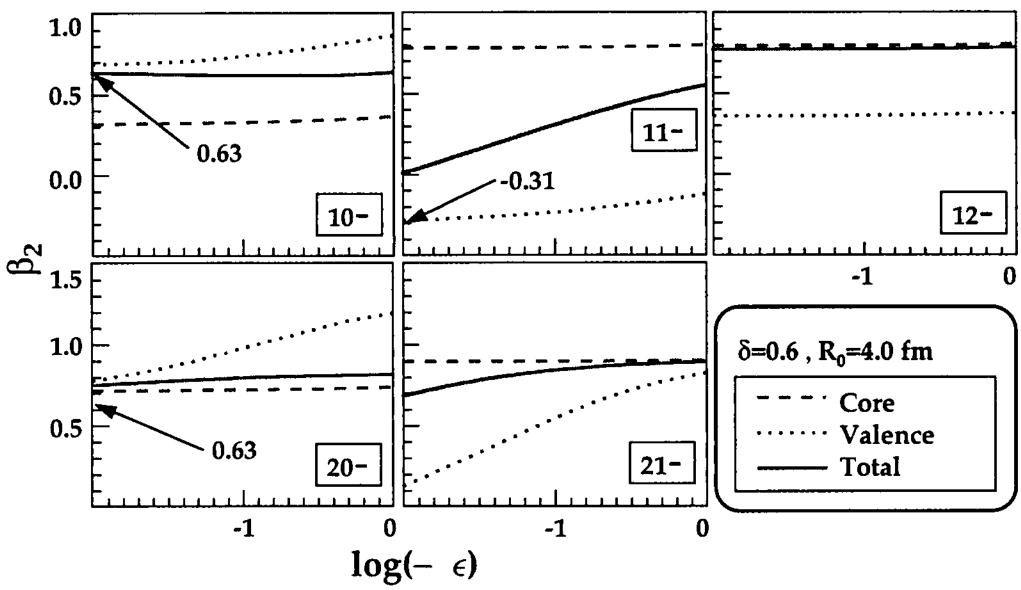


(b)

**Figure 4.6**: Quadrupole deformation $\beta_2$ of the valence orbital (dotted line), that of the core (dashed line), and the total quadrupole deformation of the system (solid line) as a function of the binding energy of the indicated valence orbitals of (a) positive and (b) negative parities. Calculations were performed for $R_0$=4 fm and $\delta$=0.6.

For the halo states, $\chi \rightarrow 0$ and $\beta_2(\text{total}) \rightarrow \beta_2(\text{v})$. The results shown in Fig. 4.6 nicely illustrate this behavior. For very small binding energy, the total deformation of the system coincides with that of valence, *regardless* of the core deformation. These results clearly indicate the deformation decoupling of the valence nucleon and the core. A nice example of this decoupling has been discussed in Ref. [44] in which the halo proton in $^8$B occupying the $1p_{3/2}$, $\Lambda$=1 weakly bound orbit (oblate density distribution) greatly reduces the large quadrupole moment of the prolate core.

The density $\rho$ and the $\rho \times r^2$ distributions projected onto the $x$-$z$ plane (linear and logarithmic scales) for a negative-parity halo system (core+2 valence particles) are shown in Figs. 4.7 and 4.8, respectively. In these figures, two nucleons in the valence orbital [11−] are weakly bound ($\epsilon = -5$ keV) in the deformed potential well with $\delta = 0.2$. According to Fig. 4.7, the two valence particles give rise to an oblate deformation of the system, in spite of the prolate deformation of the core and the prolate shape of the underlying spheroidal well ($\delta$=0.2). This nicely illustrates that the quadrupole deformation of a halo system can be solely determined by the intrinsic structure of a weakly bound orbital which is decoupled from the core.

The decoupling of valence particles is better illustrated in the $\rho \times r^2$ distribution plots (Fig. 4.8). This result demonstrates the importance of the radial contribution to the quadrupole moment. In this context, Fig. 4.9 shows the values of $\Theta^{(\text{ext})}_{\nu\Lambda\pi}$ [Eq. (5.42)] for various deformed orbitals at $\delta = 0.6$. It is interesting to note that at low binding energies the values of $\Theta^{(\text{ext})}_{\nu\Lambda\pi}$ become close to one for all (halo and non-halo) orbitals considered. (According to Eq. (5.42), $\Theta^{(\text{ext})}_{10-}$ is expected to approach

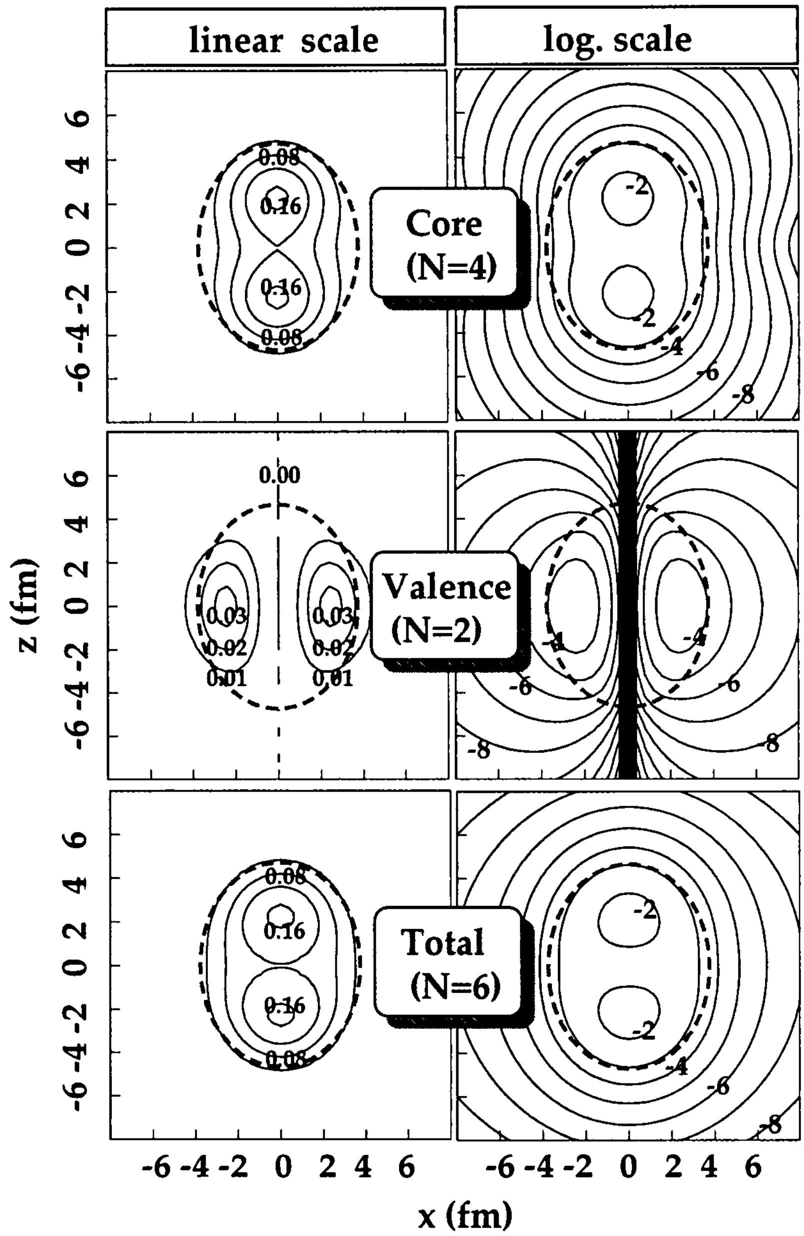


**Figure 4.7**: Contour plots of the density $\rho$ distribution in the $x$-$z$ plane shown in linear (left) and logarithmic (right) scales. Density distributions for the core (top), valence orbital [11−] (middle), and total matter (bottom) are compared. The deformation of the spheroidal well is assumed to be $\delta$=0.2; the corresponding prolate shape is indicated by a dashed line.

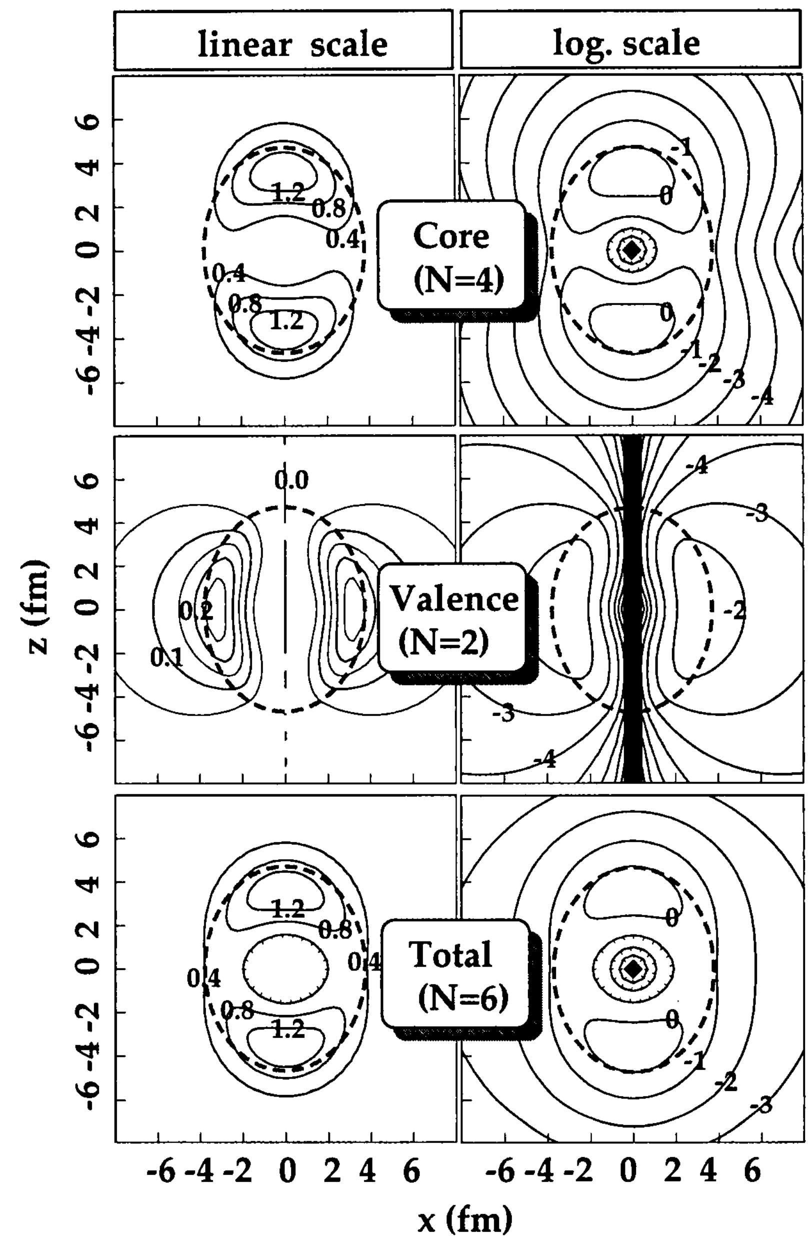


**Figure 4.8**: Same as in Fig. 4.7 except for the $\rho \times r^2$ distribution.

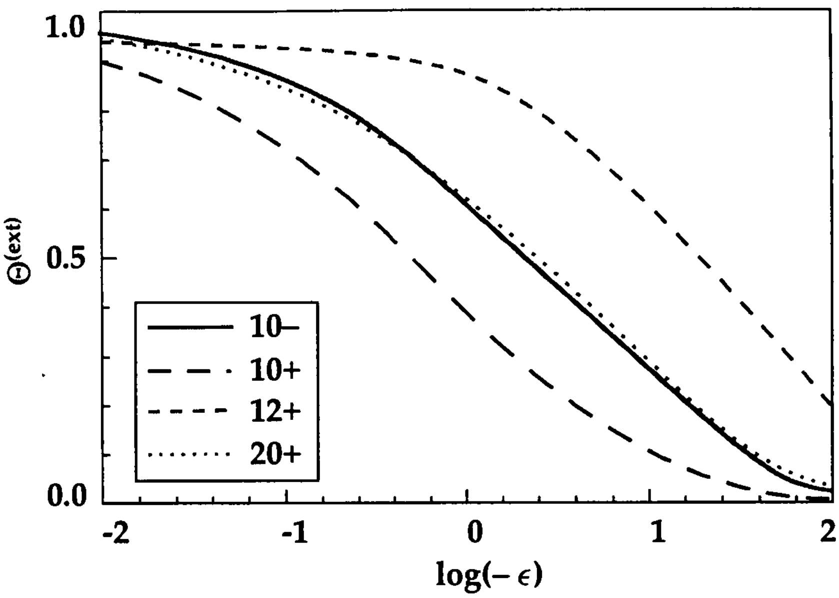


**Figure 4.9**: External contribution to the quadrupole moment, $\Theta^{(\mathrm{ext})}$ [ Eq. (5.42)], as a function of binding energy for various deformed orbitals ($\delta$=0.6).

unity for the [10−] orbital.) In other words, the quadrupole moment strongly depends on the spatial extension of the wave function in the limit of vanishing $\epsilon$.

Figure 4.10 displays the probability $P^{(\mathrm{ext})}_{\nu\Lambda\pi}$ [Eq. (3.18)] to find the neutron in the classically forbidden region ($\xi > \xi_0$) as a function of $\epsilon$ for six superdeformed states with different values of $\Lambda$. At low values of binding energy, the $\ell$=0 component completely dominates the structure of the positive-parity halo orbitals and $P^{(\mathrm{ext})}_{\nu 0+} \rightarrow$ 1. Similarly, the values of $P^{(\mathrm{ext})}_{\nu\Lambda -}$ for the negative-parity halo orbitals, [10−] and [11−], exceed 50% at low binding energy. The reduction of $P^{(\mathrm{ext})}_{\nu\Lambda\pi}$ for the [21−] orbital can be understood in terms of large contribution from the $\ell = 3$ component. (Indeed, the results in the following section indicate that at $\epsilon = -5$keV and $\delta$=0.6, for the [21−] orbital the amplitude of $f$ and $p$ components are 59% and 31%, respectively.)

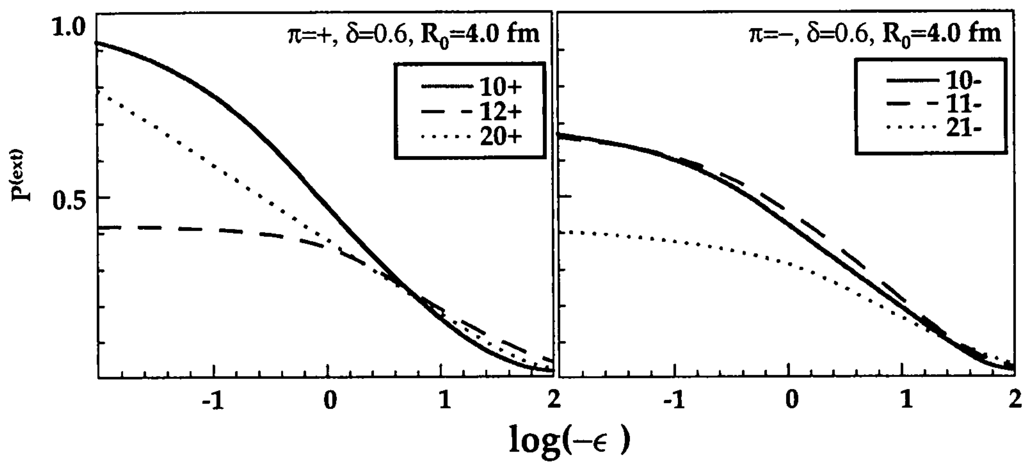


**Figure 4.10**: Probability $P^{(\text{ext})}$ [Eq. (3.18)] to find the neutron in the classically forbidden region, $\xi > \xi_0$, as a function of $\epsilon$ for both $\pi = +$ (left figure) and $\pi = -$ (right figure) states.

### 4.3.2 Radial Form Factors

The radial form factors $R_{\nu\ell\Lambda}(r)$ appearing in the multipole decomposition [Eq. (3.2)] carry information about the spatial extension of the wave function. They can be obtained by the angular integration

$$R_{\nu\ell\Lambda}(r) = \int \psi_{\nu\Lambda\pi}(\vec{r}) Y^*_{\ell\Lambda}(\theta, \phi)\, d\Omega. \tag{4.21}$$

Since in the present calculations the total wave function $\psi_{\nu\Lambda\pi}(\vec{r})$ is normalized to unity, the integral

$$P_\ell(\nu\Lambda\pi) \equiv \int_0^\infty |R_{\nu\ell\Lambda}(r)|^2 r^2\, dr \tag{4.22}$$

represents the probability to find the partial wave $\ell$ in the state $[\nu\Lambda\pi]$. This implies

$$\sum_\ell P_\ell(\nu\Lambda\pi) = 1. \tag{4.23}$$

Figures 4.11 and 4.12 display the radial form factors for several orbitals in a superdeformed well assuming the subthreshold binding energy of $\epsilon = -5$ keV. For the positive-parity halo orbitals (Fig. 4.11), the $\ell$=0 component dominates at this extremely low binding energy, in spite of a very large deformation. According to the discussions in Sec. 3.2, the value of $P_{\ell=0}(\nu 0+)$ approaches one at small binding energies. In other words, the positive-parity halos behave at low values of $\epsilon$ like $s$ waves. It is interesting to note that both the [20+] and [30+] orbitals are dominated by the $2s$ component; the corresponding $\ell$=0 form factors have only one node. For the negative-parity halo orbitals (Fig. 4.12), the $p$ component does not dominate the wave function completely (cf. Sec. 3.2) but a significant excess of $p$-wave at large distances is clearly seen. The radial decomposition of non-halo orbitals ($\Lambda > 1$) shown in Figs. 4.11 and 4.12 depend very weakly on binding energy; it reflects the usual multipole mixing due to the deformed potential.

In Fig. 4.13, the dependence of the radial form factors on binding energy is shown for the positive-parity halo orbital [20+]. As seen in Fig. 4.13, in the limit of weak binding the $\ell = 0$ partial-wave component becomes spatially extended with increasing $P_0(20+)$. The results presented in Figs. 4.11, 4.12, and 4.13 illustrate the fact that the multipole decomposition of the deformed level depends on *both* deformation and binding energy.

Figures 4.14(a) ($\pi = +$) and 4.15(a) ($\pi = -$) show contour maps of $P_\ell(\nu\Lambda\pi)$ for the lowest $\Lambda$=0 orbitals as functions of $\epsilon$ and $\delta$. The structure of the [10+] level, originating from the spherical $1s$ state, is completely dominated by the $\ell = 0$ component, even at very large deformations. A rather interesting pattern is seen

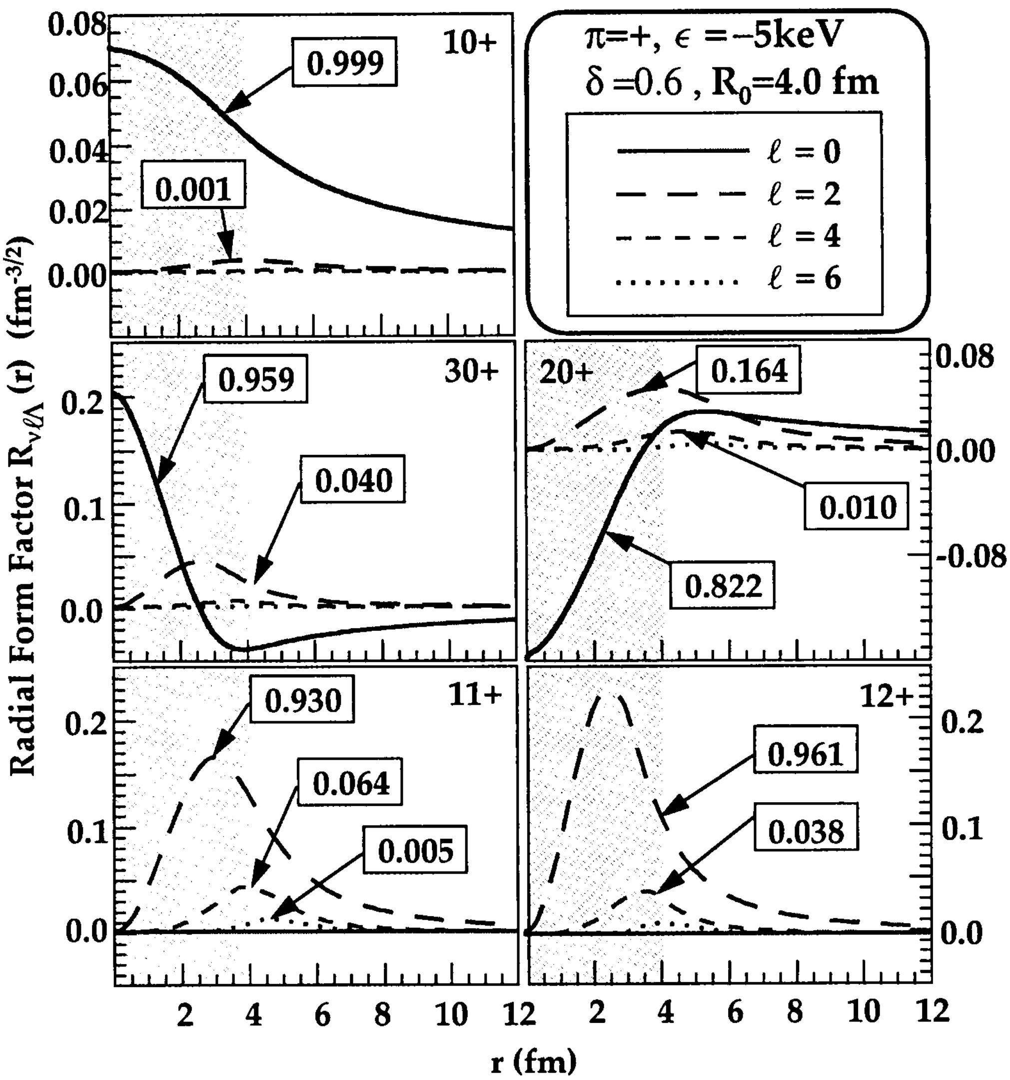


**Figure 4.11**: Radial form factors [Eq. (4.21)] for several $\pi$=+ orbitals in a superdeformed well ($\delta$=0.6, $R_0$=4 fm) at the 'subthreshold' binding energy $\epsilon = -5$ keV. Shaded area corresponds to $r \leq R_0$. The probability $P_\ell(\nu\Lambda+)$ [Eq. (4.22)] is also indicated.

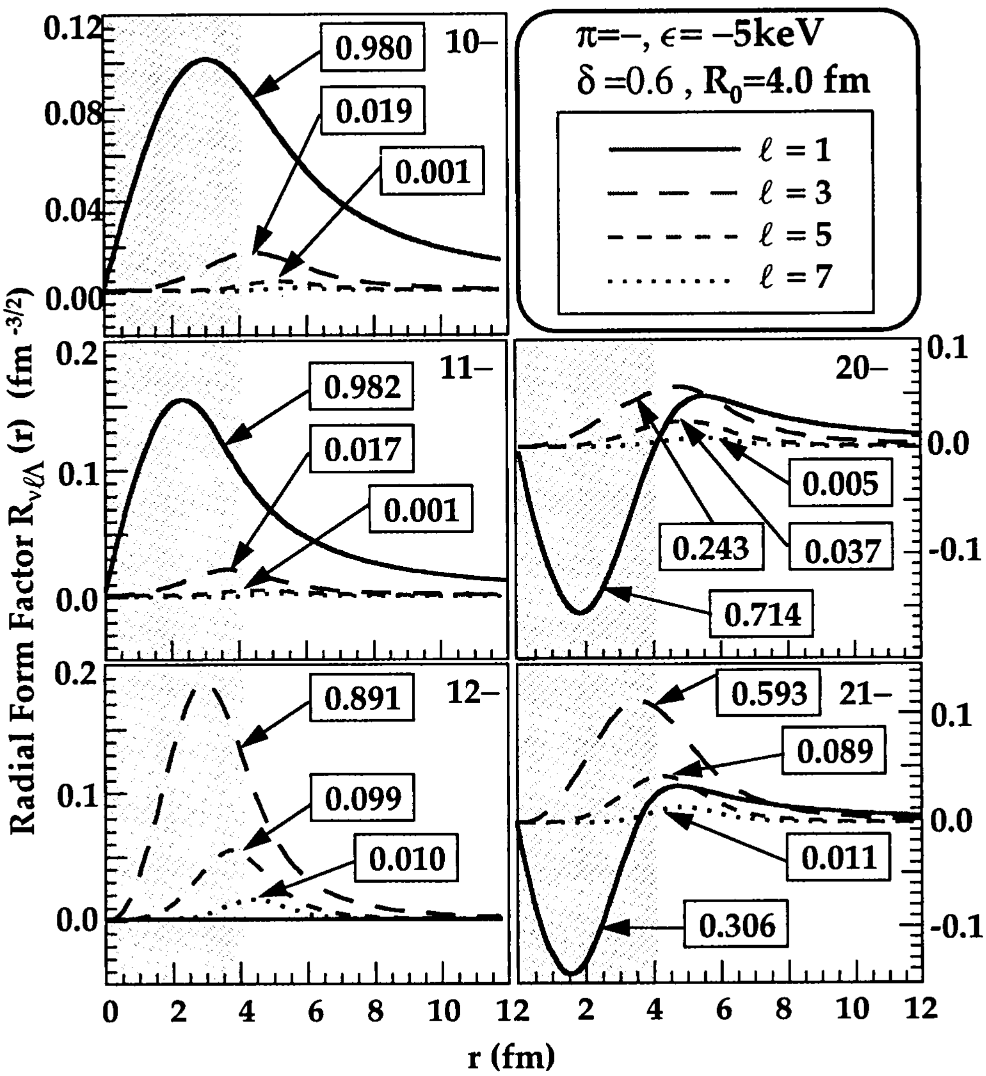


**Figure 4.12**: Same as in Fig. 4.11 except for $\pi = -$ orbitals.

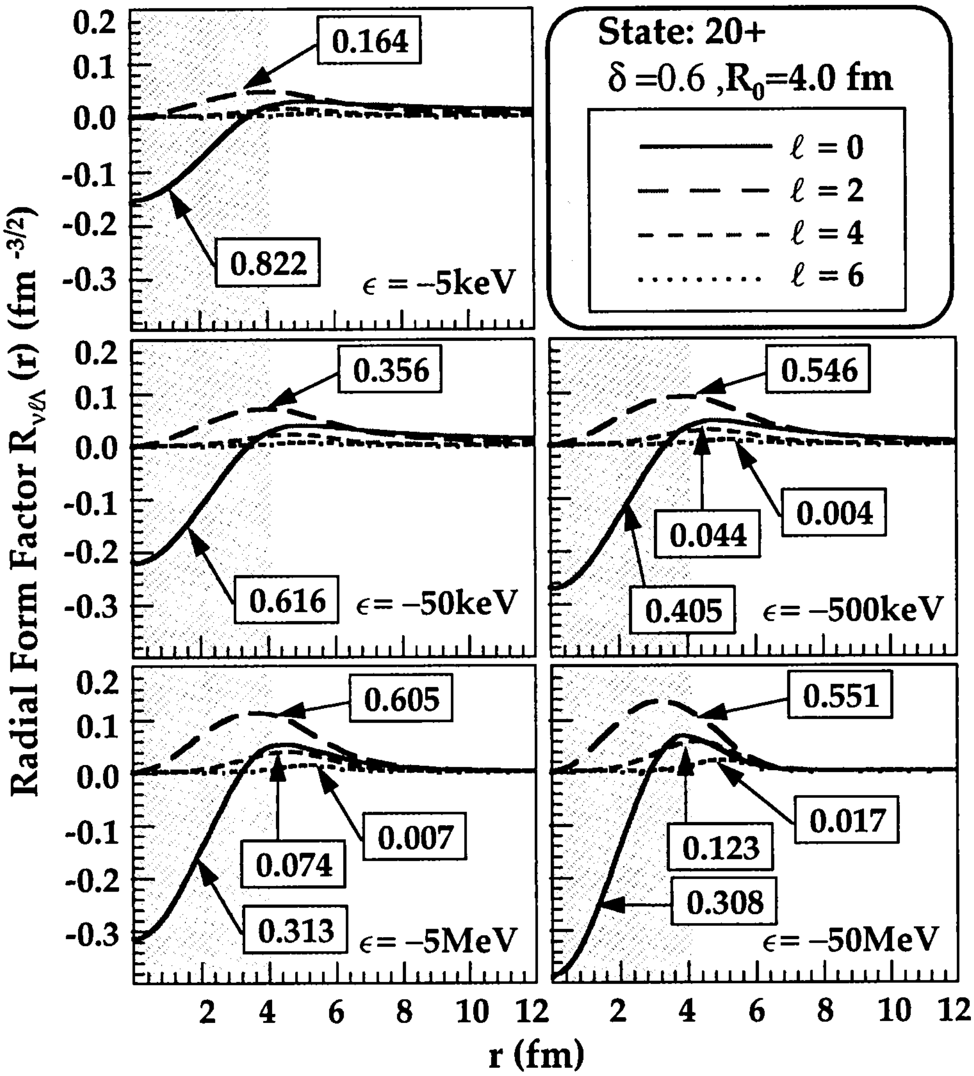


**Figure 4.13**: Radial form factors [Eq. (4.21)] for the [20+] orbital in a superdeformed well ($\delta$=0.6, $R_0$=4 fm) at various binding energies. Shaded area corresponds to $r \leq R_0$. The probability $P_\ell(20+)$ [Eq. (4.22)] is also indicated.

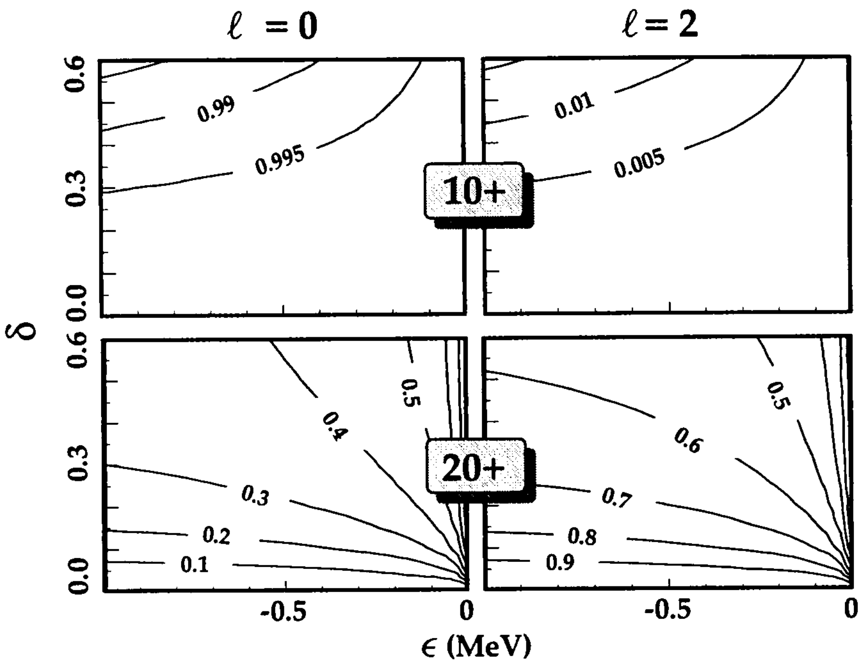


(a)

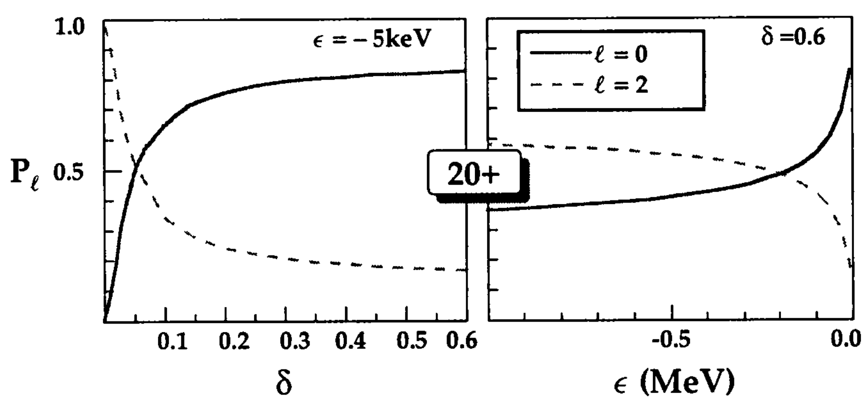


(b)

**Figure 4.14**: (a) Contour maps of probabilities $P_0$ and $P_2$ [Eq. (4.22)] for the [10+] (top) and [20+] (bottom) levels as functions of deformation $\delta$ and binding energy $\epsilon$. (b) Probabilities $P_0$ and $P_2$ for the [20+] orbital as a function of $\delta$ at $\epsilon = -5$ keV (left) and as a function of $\epsilon$ at $\delta = 0.6$ (right). Calculations were performed for $R_0$=4 fm.

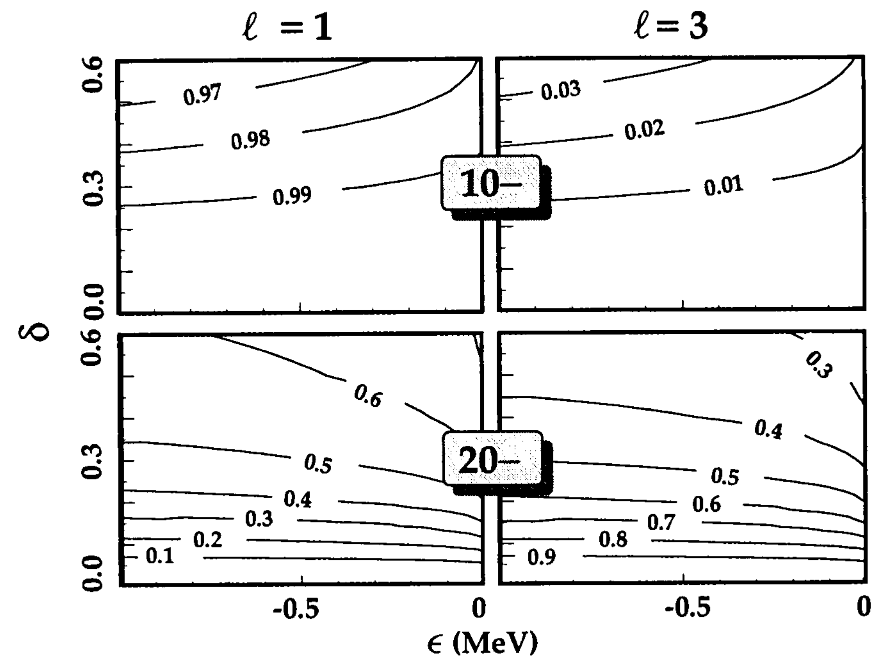


(a)

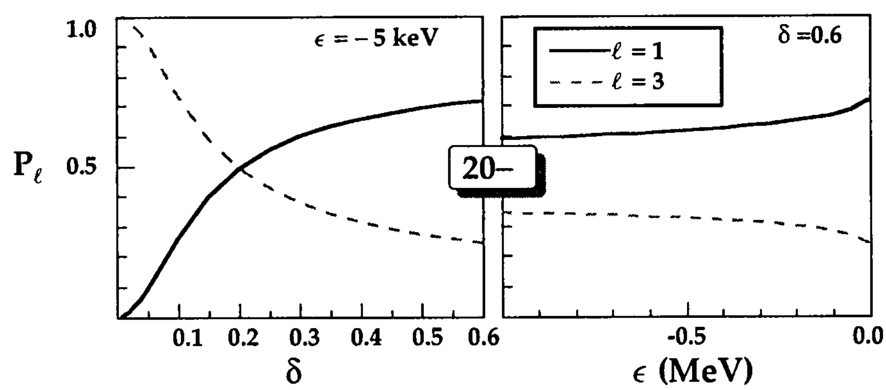


(b)

**Figure 4.15**: (a) Contour maps of probabilities $P_1$ and $P_3$ [Eq. (4.22)] for the [10-] (top) and [20-] (bottom) levels as functions of deformation $\delta$ and binding energy $\epsilon$. (b) Probabilities $P_1$ and $P_3$ for the [20−] orbital as a function of $\delta$ at $\epsilon = -5$ keV (left) and as a function of $\epsilon$ at $\delta = 0.6$ (right). Calculations were performed for $R_0$=4 fm.

in the diagram for the [20+] orbital originating from the spherical 1$d$ state. The $\ell = 2$ component dominates at low and medium deformations, and the corresponding probability $P_{\ell=2}$ slowly decreases with $\delta$, at large deformations approaching the (constant) asymptotic limit [see also Fig. 4.14(b)]. However, a similar effect, specifically the decrease of the $\ell = 2$ component, is seen when approaching the $\epsilon = 0$ threshold [see Fig. 4.14(b)]. In the language of the perturbation theory [109], this rapid transition comes from the coupling to the low-energy $\ell = 0$ continuum; the $\ell = 0$ form factor of the [20+] orbital shows, at low values of $\epsilon$, a one-nodal structure characteristic of the 2$s$ state (see Fig. 4.13). At low deformations, the amplitude of the $s$ component in the [20+] state is proportional to $\delta$. Remembering that for the $\ell = 0$ state the norm behaves as $(-\epsilon)^{-1/4}$, one can conclude that at low values of $\delta$ and $\epsilon$ the contours of constant $P_{\ell=0}$ correspond to the power law $\delta^2 \propto (-\epsilon)^{1/2}$. The result displayed in Fig. 4.14(a) tells us that the $s$ component takes over very quickly even if deformation $\delta$ is small. (A similar analysis, for the $1/2^+$ ground state of $^{11}$Be, was discussed in Ref. [100] in the weak-coupling scheme.)

The partial-wave probabilities calculated for the negative-parity halo states [10−] and [20−] presented in Fig. 4.15(a) do not show such a dramatic rearrangement around the threshold. Namely, the [10−] orbital retains its $\ell = 1$ structure in the whole deformation region considered, and the structure of the [20−] state at large deformations can be viewed in terms of a mixture of $p$ and $f$ waves. In the latter case, there is a clear tendency to increase the $\ell = 1$ contribution at low binding energies, but this effect is much weaker compared to the [20+] case discussed above [see Fig. 4.15(b)].

# Chapter 5

# Deformations of Weakly Bound Medium-Mass Nuclei. Self-Consistent Calculations

This chapter presents the results of self-consistent calculations of deformation properties of neutron-rich nuclei from the $N \approx 28$ mass region. The theoretical works of Refs. [82] and [110] are reviewed in the context relevant to the aim of this study. Ground state properties of sulfur isotopes were investigated in the framework of microscopic self-consistent mean-field approaches based on realistic effective interactions: the HF method with the Skyrme effective interaction and the RMF approach. We concentrate on the correlation between the neutron-skin formation and deformation properties of protons and neutrons.

## 5.1 Skyrme-Hartree-Fock Model

The Skyrme interaction [111] is the most popular effective force used in HF calculations today; it is a zero-range ansatz to the microscopic effective interaction and composed of two- and three-body interaction terms:

$$V = \sum_{i<j} v_{ij}^{(2)} + \sum_{i<j<k} v_{ijk}^{(3)}. \tag{5.1}$$

The two-body part of the Skyrme interaction can be expressed as

$$\begin{aligned} v_{12}^{(2)} &= t_0(1+x_0P_\sigma)\delta(\vec{r}_1-\vec{r}_2) + \frac{t_1}{2}\left[\delta(\vec{r}_1-\vec{r}_2)k^2 + k'^2\delta(\vec{r}_1-\vec{r}_2)\right] \\ &\quad + t_2\vec{k}'\cdot\delta(\vec{r}_1-\vec{r}_2)\vec{k} + it_4(\vec{\sigma}_1+\vec{\sigma}_2)\cdot\vec{k}'\times\delta(\vec{r}_1-\vec{r}_2)\vec{k}, \end{aligned} \tag{5.2}$$

with

$$\vec{k} = (\vec{\nabla}_1 - \vec{\nabla}_2)/2i \quad (\vec{k}' = \vec{k}^\dagger), \tag{5.3}$$

$$P_\sigma = (1+\vec{\sigma}_1\cdot\vec{\sigma}_2)/2. \tag{5.4}$$

In the state of relative motion, the first two terms in Eq. (5.2) represent $s$-wave interaction while the last two terms reflect $p$-wave interaction [112]. The three-body term is the zero-range potential of the form

$$v_{123}^{(3)} = t_3\delta(\vec{r}_1-\vec{r}_2)\delta(\vec{r}_2-\vec{r}_3). \tag{5.5}$$

It can be shown [112] that by averaging over the coordinate of the third particle, the above three-body term can be approximated by a density-dependent force

$$\frac{t_3}{6}(1+x_3P_\sigma)\rho^\alpha(\vec{R})\delta(\vec{r}_1-\vec{r}_2) \tag{5.6}$$

where

$$\alpha = x_3 = 1, \tag{5.7}$$

$$\vec{R} = (\vec{r}_1 + \vec{r}_2)/2. \tag{5.8}$$

Assuming that the many-body wave functions can be approximated by Slater determinants (product states), the expectation value of the total energy can be expressed in terms of the energy density $\mathcal{H}(\vec{r})$ as [112, 113]

$$E = \langle\Phi|[T+V]|\Phi\rangle = \int \mathcal{H}(\vec{r}) d^3r. \tag{5.9}$$

The energy density $\mathcal{H}$ can be defined in terms of the nucleon densities $\rho_\tau$, kinetic energy $\mathcal{K}_\tau$, and spin densities $\vec{J}_\tau$ where $\tau$ denotes the isospin quantum number ($\tau = +1$ for a neutron and $\tau = -1$ for a proton) :

$$\begin{aligned}
\mathcal{H}(\vec{r}) \;=\; & \frac{\hbar^2}{2m}\mathcal{K}(\vec{r}) + \frac{t_0}{2}\left[\left(1+\frac{x_0}{2}\right)\rho^2 - \left(x_0+\frac{1}{2}\right)\sum_\tau \rho_\tau^2\right] + \frac{1}{4}(t_1+t_2)(\rho\mathcal{K} - j^2) \\
& + \frac{1}{8}(t_2-t_1)\sum_\tau(\rho_\tau\mathcal{K}_\tau - j_\tau^2) + \frac{1}{16}(t_2-3t_1)\rho\nabla^2\rho \\
& + \frac{1}{32}(3t_1+t_2)\sum_\tau(\rho_\tau\nabla^2\rho_\tau) + \frac{1}{16}(t_1-t_2)\sum_\tau \vec{J}_\tau^2 + \frac{t_3}{12}\left(1+\frac{x_3}{2}\right)\rho^{\alpha+2} \\
& - \frac{t_3}{12}\left(\frac{1}{2}+x_3\right)\rho^\alpha\sum_\tau\rho_\tau^2 - \frac{t_4}{2}\left[\rho\vec{\nabla}\cdot\vec{J} + \sum_\tau(\rho_\tau\vec{\nabla}\cdot\vec{J}_\tau)\right] + \mathcal{H}_C(\vec{r}).
\end{aligned} \tag{5.10}$$

In the present calculation, the Coulomb interaction term $\mathcal{H}_C$ in Eq. (5.10) consists of both the direct and exchange terms, namely

$$\mathcal{H}_C = \frac{1}{2}e^2\int d^3r'\rho_{-1}(\vec{r})\frac{\rho_{-1}(\vec{r}')}{|\vec{r}-\vec{r}'|} - \frac{3}{4}e^2\left(\frac{3}{\pi}\right)^{1/3}[\rho_{-1}(\vec{r})]^{4/3}, \tag{5.11}$$

where the latter term has been approximated by the local (Slater) form. The densities and current densities, $\rho_\tau$, $\mathcal{K}_\tau$, $\vec{j}_\tau$, and $\vec{J}_\tau$, found in Eq. (5.10) depend on the single-particle wave functions $\phi_i$ by

$$\rho_\tau(\vec{r}) = \sum_{i,\sigma} |\phi_i(\vec{r},\sigma,\tau)|^2, \tag{5.12}$$

$$\mathcal{K}_\tau(\vec{r}) = \sum_{i,\sigma} |\vec{\nabla}\phi_i(\vec{r},\sigma,\tau)|^2, \tag{5.13}$$

$$\vec{j}_\tau(\vec{r}) = \sum_{i,\sigma} \mathrm{Im}\left[\phi_i^*(\vec{r},\sigma,\tau)\vec{\nabla}\phi_i(\vec{r},\sigma,\tau)\right], \tag{5.14}$$

$$\vec{J}_\tau(\vec{r}) = -i\sum_{i,\sigma,\sigma'} \phi_i^*(\vec{r},\sigma,\tau)\left[\vec{\nabla}\phi_i(\vec{r},\sigma',\tau)\times\langle\sigma|\vec{\sigma}|\sigma'\rangle\right], \tag{5.15}$$

where $\sigma$ is the spin quantum number. Here, it is to be noted that the quantities $\rho$, $\mathcal{K}$, $\vec{j}$, and $\vec{J}$ indicate the isoscaler densities (e.g., $\rho{=}\sum_\tau \rho_\tau{=}\rho_{+1}{+}\rho_{-1}$, etc.). Using above energy density $\mathcal{H}$, the variation of $E$ with respect to the normalized single-particle states $\phi_i$,

$$\frac{\delta}{\delta\phi_i}\left(E - \sum_i \epsilon_i \int |\phi_i(\vec{r})|^2 d^3r\right) = 0, \tag{5.16}$$

leads to the HF equations with the one-body Skyrme-HF Hamiltonian:

$$h_\tau = -\vec{\nabla}\cdot\frac{\hbar^2}{2m_\tau^*(\vec{r})}\vec{\nabla} + U_\tau(\vec{r}) + \frac{1}{2i}(\vec{\nabla}\cdot\vec{I}_\tau(\vec{r}) + \vec{I}_\tau(\vec{r})\cdot\vec{\nabla}) - i\vec{W}_\tau(\vec{r})\cdot(\vec{\nabla}\times\vec{\sigma}). \tag{5.17}$$

(See Ref. [112] for details.) The additional quantities appearing in Eq. (5.17) are given by

$$\frac{\hbar^2}{2m_\tau^*(\vec{r})} = \frac{\hbar^2}{2m} + \frac{1}{4}(t_1+t_2)\rho + \frac{1}{8}(t_2-t_1)\rho_\tau, \tag{5.18}$$

$$\vec{I}_\tau(\vec{r}) = -\frac{1}{2}(t_1+t_2)\vec{j} - \frac{1}{4}(t_2-t_1)\vec{j}_\tau, \tag{5.19}$$

$$\vec{W}_\tau(\vec{r}) = \frac{t_4}{2}\vec{\nabla}(\rho+\rho_\tau) - \frac{1}{8}(t_2-t_1)\vec{J}_\tau, \tag{5.20}$$

and

$$U_\tau(\vec{r}) = t_0\left[\left(1+\frac{x_0}{2}\right)\rho - \left(x_0+\frac{1}{2}\right)\rho_\tau\right] - \frac{1}{8}(3t_1-t_2)\nabla^2\rho + \frac{1}{16}(3t_1+t_2)\nabla^2\rho_\tau$$

Table 5.1: Parameters of Skyrme interaction SIII [114]

| $t_0$ (MeV · fm$^3$) | $t_1$ (MeV · fm$^5$) | $t_2$ (MeV · fm$^5$) | $t_3$ (MeV · fm$^6$) | $t_4$ (MeV · fm$^5$) | $x_0$ |
|---|---|---|---|---|---|
| -1128.75 | 395.0 | -95.0 | 14000.0 | 120.0 | 0.45 |

$$
\begin{aligned}
&+\frac{1}{4}(t_1+t_2)\mathcal{K}+\frac{1}{8}(t_2-t_1)\mathcal{K}_\tau+\frac{t_3}{12}\left(1+\frac{x_3}{2}\right)(\alpha+2)\rho^{\alpha+1} \\
&-\frac{t_3}{12}\left(\frac{1}{2}+x_3\right)\left(\alpha\rho^{\alpha-1}\sum_\tau\rho_\tau^2+2\rho^\alpha\rho_\tau\right)-\frac{t_4}{2}(\vec{\nabla}\cdot\vec{J}+\vec{\nabla}\cdot\vec{J}_\tau) \\
&+\delta_{\tau,-1}e^2\left[\int d^3r'\frac{\rho_\tau(\vec{r'})}{|\vec{r}-\vec{r'}|}-\left(\frac{3}{\pi}\right)^{1/3}\{\rho_\tau(\vec{r})\}^{1/3}\right].
\end{aligned}
\tag{5.21}
$$

In this work, the Skyrme interaction SIII [114] is employed (see Table 5.1). The Skyrme-HF calculations are performed by discretizing the energy functional on a three-dimensional Cartesian spline collocation lattice, which provides a highly accurate alternative to the finite-difference method [113]. The structure of the resulting lattice representation is suited for vector and parallel supercomputers, and the method allows for highly modular programming where the order of the splines can be defined as an input parameter. Equations of motion are obtained via the variation of the lattice representations of the constants of motion, such as the total energy. It is worth noting that no self-consistent symmetry has been imposed in the calculations. The details of the spline collocation method have been published in Ref. [115]. In addition, we use the simple scaling of the nuclear mass to approximately correct for the center-of-mass motion. The calculations were performed in the cube of the size (20 fm)$^3$. In all the cases considered, the resulting HF minima turned out to correspond to reflection-symmetric shapes with three symmetry planes, i.e., $\langle x\rangle = \langle y\rangle = \langle z\rangle = 0$ and $\langle xy\rangle = \langle xz\rangle = \langle yz\rangle = 0$.

## 5.2 Relativistic Mean-Field Theory

In the RMF calculations, the model of Ref. [116] consisting of baryon (proton and neutron) and $\sigma$-, $\omega$-, and $\rho$-meson fields is used. The Lagrangian density for the present model [117] is given by

$$\begin{aligned}
\mathcal{L} &= \bar{\psi}(i\gamma^\mu\partial_\mu - m)\psi + \frac{1}{2}\partial_\mu\sigma\partial^\mu\sigma - U(\sigma) - \frac{1}{4}\Omega_{\mu\nu}\Omega^{\mu\nu} + \frac{1}{2}m_\omega^2\omega_\mu\omega^\mu \\
&\quad -\frac{1}{4}R^a_{\mu\nu}R^{\mu\nu a} + \frac{1}{2}m_\rho^2\rho^a_\mu\rho^{\mu a} - \frac{1}{4}F_{\mu\nu}F^{\mu\nu} - g_\sigma\bar{\psi}\sigma\psi - g_\omega\bar{\psi}\gamma^\mu\omega_\mu\psi \\
&\quad -g_\rho\bar{\psi}\gamma^\mu\rho^a_\mu\tau^a\psi - e\bar{\psi}\gamma^\mu\frac{(1-\tau^3)}{2}A_\mu\psi
\end{aligned} \tag{5.22}$$

where

$$\Omega_{\mu\nu} = \partial_\mu\omega_\nu - \partial_\nu\omega_\mu, \quad R^a_{\mu\nu} = \partial_\mu\rho^a_\nu - \partial_\nu\rho^a_\mu - g_\rho\epsilon^{abc}\rho^b_\mu\rho^c_\nu, \quad F_{\mu\nu} = \partial_\mu A_\nu - \partial_\nu A_\mu. \tag{5.23}$$

Here, the usual Einstein summation convention is used. The indices $a$, $b$, $c$ denote the isotopic components, $\tau^3$ as the third component of isospin vector, and $A$ as the electromagnetic interaction. Table 5.2 shows the descriptions for the quantities appearing in Eq. (5.22). In addition, the scaler meson $\sigma$ is assumed to move in a non-linear potential [117]

$$U(\sigma) = \frac{1}{2}m_\sigma^2\sigma^2 + \frac{1}{3}g_2\sigma^3 + \frac{1}{4}g_3\sigma^4. \tag{5.24}$$

The substitution of the Lagrangian given in Eq. (5.22) into the Euler-Lagrange equation for the generalized coordinates $\{q_i\}$

$$\frac{\partial}{\partial x^\mu}\left[\frac{\partial\mathcal{L}}{\partial(\partial q_i/\partial x^\mu)}\right] - \frac{\partial\mathcal{L}}{\partial q_i} = 0 \tag{5.25}$$

**Table 5.2**: Definition of fields in the RMF approach

| Particles | Description | Mass | Field | Coupling |
|---|---|---|---|---|
| $p, n$ | Baryon | $m$ | $\psi$ | |
| $\sigma$ | Neutral scalar meson | $m_\sigma$ | $\sigma$ | $g_\sigma$ |
| $\omega$ | Neutral vector meson | $m_\omega$ | $\omega_\mu$ | $g_\omega$ |
| $\rho$ | Charged vector meson | $m_\rho$ | $\rho_\mu^a$ | $g_\rho$ |

yields the following equations of motion:

$$(\partial_\mu \partial^\mu + m_\sigma^2)\sigma = -g_\sigma \bar{\psi}\psi - g_2\sigma^2 - g_3\sigma^3, \tag{5.26}$$

$$\partial_\mu \Omega^{\mu\nu} + m_\omega^2 \omega^\nu = g_\omega \bar{\psi}\gamma^\nu \psi, \tag{5.27}$$

$$\partial_\mu R^{\mu\nu a} + m_\rho^2 \rho^{\nu a} = g_\rho \bar{\psi}\gamma^\nu \tau^a \psi, \tag{5.28}$$

$$\partial_\mu F^{\mu\nu} = e\bar{\psi}\gamma^\nu \frac{(1-\tau^3)}{2}\psi, \tag{5.29}$$

$$\left[i\gamma^\mu \partial_\mu - M - g_\sigma \sigma - g_\omega \gamma^\mu \omega_\mu - g_\rho \gamma^\mu \rho_\mu^a \tau^a - e\gamma^\nu \frac{(1-\tau^3)}{2} A_\mu\right]\psi = 0. \tag{5.30}$$

Equations (5.26)-(5.28) are the Klein-Gordon equations for meson fields, whereas the last equation (5.30) is the Dirac equation with scalar and vector fields.

In the mean-field approximation, the meson and photon field operators are replaced with static fields. The Klein-Gordon equations for meson fields [Eqs. (5.26)-(5.30)] now become

$$(-\nabla^2 + m_\sigma^2)\sigma(\vec{r}) = -g_\sigma \rho_s(\vec{r}) - g_2\sigma^2(\vec{r}) - g_3\sigma^3(\vec{r}), \tag{5.31}$$

$$(-\nabla^2 + m_\omega^2)\omega_0(\vec{r}) = g_\omega \rho_v(\vec{r}), \tag{5.32}$$

$$(-\nabla^2 + m_\rho^2)\rho_0(\vec{r}) = g_\rho \rho_3(\vec{r}), \tag{5.33}$$

$$-\nabla^2 A_0(\vec{r}) = e\rho_p(\vec{r}), \tag{5.34}$$

where

$$\rho_s(\vec{r}) = \sum_{i=1}^{A} \bar{\psi}_i(\vec{r})\psi_i(\vec{r}), \tag{5.35}$$

$$\rho_v(\vec{r}) = \sum_{i=1}^{A} \psi_i^+(\vec{r})\psi_i(\vec{r}), \tag{5.36}$$

$$\rho_3(\vec{r}) = \sum_{i=1}^{A} \psi_i^+(\vec{r})\tau^3\psi_i(\vec{r}), \tag{5.37}$$

$$\rho_p(\vec{r}) = \sum_{i=1}^{A} \psi_i^+(\vec{r})\frac{(1-\tau^3)}{2}\psi_i(\vec{r}). \tag{5.38}$$

Similarly, the corresponding static Dirac equation can be written as:

$$\left[-i\vec{\alpha}\cdot\vec{\nabla} + \beta m^*(\vec{r}) + V(\vec{r})\right]\psi_i(\vec{r}) = \epsilon_i\psi_i(\vec{r}), \tag{5.39}$$

where

$$m^*(\vec{r}) = m + g_\sigma\sigma(\vec{r}) \tag{5.40}$$

and

$$V(\vec{r}) = g_\omega\omega_0(\vec{r}) + g_\rho\tau^3\rho_0(\vec{r}) + e\frac{(1-\tau^3)}{2}A_0(\vec{r}). \tag{5.41}$$

(A comprehensive discussion on the RMF theory can be found in Ref. [116].)

The meson masses $m_\sigma$, $m_\omega$, $m_\rho$, the coupling constants $g_\sigma$, $g_\omega$, $g_\rho$, and the constants $g_2$, $g_3$ appearing in the non-linear potential $U(\sigma)$ are to be obtained by fitting them to the experimental data and finite nuclear properties. In the present work, we have employed the NL-SH set of the Lagrangian density parameters [117] (see Table 5.3), as this set has been claimed to be particularly successful in describing properties of very neutron-rich systems. The resulting Dirac equation for baryons [Eq. (5.39)] and the Klein-Gordon equations for mesons [Eqs. (5.31)-(5.34)] were solved by expanding the small and large components of the Dirac spinor and the

Table 5.3: Parameters of the NL-SH set

| M (MeV) | $m_\sigma$ (MeV) | $m_\omega$ (MeV) | $m_\rho$ (MeV) | $g_\sigma$ | $g_\omega$ | $g_\rho$ | $g_2$ | $g_3$ |
|---|---|---|---|---|---|---|---|---|
| 939.0 | 526.06 | 783.0 | 763.0 | 10.44 | 12.95 | 4.38 | −6.91 | −15.834 |

meson fields in the basis consisting of 12 harmonic oscillator shells. The expansion method in the harmonic oscillator basis does not allow for a precise description of the wave-function asymptotics in very neutron-rich nuclei, but in practice does not influence calculated energies and values of two-neutron separation energy $S_{2n}$.

## 5.3 Deformations of Neutron-Rich Sulfur Isotopes

To shed some light on the physics of exotic neutron-rich nuclei with N≈28, we performed self-consistent calculations for the sulfur isotopes. The predicted separation energies have been compared to the results of recent large scale mass calculations using the finite-range droplet model (FRDM) [72], the extended Thomas-Fermi with Strutinski-integral model (ETFSI) [73], and the available experimental data (the predicted charge radii are also compared to the experimental data). Particular attention has been paid to three topics: (i) the onset of deformation around the $N$=28 magic gap, (ii) stability of the heaviest isotopes, and (iii) the isovector shape deformation effects.

In this study the 'constant-gap' approximation was used with a strongly reduced pairing, $\Delta_n=\Delta_p$=75 keV and 200 keV in the RMF and HF models, respectively. The RMF calculations were also performed with $\Delta_n=\Delta_p$=500 keV. The results obtained were very similar to those with $\Delta_n$=$\Delta_p$=75 keV. In both types of calculations (HF and RMF), the number of iterations was chosen individually for each nucleus, so as to ensure convergence within 5 keV in both total and single particle energies.

In most cases, the ground-state minima of the sulfur isotopes can be associated with deformed intrinsic states. In order to compare various variants of calculations, the standard quadrupole deformation parameters $\beta_2$ and $\gamma$ were extracted. First, the two quadrupole moments, $q_{20} = \sqrt{16\pi/5}\langle r^2 Y_{20}\rangle$ and $q_{22} = \sqrt{8\pi/15}\langle r^2\,(Y_{22} + Y_{2-2})\rangle$ were expressed in terms of the polar coordinates $Q_\circ$ and $\gamma$ [118, 119]

$$q_{20} = Q_\circ \cos\gamma, \qquad q_{22} = \frac{1}{\sqrt{3}} Q_\circ \sin\gamma. \tag{5.42}$$

Using Eq. (5.42), the $\gamma$–value can be determined. The quadrupole moment of proton distribution, $Q_\circ^p$, can be written in terms of $\beta_2^p$ by means of relation

$$Q_\circ^p = \sqrt{\frac{5}{\pi}} Z\langle r_p^2\rangle\beta_2^p. \tag{5.43}$$

Similarly, one can extract quadrupole deformations of neutron ($\beta_2^n$) and mass ($\beta_2^A$) distributions. Since in most cases the equilibrium shapes predicted by the HF model are axial, the standard convention was adapted [i.e., $\beta_2$>0 (prolate) for $\gamma$~0° and $\beta_2$<0 (oblate) for $\gamma$~60°].

Figure 5.1(a) displays the representative single-particle neutron levels as functions of quadrupole deformation $\beta_2$. The Nilsson diagram was obtained using a deformed Woods-Saxon model [120] with a Chepurnov set of parameters [121]; the resulting single-particle energies are close to those from the HF+SIII model.

The two-neutron separation energies for the sulfur isotopes, $S_{2n}$, are displayed in Fig. 5.1(b) as a function of neutron number. Our HF and RMF results are

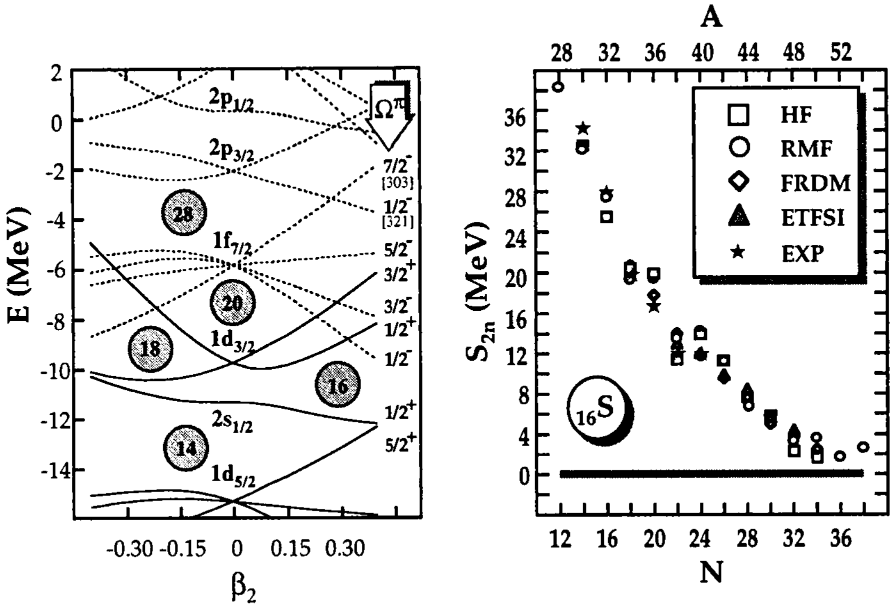


(a) (b)

**Figure 5.1**: (a) Wood-Saxon single-particle neutron levels as functions of $\beta_2$ for nuclei around $^{44}$S. The orbitals are labeled by means of $\Omega$ and $\pi$ ($\pi = +$, solid line; $\pi = -$, dashed line) quantum numbers. (b) Two-neutron separation energies of the even-even sulfur isotopes calculated with the HF and RMF models. They are compared with the results of the FRDM [72] and ETFSI [73] models, and experimental data.

compared with the predictions of the FRDM and ETFSI models, and experimental data. In general, the agreement between the models themselves and between theory and experiment is good. In the HF model, the nucleus $^{52}$S ($N$=36) is two-neutron-unstable. The RMF calculations yield more neutron binding; the isotopes $^{52,54}$S are predicted to lie inside the two-neutron drip line. The systematic model agreement for $S_{2n}$ should not imply that the intrinsic structures of neutron-rich sulfur isotopes are also similar in all models presented in Fig. 5.1(b). As discussed below, this is not the case.

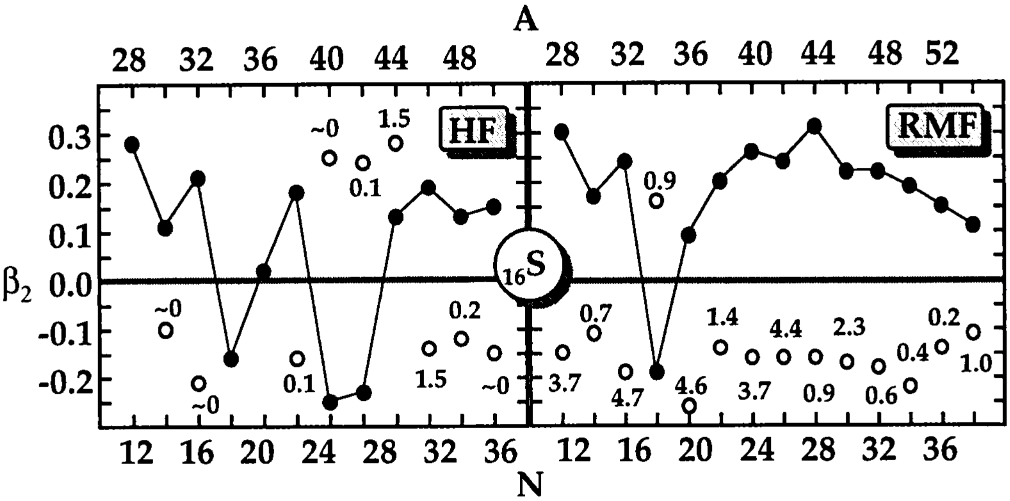


**Figure 5.2**: Quadrupole mass deformations $\beta_2^A$ of the even-even sulfur isotopes calculated with the HF (left) and RMF (right) models. The dots connected by a solid line correspond to ground-state deformations. The empty circles indicate excited configurations with excitation energies given in MeV.

The calculated mass quadrupole deformations of even-even sulfur isotopes are shown in Fig. 5.2 as a function of neutron number. (Usually, calculations yield more than one energy minimum. In such situations, deformations and excitation energies of excited states are also displayed.) The deformation pattern for even-even isotopes $^{28-38}$S is fairly similar in the HF and RMF models: prolate ground states in $^{28-32,38}$S, oblate minimum in $^{34}$S, and spherical shape in the magic $N$=20 nucleus $^{36}$S[‡]. However, the differences show up for the heavier isotopes. The nuclei $^{40,42}$S are predicted by the RMF model to have prolate ground states with $\beta_2$~0.25; the oblate minima with $\beta_2$~-0.16 lie about 4 MeV higher in energy. In the HF calculations, prolate ($\beta_2$~0.25) and oblate ($\beta_2$~–0.24) configurations are practically

[‡]It is to be noted here that RMF predicts a slightly deformed shape for $^{36}$S while HF yields spherical equilibrium. This can be attributed to different ordering of the $2s_{1/2}$ and $1d_{3/2}$ shells in these two models. In the HF+SIII $1d_{3/2}$ shell lies above $2s_{1/2}$ shell, thus producing the spherical subshell at $Z$=16. Due to very weak pairing and spherical degeneracy at $Z$=16 in the RMF calculations, small deformation is predicted. However, if a stronger proton pairing gap is assumed, $\Delta_p$=1 MeV, the equilibrium shape becomes spherical.

degenerate. The FRDM and ETFSI models give prolate-deformed ground states with ($\beta_2$~0.25), in agreement with our findings. There is no consensus regarding the equilibrium shape of the $N$=28 nucleus $^{44}$S. According to RMF calculations, $^{44}$S has a well-deformed prolate ground state with $\beta_2$=0.31. The oblate minimum with $\beta_2$=0.16 appears to lie 0.8 MeV higher. The spherical saddle point lies even higher at $E^*$=2.8 MeV. On the other hand, according to the HF model, $^{44}$S is a gamma-soft system with a small quadrupole deformation $\beta_2$~0.13. The very shallow, well-deformed prolate minimum ($\beta_2$=0.28) analogous to the RMF ground state lies at $E^*$~1.5 MeV. The FRDM and ETFSI models give spherical and oblate ($\beta_2$=−0.26) ground states, respectively. Experimentally, moderate deformations around $N$=28 have recently been observed [71].

The heavier sulfur isotopes with $N$ >28 are consistently calculated to be prolate-deformed in the HF, RMF, and FRDM models. The oblate minima are higher in energy, but with increasing neutron number, the prolate-oblate energy difference is reduced. The RMF approach yields systematically larger quadrupole deformations compared to HF. For instance, according to the RMF predictions, $^{48}$S is a well-deformed system with $\beta_2$=0.22. According to the HF model, it is a transitional nucleus with $\beta_2$=0.13, $\gamma$=10°. Interestingly, the ETFSI approach favors a strongly deformed oblate configuration with $\beta_2$=−0.25.

The neutron and proton single-particle levels in the ground-state of $^{44}$S obtained in HF and RMF models are displayed in Fig. 5.3. The deformed shape in $^{44}$S results from a subtle interplay between the deformed gaps at $Z$=16 and $N$=28, and the spherical $N$=28 gap. In the RMF model, the spherical $N$=28 gap is completely

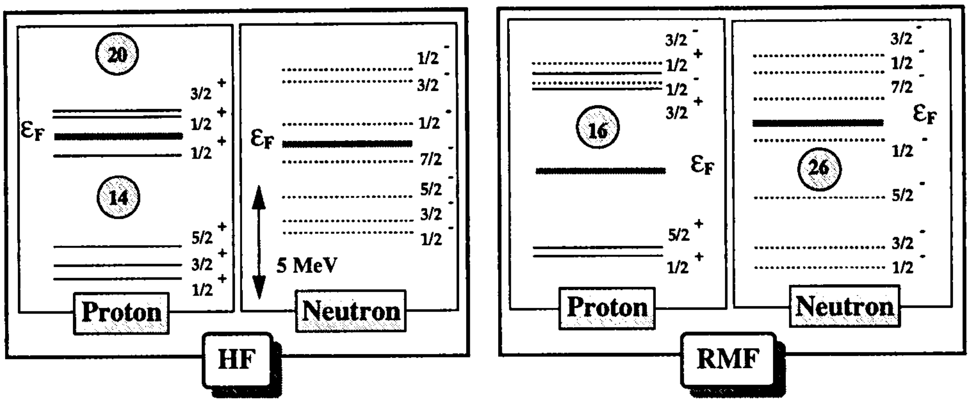


**Figure 5.3**: The shell structure of $^{44}$S as predicted by the HF (left) and RMF(right) models.

broken; the neutron intruder orbital [321]1/2, originating from the $2p_{3/2,1/2}, 1f_{5/2}$ shells above the $N$=28 gap is occupied. In the HF calculations the energy distance between the deformed [321]1/2 and [303]7/2 levels is only 1.6 MeV.

The predicted rms neutron and charge radii of even-even sulfur isotopes are illustrated in Fig. 5.4. The results of HF and RMF models are fairly similar. There appears a systematic shift of ~0.08 fm between the HF and RMF results for the rms charge radii; the experimental data for $^{32,34,36}$S lie in between. As expected, due to skin effect, rms radii increase when approaching particle drip lines. (Since the pairing correlations are practically neglected, the undesired 'particle gas' effect is not present.)

Figure 5.5(a) illustrates the dependence of the $Q^n_\circ/Q^p_\circ$ ratio on the $N/Z$ ratio. Up to neutron number $N$=26, the HF and RMF results are very similar. The dips in $Q^n_\circ/Q^p_\circ$ in the HF calculations appear at shell and subshell closures (i.e., at $N$=14, 20, 28, and 32). At these particle numbers the neutron distribution has a tendency to be more spherical. The lack of shell fluctuations in $Q^n_\circ/Q^p_\circ$ in the RMF model at

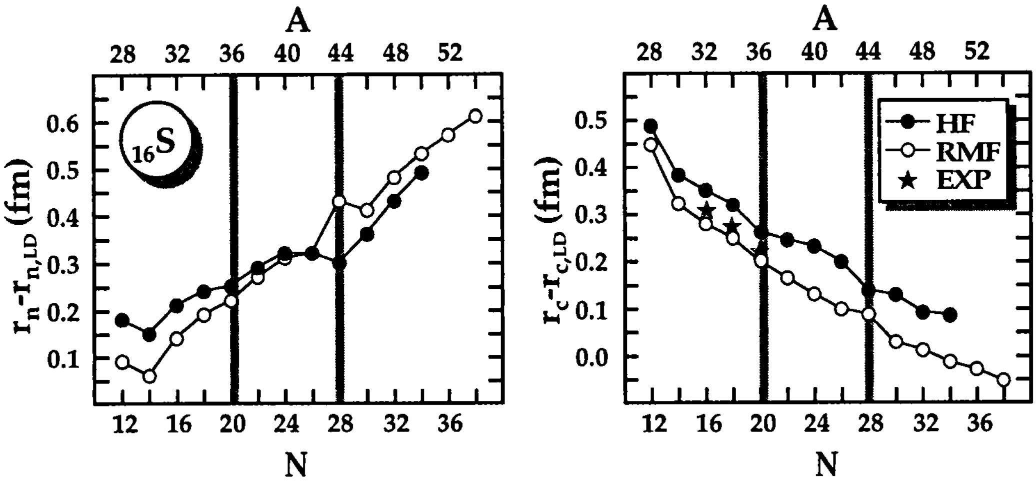


(a) (b)

**Figure 5.4**: Root-mean-square radii of the (a) neutron distribution and (b) charge distribution of the even-even sulfur isotopes calculated with the HF and RMF models. The radii are shown relative to the average (liquid-drop) value of $\sqrt{3/5}R_\circ$, $R_\circ = 1.2\mathrm{A}^{1/3}$ fm. The experimental data for $^{32,34,36}$S are taken from Ref. [122].

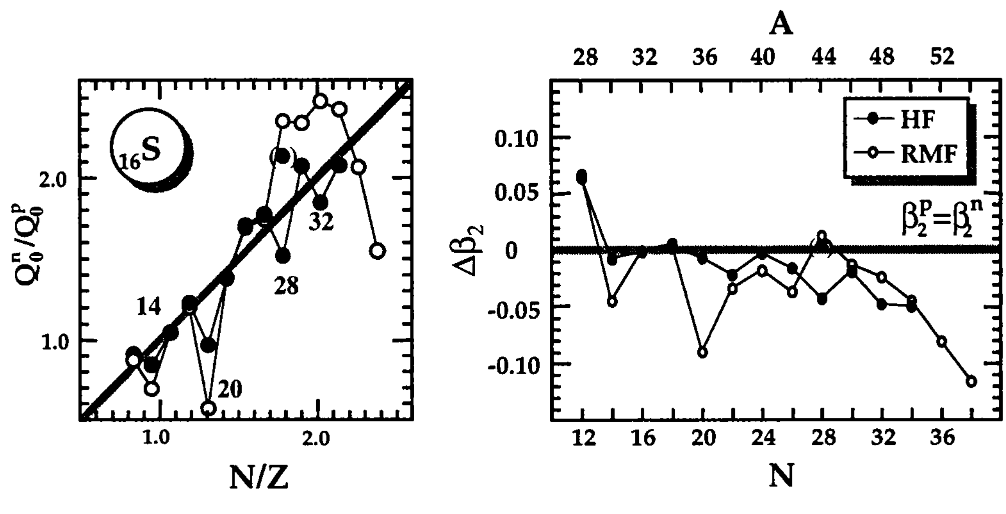


(a) (b)

**Figure 5.5**: (a) Ratio of neutron and proton quadrupole moments versus N/Z. The large-deformation excited state in $^{44}$S calculated in the HF model is indicated by means of an '(•)' symbol. (b) Difference $\Delta\beta_2 \equiv \beta_2^n - \beta_2^p$ for the even-even sulfur isotopes calculated with the HF and RMF models as a function of neutron number.

$N$ >26 is consistent with the calculated large prolate deformations. Interestingly, above $N$=28, $\Delta\beta_2$(RMF) decreases steadily with neutron number, while the $Q_\circ^n/Q_\circ^p$ (RMF) ratio intersects the $N/Z$ line (rigid geometric limit) only at $N$>34.

The difference between neutron and proton deformations, $\Delta\beta_2 \equiv \beta_2^n - \beta_2^p$, is illustrated in Fig. 5.5(b). It is seen that when approaching the neutron drip line, the values of $\beta_2^n$ are systematically smaller than those of the proton distribution. An opposite effect is seen around the proton drip-line. The largest difference, $|\Delta\beta_2|\sim 0.10$, is obtained in the RMF model for $^{54}$S. (As discussed above, the deviation for $^{36}$S disappears if the stronger proton pairing gap is assumed.) The behavior of $\Delta\beta_2$ can be partly attributed to the isotonic behavior of rms radii in Fig. 5.4 [see the definition (5.43) of $\beta_2$]. Indeed, the value of $Q_\circ$ depends both on the angular anisotropy *and* the radial dependence of the nucleonic density. In the drip-line nuclei, due to spatially extended wave functions, the 'radial' contribution to $Q_\circ$ might be as important as the 'angular' part. The significance of the radial contribution to the quadrupole moment was already discussed in the previous chapters. Consider, e.g., large decrease in $\Delta\beta_2$ observed for $N$=34-38 in the RMF calculations in Fig. 5.5(b). According to Fig. 5.1(a), the last two neutrons occupy the Nilsson level originating from the $p_{1/2}$ orbital for $N$=34 and $f_{5/2}$ orbital for $N$=36, 38. These deformed orbitals ($\Lambda\leq 1$) were, in fact, classified as the *halo* orbitals in the previous discussions. It was shown that for such low-$\Lambda$ orbitals the deformation decoupling of the neutron excess takes place.

A similar effect can also be seen for the proton-rich side in Fig. 5.5(b) (see also Fig. 5.4). Namely, the dramatic increase in $\Delta\beta_2$ at $N$=12 can be understood in terms of the decoupling of the two weakly bound protons in the $s_{1/2}$ orbital from the core. Although in Chapters 3 and 4, the loosely bound proton systems were not discussed, the low-$\Lambda$ proton orbitals should also give rise to the large spatial dimension of a nuclear system [19]. It is interesting to note that the recent theoretical study [123] by Brown and Hansen suggests a possible proton-halo structure in $^{27}S$. In this context, the present study is consistent with the proton-halo scenario for $^{27}S$.

# Chapter 6

# Conclusions

In this study, deformation properties of drip-line nuclei were investigated *both* qualitatively and quantitatively. In particular, two aspects of weakly bound nuclei were discussed. Firstly, we addressed the notion of shape deformations. It was shown that conventionally defined shape deformations are no longer useful when applied to loosely bound systems. Secondly, we investigated the deformation decoupling between the core and weakly bound particles in drip-line nuclei. In particular, large differences between proton and neutron quadrupole deformations were obtained for the sulfur isotopes near particle drip lines.

## 6.1 Remarks on Deformed Halos

Asymptotic properties of weakly bound systems were investigated in Chapters 3 and 4. It was shown that, near particle threshold, the matter deformations of a halo system can be approximated by the deformations of weakly bound orbitals, *regardless* of the core deformation. Consequently, in the limit of a very weak binding, the geometric interpretation of shape deformation is lost.

Consider, e.g., a deformed core with deformation $\delta$=0.2 and a weakly-bound halo neutron in a negative-parity orbital. According to the discussion in Chapter 3, the total quadrupole moment of the system diverges at the limit of vanishing binding (i.e., $\langle r^2 Y_{20}\rangle$ can take *any* value). On the other hand, depending on the geometry of the valence orbital, the total quadrupole deformation of the (core+valence) system is consistent with superdeformed shape ($\pi = -$, $\Lambda = 0$ halo) or oblate shape ($\pi = -$, $\Lambda = 1$ halo). For a positive-parity halo the quadrupole moment is finite, but $\beta_2$ approaches zero. In the language of the self-consistent mean-field theory, this result reflects the extreme softness of the system to the quadrupole distortion. Shape deformation is an extremely powerful concept provided that the nuclear surface can be properly defined. However, for very diffused and spatially extended systems, the geometric interpretation of multipole moments and deformations is no longer useful.

Our analysis of radial form factors demonstrates that in the limit of very small binding energy, a positive-parity deformed halo orbital is completely dominated by an $s$-wave component even at high deformations. For negative-parity deformed halo orbitals, those are the $p$-waves that determine the asymptotics. This result is consistent with the analysis of Ref. [100] (see Table 2 in Ref. [100]) and independent of the geometry of the mean-field, provided it vanishes at large distances.

The presence of the spatially extended neutron halo gives rise to the presence of low-energy isovector modes in neutron-rich nuclei. The deformation decoupling of the halo implies that the nuclei close to the neutron drip line are excellent candidates for isovector quadrupole deformations, with different quadrupole deformations for protons and neutrons. [Experimentally, the decoupling (in terms of both density distributions and quadrupole moments) between the core and halo neutrons [39] has been observed for $^{11}$Li.]

An example of the strong isovector shape effect has been predicted in the self-consistent calculations [82, 110] for the neutron-rich sulfur isotopes discussed in Chapter 5. When approaching the neutron drip line, the calculated values of $\beta_2$ for neutrons are systematically smaller than those of the proton distribution. In the drip-line nuclei, due to spatially extended wave functions, the 'radial' contribution to the quadrupole moment might be as important as the 'angular' part.

Finally, it is interesting to note that the anisotropic (non-spherical) halo systems have been investigated in molecular physics. A direct molecular analogy of a quadrupole-deformed halo nucleus is the electron weakly bound by the quadrupole moment of the neutral symmetric molecule such as $CS_2$ [31].

## 6.2 Remarks on Neutron-Rich Nuclei far from The Valley of Stability

We investigated ground state properties of the sulfur isotopes in Chapter 5 within self-consistent non-relativistic and relativistic mean-field approaches. The main motivation was to identify the effects of shape coexistence around $^{44}_{16}S_{28}$ and the changes in intrinsic shape deformations of the near-drip-line sulfur isotopes.

The calculations presented in Chapter 5 suggest strong deformation effects in the region around $^{44}$S due to the $1f_{7/2}\rightarrow fp$ core breaking. According to the RMF+NL-SH model, the $N$=28 nucleus $^{44}$S is well deformed in its ground state. On the other hand, the HF+SIII model predicts smaller deformations in this region and $^{44}$S is calculated to be a soft transitional system. Experimentally, following our predictions, moderate deformations around $N$=28 have recently been determined by the group at Michigan State University [71].

Large differences between neutron and proton quadrupole deformations are obtained in the RMF approach in deformed sulfur nuclei far from stability. These differences in the neutron-rich and neutron-deficient sulfur isotopes can be understood in terms of the spatially extended (low-$\Lambda$) valence orbitals. The important role of weakly bound low-$\Lambda$ orbitals on the quadrupole deformation was already discussed in Chapters 3 and 4. Since in stable nuclei charge (i.e., proton) deformations are very close to matter deformations [108], the isovector deformations, predicted in this analysis, are characteristic properties of drip-line nuclei. Such differences might have interesting consequences for the quadrupole isovector modes in drip-line systems.

# Bibliography

# Bibliography


[1] I. Peterson, *The Mathematical Tourist* (W.H.Freeman and Company, New York, 1988).

[2] F.J. Almgren and J.E. Taylor, Sci. Am. **Vol.235**, 82 (1976).

[3] J.E. Taylor and J.W. Cahn, Acta Metal. **Vol.34**, 1 (1986).

[4] http://www.exploratorium.edu/ronh/bubbles/bubbles.html and http://www.leonet.it/culture/nexus96, (1996).

[5] R.H. Silliman, ISIS **Vol.54**, 1 (1963).

[6] J.J. Thomson, *A Treatise on The Motion of Vortex Rings* (Macmillan and Co., London, 1883).

[7] R.L. Ricca and M.A. Berger, Phys. Tod. **Vol. 49**, 28 (1996).

[8] P.G. Tait, *Scientific Papers by P.G.Tait* (Cambridge: at The University Press, Cambridge, 1898).

[9] F. Lund and T. Regge, Phys. Rev. **D14**, 1524 (1976).

[10] L.H. Kauffman, *Knots and Physics* (World Scientific, Singapore, 1991).

[11] http://www.arc.losrios.cc.ca.us/math-eng dt/math, (1996).

[12] E.J. Aiton, *The Vortex Theory of Planetary Motions* (American Elsevier, London, Macdonald; New York, 1972).

[13] A. Chapman, *Dividing The Circle* (Ellis Horwood Limited, Oxford, UK, 1990).

[14] A. Dressler, Sci. Am. **Vol.257**, 46 (1987).

[15] http://www.damtp.cam.ac.uk/user/gr/public, (1996).

[16] R. Monastersky, Sci. News **Vol.132**, 388 (1987).

[17] W. Nazarewicz, Acta Phys. Pol. B **Vol.27**, 21 (1996).

[18] A.C. Mueller and B.M. Sherrill, Annu. Rev. Nucl. Part. Sci. **43**, 529 (1993).

[19] K. Riisager, A.S. Jensen, and P. Møller, Nucl. Phys. **A548**, 393 (1992).

[20] N. Fukunishi, T. Otsuka, and I. Tanihata, Phys. Rev. **C48**, 1648 (1993).

[21] I. Tanihata, H. Hamagaki, O. Hashimoto, Y. Shida, N. Yoshikawa, K. Sugimoto, O. Yamakawa, T. Kobayashi, and N. Takahashi, Phys. Rev. Lett. **55**, 2676 (1985).

[22] http://fyaxp2.fy.chalmers.se:8000/htbin/dcl_isotopes.com, (1996).

[23] O. Solin, D. Guilemaud-Mueller, A.C. Mueller, V. Borrel, S. Doga, F. Pougheon, K.-L. Kratz, H. Gabelmann, B. Pfeiffer, A. Wöhr, W. Ziegert, Yu. E. Penionzhkevich, S.M. Lukyanov, V.S. Salamatin, R. Anne, C. Borcea, L.K. Fifield, M. Lewitowicz, M.G. Saint-Laurent, D. Bazin, C. Détraz, F.-K. Thielemann, and W. Hillebrandt, Phys. Rev. **C47**, 2941 (1993).

[24] R. Schneider, J. Friese, J. Reinhold, K. Zeitelhack, T. Faestermann, R. Gernhäuser, H. Gilg, F. Heine, J. Homolka, P. Kienle, H.J. Körner, H. Geissel, G. Münzenberg, and K. Sümmerer, Z. Phys. **A348**, 241 (1994).

[25] W. Böhmer *et al.*, Verhandl.GDP **VI29**, 1816 (1994).

[26] K. Langanke and C.A. Barnes, Adv. Nuc. Phys. **22**, 173 (1996).

[27] G.M. Fuller, R.N. Boyd, and J.D. Kalen, Astrophys.J. **371**, L11 (1991).

[28] R.N. Boyd, D. Hirata, N. Inabe, T. Kubo, T. Nakagawa, T. Suzuki, I. Tanihata, M. Yonokura, X.X. Bai, K. Kimura, S. Kubono, S. Shimoura, and H.S. Xu, Nucl. Phys. **A538**, 523c (1992).

[29] C. Alcock, R.A. Allsman, T.S. Axelrod, D.P. Bennett, K.H. Cook, K.C. Freeman, K. Griest, J.A. Guern, M.J. Lehner, S.L. Marshall, H.-S. Park, S. Perlmutter, B.A. Peterson, M.R. Pratt, P.J. Quinn, A.W. Rodgers, C.W. Stubbs, and W. Sutherland, Phys. Rev. Lett. **74**, 2867 (1995).

[30] Various informations can be found by searching for a word 'Halos' on internet, (1996).

[31] R.N. Compton, F.B. Dunning, and P. Nordlander, Chem. Phys. Lett. **253**, 8 (1996).

[32] S. Huber, Phys. Rev. **A31**, 3981 (1985).

[33] B.D. Esry, C.D. Lin, and C.H. Greene, Phys. Rev. **A54**, 394 (1996).

[34] J. Macek, Z. Phys. **D3**, 31 (1986).

[35] Z. Zhen and J. Macek, Phys. Rev. **A38**, 1193 (1988).

[36] G. Borm and F. Wysotzki, Nucl. Phys. **B15**, 628 (1970).

[37] D. Bazin, B.A. Brown, J. Brown, M. Fauerbach, M. Hellström, S.E. Hirzebruch, J.H. Kelley, R.A. Kryger, D.J. Morrissey, R. Pfaff, C.F. Powell, B.M. Sherrill, and M. Thoennessen, Phys. Rev. Lett. **74**, 3569 (1995).

[38] M.V. Zhukov, B.V. Danilin, D.V. Fedorov, J.M. Bang, I.J. Thompson, and J.S. Vaagen, Phys. Rev. **231**, 151 (1993).

[39] I. Tanihata, J. Phys. **G22**, 157 (1996).

[40] P.G. Hansen, A.S. Jensen, and B. Jonson, Annu. Rev. Nucl. Part. Sci. **45**, 591 (1995).

[41] T. Minamisono, T. Ohtsubo, I. Minami, S. Fukuda, A. Kitagawa, M. Fukuda, K. Matsuta, Y. Nojiri, S. Takeda, H. Sagawa, and H. Kitagawa, Phys. Rev. Lett. **69**, 2058 (1992).

[42] M.V. Zhukov and B. Jonson, Nucl. Phys. **A589**, 1 (1995).

[43] H. Nakada and T. Otsuka, Phys. Rev. **C49**, 886 (1994).

[44] A. Muta and T. Otsuka, preprint (1995).

[45] D.V. Fedorov, A.S. Jensen, and K. Riisager, Phys. Rev. **C49**, 201 (1994).

[46] N.K. Timofeyuk, P. Descouvemont, and D. Baye, Nucl. Phys. **A600**, 1 (1996).

[47] T. Kobayashi, O. Yamakawa, K. Omata, K. Sugimoto, T. Shimoda, N. Takahashi, and I. Tanihata, Phys. Rev. Lett. **60**, 2599 (1988).

[48] J.H. Kelley, Sam M. Austin, R.A. Kryger, D.J. Morrissey, N.A. Orr, B.M. Sherrill, M. Thoennessen, J.S. Winfield, J.A. Winger, and B.M. Young, Phys. Rev. Lett. **74**, 30 (1995).

[49] J. Hüfner and M.C. Nemes, Phys. Rev. **C23**, 2538 (1981).

[50] K. Riisager, M.J.G. Borge, H. Gabelmann, P.G. Hansen, L. Johannsen, B. Jonson, W. Kurcewicz, G. Nyman, A. Richter, O. Tengblad, K. Wilhelmsen, and ISOLDE collaboration, Phys. Lett. **B235**, 30 (1990).

[51] M.J.G. Borge, L. Johannsen, B. Jonson, T. Nilsson, G. Nyman, K. Riisager, O. Tengblad, K. Wilhelmsen Rolander, and ISOLDE Collaboration, Nucl. Phys. **A560**, 664 (1993).

[52] T. Suzuki and T. Otsuka, Phys. Rev. **C50**, R555 (1993).

[53] T. Kobayashi, S. Shimoura, I. Tanihata, K. Katori, K. Matsuta, T. Minamisono, K. Sugimoto, W. Müller, D.J. Olson, T.J.M. Symons, and H. Wieman, Phys. Lett. **232**, 51 (1989).

[54] Y. Suzuki and Y. Tosaka, Nucl. Phys. **517**, 599 (1990).

[55] K. Ikeda Y. Suzuki and H. Sato, Prog. Theor. Phys. **83**, 180 (1990).

[56] S.A. Fayans, Phys. Lett. **B267**, 443 (1991).

[57] H. Esbensen and G.F. Bertsch, Nucl. Phys. **A542**, 310 (1992).

[58] S. Shimoura, T. Nakamura, M. Ishihara, N. Inabe, T. Kobayashi, T. Kubo, R.H. Siemssen, I. Tanihata, and Y. Watanabe, Phys. Lett. **B348**, 29 (1995).

[59] F. Catara, C.H. Dasso, and A. Vitturi, Nucl. Phys. **A602**, 181 (1996).

[60] I. Tanihata, D. Hirata, T. Kobayashi, S. Shimoura, K. Sugimoto, and H. Toki, Phys. Lett. **B289**, 261 (1992).

[61] T. Suzuki, H. Geissel, O. Bochkarev, L. Chulkov, M. Golovkov, D. Hirata, H. Irnich, Z. Janas, H. Keller, T. Kobayashi, G. Kraus, G. Münzenberg, S. Neumaier, F. Nickel, A. Ozawa, A. Piechaczeck, E. Roeckl, W. Schwab, K. Sümmerer, K. Yoshida, and I. Tanihata, Phys. Rev. Lett. **75**, 3241 (1995).

[62] J.L. Wood, K. Heyde, W. Nazarewicz, M. Huyse, and P. van Duppen, Phys. Rep. **215**, 101 (1992).

[63] C. Détraz, D. Guillemaud, G. Huber, R. Klapish, M. Langevin, F. Naulin, C. Thibault, L.C. Carraz, and F. Touchard, Phys. Rev. **C19**, 164 (1979).

[64] X. Campi, H. Flocard, A. K. Kerman, and S. Koonin, Nucl. Phys. **A251**, 193 (1975).

[65] R. Bengtsson, P. Möller, J.R. Nix, and J. y. Zhang, Physica Scripta **29**, 402 (1984).

[66] A. Poves and J. Retamoso, Phys. Lett. **184B**, 311 (1987).

[67] E.K. Warburton, J.A. Becker, and B.A. Brown, Phys. Rev. **C41**, 1147 (1990).

[68] K. Heyde and J.L. Wood, J. Phys. **G17**, 135 (1991).

[69] M. Lewitowicz, Yu.E. Penionzhkevich, A.G. Artukh, A.M. Kalinin, V.V. Kamanin, S.M. Lukyanov, Nguyen Hoai Chau, A.C. Mueller, D. Guillemaud-

Mueller, R. Anne, D. Bazin, C. Detraz, D. Guerreau, M.G. Saint-Laurent, V. Borrel, J.C. Jacmart, F. Pougheon, A. Richard, and W.D. Schmidt-Ott, Nucl. Phys. **A496**, 477 (1989).

[70] M. Lewitowicz, Yu.E. Penionzhkevich, A.G. Artyukh, A.V. Belozerov, S.M. Lukyanov, D. Guillemaud-Mueller, Zh.K. Zhakmar, E. Kashy, A. Latimer, A.K. Mueller, F. Pougheon, A. Richard, R. Anne, P. Bricault, C. Detraz, I. Zhong, D. Bazin, and W.D. Schmidt-Ott, Proc. Ann. Conf. Nucl. Spectrosc. Struct. At. Nuclei, Leningrad p.50 (1990).

[71] H. Scheit, T. Glasmacher, B.A. Brown, J.A. Brown, P.D. Cottle, P.G. Hansen, R. Harkewicz, M. Hellström, R.W. Ibbotson, J.K. Jewell, K.W. Kemper, D.J. Morrissey, M. Steiner, P. Thirolf, and M. Thoennessen, Phys. Rev. Lett. .

[72] P. Möller, J.R. Nix, W.D. Myers, and W.J. Swiatecki, At. Data and Nucl. Data Tab. to be published .

[73] Y. Aboussir, J.M. Pearson, A.K. Dutta, and F. Tondeur, Nucl. Phys. **A549**, 155 (1992).

[74] J. Dobaczewski, T.R. Werner W. Nazarewicz, J.F. Berger, C.R. Chinn, and J. Dechargé, Phys. Rev. **C53**, 2809 (1996).

[75] J. Dobaczewski, W. Nazarewicz, and T.R. Werner, Physica Scripta **T56**, 15 (1995).

[76] W. Nazarewicz, T.R. Werner, and J. Dobaczewski, Phys. Rev. **C50**, 2860 (1994).

[77] W. Nazarewicz, J. Dobaczewski, and T.R. Werner, Physica Scripta **T56**, 9 (1995).

[78] W. Nazarewicz, J. Dobaczewski, T.R. Werner, J.A. Maruhn, P.-G. Reinhard, K. Rutz, C.R. Chinn, A.S. Umar, and M.R. Strayer, to be published .

[79] J. Dobaczewski, I. Hamamoto, W. Nazarewicz, and J.A. Sheikh, Phys. Rev. Lett. **72**, 981 (1994).

[80] J. Dobaczewski, H. Flocard, and J. Treiner, Nucl. Phys. **A422**, 103 (1984).

[81] J. Terasaki, P.-H. Heenen, H. Flocard, and P. Bonche, Nucl. Phys. **A600**, 371 (1996).

[82] T.R. Werner, J.A. Sheikh, M. Misu, W. Nazarewicz, J. Rikovska, K. Heeger, A.S. Umar, and M.R. Strayer, Nucl. Phys. **A597**, 327 (1996).

[83] F. Ajzenberg-Selove, Nucl. Phys. **A490**, 1 (1988).

[84] Zhongzhou Ren, Z.Y. Zhu, Y.H. Cai, and Gongou Xu, Nucl. Phys. **A605**, 75 (1996).

[85] M. Fukuda, T. Ichihara, N. Inabe, T. Kubo, H. Kumagai, T. Nakagawa, Y. Yano, I. Tanihata, M. Adachi, K. Asahi, M. Kouguchi, M. Ishihara, H. Sagawa, and S. Shimoura, Phys. Lett. **B268**, 339 (1991).

[86] S. Raman, C.H. Malarkey, W.T. Milner, C.W. Nestor Jr., and P.H. Stelson, At. Data and Nucl. Data Tab. **36**, 1 (1987).

[87] K. Riisager, Rev. Mod. Phys. **66**, 1105 (1994).

[88] I. Tanihata, T. Kobayashi, O. Yamakawa, S. Shimoura, K. Ekuni, K. Sugimoto, N. Takahashi, T. Shimoda, and T. Sato, Phys. Lett. **B206**, 592 (1988).

[89] M. Bouten, E. Fleracker, and M.C. Bouten, Nucl. Phys. **A307**, 413 (1978).

[90] I. Ragnarsson, S. , H.-B. Hånsson, and R.K. Sheline, Nucl. Phys. **A361**, 1 (1981).

[91] S.G. Nilsson, Dan. Mat. Fys. Medd. **29**, 1 (1955).

[92] T. Otsuka, A. Muta, M. Yokoyama, N. Fukunishi, and T. Suzuki, Nucl. Phys. **A588**, 113c (1995).

[93] I. Tanihata, D. Hirata, and H. Toki, Nucl. Phys. **A583**, 769 (1995).

[94] Y. Kanada-Enyo, H. Horiuchi, and A. Ono, Phys. Rev. **C52**, 628 (1995).

[95] X. Li and P.-H. Heenen, preprint ULB PNT/2/96 .

[96] H. Esbensen, B.A. Brown, and H. Sagawa, Phys. Rev. **C51**, 1274 (1995).

[97] N. Vinh Mau, Nucl. Phys. **A592**, 33 (1995).

[98] C.A. Bertulani, L.F. Canto, and M.S. Hussein, Phys. Lett. **B353**, 413 (1995).

[99] F.M. Nunes, I.J. Thompson, and R.C. Johnson, Nucl. Phys. **A596**, 171 (1996).

[100] D. Ridikas and J.S. Vaagen, priprint ETC* (1996).

[101] W.R. Garrett, Phys. Rev. **A3**, 961 (1971).

[102] D.V. Fedorov, A.S. Jensen, and K. Riisager, Phys. Lett. **B312**, 1 (1993).

[103] S.A. Moszkowski, Phys. Rev. **99**, 803 (1955).

[104] A.C. Merchant and W.D.M. Rae, Nucl. Phys. **A571**, 43 (1994).

[105] P.M. Morse and H. Feshbach, *Methods of Theoretical Physics* (MacGraw-Hill, New York, 1953).

[106] J.A. Stratton, P.M. Morse, L.J. Chu, J.D.C. Little, and F.J. Corbató, *Spheroidal Wave Functions* (Wiley, New York, 1956).

[107] M. Abramowitz and I. Stegun, *Handbook of Mathematical Functions* (Dover, New York, 1965).

[108] W. Nazarewicz, I. Ragnarsson (ed. by D.N. Poenaru, and W. Greiner), *Handbook of Nuclear Properties* (p.80, Clarendon Press, Oxford, 1996).

[109] U. Fano, Phys. Rev. **124**, 1866 (1961).

[110] T.R. Werner, J.A. Sheikh, W. Nazarewicz, M.R. Strayer, A.S. Umar, and M. Misu, Phys. Lett. **B333**, 303 (1994).

[111] T.H.R. Skyrme, Nucl. Phys. **9**, 615 (1959).

[112] D. Vautherin and D.M. Brink, Phys. Rev. **C5**, 626 (1972).

[113] A.S. Umar, J.-S. Wu, M.R. Strayer, and C. Bottcher, J. Comp. Phys. **93**, 426 (1991).

[114] M. Beiner, N. Van Giai H. Flocard, and P. Quentin, Nucl. Phys. **A238**, 2512 (1975).

[115] A.S. Umar, J.-S. Wu, M.R. Strayer, and C. Bottcher, Phys. Rev. **C44**, 2512 (1991).

[116] B.D. Serot and J.D. Walecka, Adv. Nucl. Phys. **A422**, 1 (1986).

[117] M.M. Sharma, M.A. Nagarajan, and P. Ring, Phys. Lett. **B312**, 377 (1993).

[118] D.L. Hill and J.A. Wheeler, Phys. Rev. **89**, 1102 (1953).

[119] A. Bohr, Mat. Fys. Medd. Dan. Vid. Selsk. **26**, No.14 (1952).

[120] S. Cwiok, J. Dudek, W. Nazarewicz, J. Skalski, and T. Werner, Comp. Phys. Comm. **46**, 379 (1987).

[121] V.A. Chepurnov, Yad. Fiz. **6**, 955 (1967).

[122] L.A. Schaller, D.A. Barandao, P. Bergem, M. Boschung, T.Q. Phan, G. Piller, A. Rüetschi, L. Schellenberg, H. Schneuwly, G. Fricke, G. Mallot, and H.G. Sieberling, Phys. Rev. **C85**, 1007 (1985).

[123] B.A. Brown and P.G. Hansen, Nucl. Phys. **B381**, 391 (1996).

# Appendices

# Appendix A

# Numerical Methods

In this appendix, some of the computational procedures used in Chapter 4 are discussed. For continuum states ($\epsilon > 0$), the approach of Ref. [104] can be used. However, for $\epsilon < 0$ different technique needs to be employed. As mentioned below, the main computational difficulty arises from evaluating higher order spheroidal wave functions. Since it is essential in the present calculation to obtain the solutions at very small binding energies, the high numerical accuracy must be achieved in the limit of *both* weak binding and large deformation.

## A.1 Matching Conditions

The wave amplitudes $A_{\nu\Lambda l}$ and $B_{\nu\Lambda l}$ in Eq. (4.18) can be found following the method outlined in Ref. [104]. The matching conditions for the internal and external wave functions (4.18) at $\xi = \xi_0$ lead to the following set of equations:

$$\sum_{l}^{\infty}{}' A_{\nu\Lambda l} R_{\Lambda l}^{(1)}(c_{\text{int}}, \xi_0) S_{\Lambda l}(c_{\text{int}}, \eta) = \sum_{l}^{\infty}{}' B_{\nu\Lambda l} R_{\Lambda l}^{(3)}(ic_{\text{ext}}, \xi_0) S_{\Lambda l}(ic_{\text{ext}}, \eta) \quad \text{(A.1)}$$

and

$$\sum_{l}^{\infty}{}' A_{\nu\Lambda l} \left( \frac{dR^{(1)}_{\Lambda l}(c_{\text{int}}, \xi)}{d\xi} \right)_{\xi_0} S_{\Lambda l}(c_{\text{int}}, \eta) = \sum_{l}^{\infty}{}' B_{\nu\Lambda l} \left( \frac{dR^{(3)}_{\Lambda l}(ic_{\text{ext}}, \xi)}{d\xi} \right)_{\xi_0} S_{\Lambda l}(ic_{\text{ext}}, \eta). \tag{A.2}$$

The matching conditions [Eqs. (A.1) and (A.2)] should hold for any value of $\eta$. To eliminate this degree of freedom, one can take advantage of the fact that the angular spheroidal functions $S_{\Lambda l}(c, \eta)$ form a complete orthogonal set in the interval $-1 \leq \eta \leq 1$. By multiplying both sides of Eqs. (A.1) and (A.2) by $S^{*}_{\Lambda l'}(ic_{\text{ext}}, \eta)$ and integrating over $\eta$, one obtains the matrix equation for $A_{\nu\Lambda l}$:

$$\sum_{l}^{\infty}{}' A_{\nu\Lambda l} M_{ll'} = 0 \text{ for all } l', \tag{A.3}$$

where

$$\begin{aligned} M_{ll'} \equiv \Bigg[ \left( \frac{dR^{(1)}_{\Lambda l}(c_{\text{int}}, \xi)}{d\xi} \right)_{\xi_0} R^{(3)}_{\Lambda l'}(ic_{\text{ext}}, \xi_0) \;&-\; \left( \frac{dR^{(3)}_{\Lambda l'}(ic_{\text{ext}}, \xi)}{d\xi} \right)_{\xi_0} R^{(1)}_{\Lambda l}(c_{\text{int}}, \xi_0) \Bigg] \\ &\times \;\; \langle S_{\Lambda l'}(ic_{\text{ext}}) | S_{\Lambda l}(c_{\text{int}}) \rangle. \end{aligned} \tag{A.4}$$

The eigenenergies $\epsilon_{\nu\Lambda\pi}$ and the corresponding amplitudes $A_{\nu\Lambda l}$ are found from the condition that $\det(M)$=0.

## A.2 Calculation of Spheroidal Wave Functions

The expansion coefficients $d^{\Lambda l}_{k}(c)$ appearing in Eqs. (4.15) and (4.17), and the separation constants $\lambda_{\Lambda l}$ can be obtained simultaneously from the three-term recursion relation formula [105]:

$$\begin{aligned} &\left[ \frac{k(k-1)}{(2k+2\Lambda-1)(2k+2\Lambda-3)} \right] d^{\Lambda l}_{k-2} + \left[ \frac{(k+2\Lambda+1)(k+2\Lambda+2)}{(2k+2\Lambda+3)(2k+2\Lambda+5)} \right] d^{\Lambda l}_{k+2} \\ &+ \left[ \frac{2(k+\Lambda)(k+\Lambda+1) - 2\Lambda^2 - 1}{(2k+2\Lambda+3)(2k+2\Lambda-1)} + \frac{(k+\Lambda)(k+\Lambda+1) - \lambda_{\Lambda l}}{c^2} \right] d^{\Lambda l}_{k} = 0. \end{aligned} \tag{A.5}$$

For numerical purposes, the above recursion formula can be modified in two ways:

### (a) Eigenvalue Problem

Following the procedure discussed in Ref. [104], Eq. (A.5) can be written in the form of the linear matrix equation for a symmetric band matrix:

$$\begin{aligned}\lambda_{\Lambda l}(c)\omega_k &= \frac{c^2}{2k+3}\sqrt{\frac{(k+\Lambda+1)(k+\Lambda+2)(k-\Lambda+1)(k-\Lambda+2)}{(2k+1)(2k+5)}}\omega_{k+2} \\ &+ \left[k(k+1)+c^2\frac{2k(k+1)-2\Lambda^2-1}{(2k+3)(2k-1)}\right]\omega_k \\ &+\frac{c^2}{2k-1}\sqrt{\frac{(k+\Lambda-1)(k+\Lambda)(k-\Lambda-1)(k-\Lambda)}{(2k-3)(2k+1)}}\omega_{k-2}, \qquad (A.6)\end{aligned}$$

where

$$\omega_k \equiv d_{k-\Lambda}/\sqrt{\frac{2k+1}{2}\frac{(k-\Lambda)!}{(k+\Lambda)!}}. \qquad (A.7)$$

Hence, the matrix equation (A.5) is now reduced to the Hermitian eigenvalue problem which is easy to solve.

### (b) Boundary Condition

Dividing Eq. (A.5) by $d_k$ and defining $R_k \equiv d_k/d_{k-2}$, Eq. (A.5) can be rewritten as a difference equation:

$$R_{k+2} = \frac{1}{\alpha_k}\left(\beta_k + \frac{\gamma_k}{R_k}\right), \qquad (A.8)$$

where

$$\begin{aligned}\alpha_k &= \frac{(k+2\Lambda+1)(k+2\Lambda+2)}{(2k+2\Lambda+3)(2k+2\Lambda+5)}, \qquad (A.9)\\ \beta_k &= \frac{2(k+\Lambda)(k+\Lambda+1)-2\Lambda^2-1}{(2k+2\Lambda+3)(2k+2\Lambda-1)} + \frac{(k+\Lambda)(k+\Lambda+1)-\lambda_{\Lambda l}}{c^2}, \qquad (A.10)\\ \gamma_k &= \frac{k(k-1)}{(2k+2\Lambda-1)(2k+2\Lambda-3)}. \qquad (A.11)\end{aligned}$$

In addition, two boundary conditions have to be met: (i) the truncation of the series at $k$=0 or 1 (i.e., the exclusion of series corresponding to $k<0$), and (ii) the ratio $R_k$ must vanish for large values of $k$ [106]. Numerical values of $R_k$ obtained from both boundary conditions match at $k = l - \Lambda$ only if the correct separation constants $\lambda_{\Lambda l}$ are obtained. Defining the ratios $d_k/d_{k-2}$ calculated recursively from both boundaries (i) and (ii) as $R_k^{(-)}(\lambda)$ and $R_k^{(+)}(\lambda)$, respectively, the correct values of $\lambda_{\Lambda l}$ can be determined iteratively until values of $R_k^{(-)}(\lambda)$ and $R_k^{(+)}(\lambda)$ coincide at $k = l - \Lambda$.

The iteration scheme can be optimized by using derivatives, $dR_k^{(-)}(\lambda)/d\lambda$ and $dR_k^{(+)}(\lambda)/d\lambda$. Suppose the initial guess for $\lambda$ is off from the correct value of $\lambda_0$ by $\Delta\lambda$. The following approximated relation for $\Delta\lambda$ can be used:

$$\Delta\lambda = \left[R_k^{(+)}(\lambda) - R_k^{(-)}(\lambda)\right] / \left[\frac{dR_k^{(+)}(\lambda)}{d\lambda} - \frac{dR_k^{(-)}(\lambda)}{d\lambda}\right]. \tag{A.12}$$

The analytic forms of $dR_k^{(\pm)}(\lambda)/d\lambda$ can be obtained by means of Eq. (A.8):

$$\frac{dR_{k+2}^{(-)}}{d\lambda} = \frac{1}{\alpha_k}\left[\frac{1}{c^2} + \frac{\gamma_k}{\left(R_k^{(-)}\right)^2}\left(\frac{dR_k^{(-)}}{d\lambda}\right)\right] \tag{A.13}$$

and

$$\frac{dR_k^{(+)}}{d\lambda} = \frac{\gamma_k\left[\alpha_k\left(\frac{dR_{k+2}^{(+)}}{d\lambda}\right) - \frac{1}{c^2}\right]}{\left[\beta_k + \alpha_k\left(R_{k+2}^{(+)}\right)\right]^2}. \tag{A.14}$$

Here, we employed the relation $d\beta_k/d\lambda = c^{-2}$. By matching boundary condition at $k = l - \Lambda$ ( i.e., $R_{l-\Lambda}^{(-)} = R_{l-\Lambda}^{(+)}$), all values of $R_k$ can now be obtained. In the present calculation, the following normalization condition [106] is used:

$$\sum_{k=0,1}^{\infty}{}' \frac{(k+2\Lambda)!}{k!} d_k^{\Lambda l}(c) = \frac{(l+\Lambda)!}{(l-\Lambda)!}, \tag{A.15}$$

which leads to $\lim_{\eta\to 1} S_{\Lambda l}(c,\eta) = P_l^{\Lambda}(\eta)$. For numerical purpose, Eq. (A.15) is writen in terms of $R_k$ as

$$\sum_{k=0,1}^{\infty}{}' \frac{(k+2\Lambda)!}{k!} d_k^{\Lambda l}(c) = d_{0,1}^{\Lambda l} \sum_{k=0,1}^{\infty}{}' \frac{(k+2\Lambda)!}{k!} \prod_{i=0,1}^{k}{}' R_i, \tag{A.16}$$

where $R_0 = R_1 \equiv 1$, and the prime sign indicates $k$ (or $i$) $= 0, 2, 4, ...$ for odd $(l - \Lambda)$ and $k$ (or $i$) $= 1, 3, 5, ...$ for even $(l - \Lambda)$. Finally, the coefficients $d_0$ and $d_1$ can be determined from Eqs. (A.16):

$$d_{0,1}^{\Lambda l} = \frac{(l+\Lambda)!}{(l-\Lambda)!} / \sum_{k=0,1}^{\infty}{}' \frac{(k+2\Lambda)!}{k!} \prod_{i=0,1}^{k}{}' R_i. \tag{A.17}$$

## A.3 Numerical Difficulties and Solutions

The method **(a)** discussed in Sec. A.2 is a straightfoward Hermitian eigenvalue problem, while the results of the method **(b)** are very sensitive to the accuracy of separation constant $\lambda_{\Lambda l}$. However, in the limit of low binding energies and/or large deformation, the technique based on method **(b)** is very useful when calculating radial wave functions.

For instance, the coefficients $d_k$ are, in general, largest in magnitude at $k = l - \Lambda$, and quickly decrease with $k$. On the other hand, the magnitudes of spherical Bessel functions of the third kind, $h_k^{(1)}(ic_{\mathrm{ext}}\xi)$, rapidly increase with $k$. Consequently, the product $d_k^{\Lambda l}(ic_{\mathrm{ext}})h_{k+\Lambda}^{(1)}(ic_{\mathrm{ext}}\xi)$ becomes numerically unstable at large values of $k$ if $d_k$ and $h_{k+\Lambda}^{(1)}$ are computed separately. The similar problem also occurs when calculating the radial spheroidal function of the first kind $R_{\Lambda l}^{(1)}(c, \xi)$ with large value of $(l - \Lambda)$. This problem can be overcome by writing the recurrence relation (A.8) in the form

$$\bar{\alpha}_k \bar{R}_{k+2} + \beta_k + \bar{\gamma}_k \bar{R}_k = 0, \tag{A.18}$$

where

$$\bar{\alpha}_k = \left(\frac{f_{k+\Lambda+2}}{f_{k+\Lambda}}\right)^{-1} \alpha_k, \quad \bar{\gamma}_k = \left(\frac{f_{k+\Lambda}}{f_{k+\Lambda-2}}\right)^{-1} \gamma_k, \quad \bar{R}_k = \frac{d_k f_{k+\Lambda}}{d_{k-2} a f_{k+\lambda-2}}, \tag{A.19}$$

and $f_k$ is the $k$th order spherical Bessel function. Employing the recurrence property of spherical Bessel functions $f_k(z)$

$$f_{k-1}(z) + f_{k+1}(z) = \frac{2k+1}{z} f_k(z), \tag{A.20}$$

the ratio of spherical Bessel functions $f_k/f_{k-2}$ can be expressed as

$$\frac{j_k}{j_{k-2}} = \left\{ \frac{4k^2-1}{z^2} - 1 - \frac{2k-1}{2k+3} \left[ 1 + \left( \frac{j_{k+2}}{j_k} \right)^{-1} \right] \right\}^{-1} \tag{A.21}$$

and

$$\frac{h^{(1)}_{k+2}}{h^{(1)}_k} = \frac{(2k+3)(2k+1)}{z^2} - 1 - \frac{2k+3}{2k-1} \left[ 1 + \left( \frac{h^{(1)}_k}{h^{(1)}_{k-2}} \right)^{-1} \right]. \tag{A.22}$$

It is to be noted that the above two equations (A.21) and (A.22) are needed to avoid the error propagation. For $f_k = h^{(1)}_k$, the ratios $f_k/f_{k-2}$ are to be calculated recursively starting from small values of $k$, whereas for $f_k = j_k$ they are to be evaluated starting from large values of $k$. Similarly, the first derivatives of radial spheroidal wave functions with respect to $\xi$ can be computed by replacing the spherical Bessel functions $f_k(z)$ [Eq. (A.19)] with their derivatives $f'_k(z) \equiv df_k(z)/dz$, using

$$\frac{f'_{k+2}}{f'_k} = -\left( \frac{f_{k+2}}{f_k} \right) \frac{1 + \left( \frac{f_{k+2}}{f_k} \right)^{-1} - \frac{1}{z^2}(2k+3)(k+3)}{1 + \left( \frac{f_{k+2}}{f_k} \right) - \frac{1}{z^2} k(2k+3)}. \tag{A.23}$$

The algorithm for calculating the products $d^{\Lambda l}_k(c) f_{k+\Lambda}(c\xi)$ and $d^{\Lambda l}_k(c) f'_{k+\Lambda}(c\xi)$ follows method **(b)**. Numerical accuracy of calculating spherical Bessel functions with large arguments can also be achieved by applying this method.

# Appendix B

# Properties of Spheroidal Orbitals in the limit of low binding energy

In this Appendix, properties of deformed orbitals of the spheroidal well are examined at the limit of small binding energy. The general properties of deformed orbitals are investigated in terms of the multipole expansion in Sec. 3.2, and the relevant numerical examples are presented in Sec. 4.3. Here, we demonstrate that the analytic expressions obtained in Sec. 3.2 can also be obtained by analyzing the exact spheroidal wave functions of Eq. (4.17). It is shown that the spheroidal wave functions have rather similar properties in the limit of *both* small deformation and binding energy ($c_{\text{ext}} \rightarrow 0$).

## B.1 Some Properties of Weakly Bound Orbitals in Spheroidal Well

In this section, average values of the mean square radius and quadrupole moment in deformed orbital are discussed by considering an explicit form of spheroidal wave functions. In terms of spheroidal coordinates, the volume element $dV$, square radius $r^2$, and quadrupole moment $r^2Y_{20}$ are expressed as:

$$dV = dxdydz = a^3(\xi^2 - \eta^2)d\xi d\eta d\phi, \tag{B.1}$$

$$r^2 = x^2 + y^2 + z^2 = a^2(\xi^2 + \eta^2 - 1), \tag{B.2}$$

and

$$r^2Y_{20}(\theta,\phi) = \sqrt{\frac{5}{16\pi}}(3z^2 - r^2) = \sqrt{\frac{5}{16\pi}}a^2(3\xi^2\eta^2 - \xi^2 - \eta^2 + 1). \tag{B.3}$$

As discussed in Sec. 3.2, the asymptotic behavior of radial and multipole moments is mainly determined by the asymptotic structure of wave functions. Therefore, it is instructive to consider the $n$th external radial integral

$$O_{\nu\Lambda nll'} \equiv B^*_{\nu\Lambda l}B_{\nu\Lambda l'}\int_{\xi_0}^{+\infty} R^{(3)*}_{\Lambda l}(ic_{\rm ext},\xi)\xi^n R^{(3)}_{\Lambda l'}(ic_{\rm ext},\xi)d\xi. \tag{B.4}$$

In the small-$\epsilon$ limit, the amplitudes $B_{\nu\Lambda l}$ determined from Eq.(A.1) behave as

$$B_{\nu\Lambda l} = \frac{\sum_{l'}^{\infty}{}' A_{\nu\Lambda l'}R^{(1)}_{\Lambda l'}(c_{\rm int},\xi_0)\langle S^{(1)}_{\Lambda l}(ic_{\rm ext},\eta)|S^{(1)}_{\Lambda l'}(c_{\rm int},\eta)\rangle}{R^{(3)}_{\Lambda l}(ic_{\rm ext},\xi_0)\langle S^{(1)}_{\Lambda l}(ic_{\rm ext},\eta)|S^{(1)}_{\Lambda l}(ic_{\rm ext},\eta)\rangle} \propto c^{l+1}_{\rm ext}. \tag{B.5}$$

Since in the limit of small $c$ the expansion coefficients $d^{\Lambda l}_k(c)$ behave as

$$\lim_{c\to 0} d^{\Lambda l}_k(c) = \delta_{k,l-\Lambda}, \tag{B.6}$$

in the limit of low binding energy the radial spheroidal wave functions of the third kind $R^{(3)}_{\Lambda l}(ic_{\rm ext},\xi)$ behave as spherical Hankel function of the first kind $h^{(1)}_l(ic_{\rm ext}\xi)$. At small values of $\epsilon$, the radial integral $O_{\nu\Lambda nll'}$ can be written as

$$
\begin{aligned}
O_{\nu\Lambda nll'} &\cong c_{\rm ext}^{l+l'+2}\int_{\xi_0}^{+\infty}\left[\xi^n-\xi^{n-2}+\cdots\right]h_l^{(1)*}(ic_{\rm ext}\xi)h_{l'}^{(1)}(ic_{\rm ext}\xi)d\xi && \text{(B.7)}\\
&= c_{\rm ext}^{l+l'+1}\int_{c_{\rm ext}\xi_0}^{+\infty}\left[\left(\frac{x}{c_{\rm ext}}\right)^n-\left(\frac{x}{c_{\rm ext}}\right)^{n-2}+\cdots\right]h_l^{(1)*}(ix)h_{l'}^{(1)}(ix)dx && \text{(B.8)}\\
&= c_{\rm ext}^{l+l'+1-n}\frac{(i)^{l-l'}}{2^{l+l'}}\left(l+\frac{1}{2},l\right)\left(l'+\frac{1}{2},l'\right)\\
&\quad\times\left[\int_{c_{\rm ext}\xi_0}^{c_{\rm ext}\xi_0+\Delta}x^{n-l-l'-2}dx-c_{\rm ext}^2\int_{c_{\rm ext}\xi_0}^{c_{\rm ext}\xi_0+\Delta}x^{n-l-l'-4}dx+\cdots\right] && \text{(B.9)}\\
&= c_{\rm ext}^{l+l'+1-n}\frac{(i)^{l-l'}}{2^{l+l'}}\left(l+\frac{1}{2},l\right)\left(l'+\frac{1}{2},l'\right)\\
&\quad\times\left[\left\{\begin{array}{ll}\text{const.}-\frac{(c_{\rm ext}\xi_0)^{n-l-l'-1}}{n-l-l'-1} & \text{for } n-l-l'\neq 1\\ -\ln(c_{\rm ext}\xi_0) & \text{for } n-l-l'=1\end{array}\right\}\right.\\
&\quad\left.-c_{\rm ext}^2\times\left\{\begin{array}{ll}\text{const.}-\frac{(c_{\rm ext}\xi_0)^{n-l-l'-3}}{n-l-l'-3} & \text{for } n-l-l'\neq 3\\ -\ln(c_{\rm ext}\xi_0) & \text{for } n-l-l'=3\end{array}\right\}+\cdots\right]. && \text{(B.10)}
\end{aligned}
$$

Finally, the following asymptotic limits can be deduced from Eqs.(B.10) and (B.5):

$$
\lim_{\epsilon_\nu\to 0}O_{\nu\Lambda nll'}\propto\left\{\begin{array}{ll}(-\epsilon_\nu)^{-(n-l-l'-1)/2} & \text{for } n-l-l'-1>0\\ \ln(-\epsilon_\nu) & \text{for } n-l-l'-1=0\\ \text{finite} & \text{for } n-l-l'-1<0\end{array}\right. . \qquad \text{(B.11)}
$$

The asymptotic behavior of the normalization constant $\mathcal{N}_{\nu\Lambda\pi}$ can be easily evaluated:

$$
\begin{aligned}
\mathcal{N}^2_{\nu\Lambda\pi} &\equiv \langle\psi_{\nu\Lambda\pi}(\xi,\eta,\phi)|\psi_{\nu\Lambda\pi}(\xi,\eta,\phi)\rangle && \text{(B.12)}\\
&= \int_{\xi_0}^{+\infty}d\xi\int_0^{\pi}d\eta\int_0^{2\pi}d\phi\psi^*_{\nu\Lambda\pi}(\xi,\eta,\phi)\psi_{\nu\Lambda\pi}(\xi,\eta,\phi)a^3(\xi^2-\eta^2)\\
&\quad+\int_1^{\xi_0}d\xi\int_0^{\pi}d\eta\int_0^{2\pi}d\phi\psi^*_{\nu\Lambda\pi}(\xi,\eta,\phi)\psi_{\nu\Lambda\pi}(\xi,\eta,\phi)a^3(\xi^2-\eta^2) && \text{(B.13)}
\end{aligned}
$$

$$= a^3 \sum_{l,l'}{}' B^*_{\nu\Lambda l} B_{\nu\Lambda l'} \left[ \int_{\xi_0}^{+\infty} R^{(3)*}_{l\Lambda}(ic_{\text{ext}},\xi)\xi^2 R^{(3)}_{l'\Lambda}(ic_{\text{ext}},\xi) d\xi \bar{S}_{\Lambda 0 l l'}(ic_{\text{ext}}) \right.$$

$$\left. - \int_{\xi_0}^{+\infty} R^{(3)*}_{l\Lambda}(ic_{\text{ext}},\xi) R^{(3)}_{l'\Lambda}(ic_{\text{ext}},\xi) d\xi \bar{S}_{\Lambda 2 l l'}(ic_{\text{ext}}) \right] + \text{const.} \tag{B.14}$$

$$= a^3 \sum_{l,l'}{}' \left[ O_{\nu\Lambda 2 l l'} \bar{S}_{\Lambda 0 l l'}(ic_{\text{ext}}) - O_{\nu\Lambda 0 l l'} \bar{S}_{\Lambda 2 l l'}(ic_{\text{ext}}) \right] + \text{const.}, \tag{B.15}$$

where $\bar{S}_{\Lambda n l l'}(c) \equiv \langle S^{(1)}_{l\Lambda}(c,\eta) | \eta^n | S^{(1)}_{l'\Lambda}(c,\eta) \rangle$. Since only diverging element in Eq.(B.15) is $O_{\nu 0200}$, one obtains

$$\lim_{\epsilon_\nu \to 0} \mathcal{N}^2_{\nu\Lambda\pi} \propto \begin{cases} (-\epsilon_\nu)^{-1/2} & \text{for } \pi = +, \Lambda = 0 \\ \text{finite} & \text{otherwise} \end{cases} . \tag{B.16}$$

Similarly, the average value of the 2nd radial moment $\langle \nu\Lambda\pi | r^2 | \nu\Lambda\pi \rangle$ can be written as

$$\langle \nu\Lambda\pi | \; r^2 \; | \nu\Lambda\pi \rangle \equiv \frac{\langle \psi_{\nu\Lambda\pi}(\xi,\eta,\phi) | r^2 | \psi_{\nu\Lambda\pi}(\xi,\eta,\phi) \rangle}{\mathcal{N}^2_{\nu\Lambda\pi}} \tag{B.17}$$

$$= \frac{a^5}{\mathcal{N}^2_{\nu\Lambda\pi}} \left[ \int_1^{\xi_0} d\xi \int_0^{\pi} d\eta \int_0^{2\pi} d\phi |\psi_{\nu\Lambda\pi}(\xi,\eta,\phi)|^2 (\xi^4 - \eta^4) \right.$$

$$\left. + \int_{\xi_0}^{+\infty} d\xi \int_0^{\pi} d\eta \int_0^{2\pi} d\phi |\psi_{\nu\Lambda\pi}(\xi,\eta,\phi)|^2 (\xi^4 - \eta^4) \right] - a^2 \tag{B.18}$$

$$= \frac{a^5}{\mathcal{N}^2_{\nu\Lambda\pi}} B^*_{\nu\Lambda l} B_{\nu\Lambda l'} \sum_{l,l'}{}' \left[ \int_{\xi_0}^{+\infty} R^{(3)*}_{l\Lambda}(ic_{\text{ext}},\xi)\xi^4 R^{(3)}_{l'\Lambda}(ic_{\text{ext}},\xi) d\xi \; \bar{S}_{\Lambda 0 l l'}(ic_{\text{ext}}) \right.$$

$$\left. - \int_{\xi_0}^{+\infty} R^{(3)*}_{l\Lambda}(ic_{\text{ext}},\xi) R^{(3)}_{l'\Lambda}(ic_{\text{ext}},\xi) d\xi \bar{S}_{\Lambda 4 l l'}(ic_{\text{ext}}) \right] + \text{const.} \tag{B.19}$$

$$= \frac{a^5}{\mathcal{N}^2_{\nu\Lambda\pi}} \sum_{l,l'}{}' \left[ O_{\nu\Lambda 4 l l'} \bar{S}_{\Lambda 0 l l'}(ic_{\text{ext}}) - O_{\nu\Lambda 0 l l'} \bar{S}_{\Lambda 4 l l'}(ic_{\text{ext}}) \right] + \text{const.} \tag{B.20}$$

Since the zeroth radial integral $O_{\nu\Lambda 0 l l'}$ remains finite, the only diverging elements are $O_{\nu\Lambda 4 l l'}$ and

$$\langle \nu\Lambda\pi | r^2 | \nu\Lambda\pi \rangle = \frac{a^5}{\mathcal{N}^2_{\nu\Lambda\pi}} \sum_{l,l'}{}' O_{\nu\Lambda 4 l l'} \bar{S}_{\Lambda 0 l l'}(ic_{\text{ext}}) + \text{const.}. \tag{B.21}$$

Using the asymptotic expressions for $O_{\nu\Lambda nll'}$ [Eq. (B.11)] and $\mathcal{N}^2_{\nu\Lambda\pi}$ [Eq. (B.16)], one obtains

$$\lim_{\epsilon_\nu \to 0} \langle \nu\Lambda\pi | r^2 | \nu\Lambda\pi \rangle \propto \begin{cases} (-\epsilon_\nu)^{-1} & \text{for } \pi = +, \Lambda = 0 \\ (-\epsilon_\nu)^{-1/2} & \text{for } \pi = -, \Lambda = 0 \text{ or } 1 \\ \text{finite} & \text{otherwise} \end{cases} \cdot \tag{B.22}$$

The quadrupole moment $\langle \nu\Lambda\pi | r^2 Y_{20} | \nu\Lambda\pi \rangle$ can be expressed as

$$\langle \nu\Lambda\pi | \; r^2 \; Y_{20} | \nu\Lambda\pi \rangle \equiv \frac{\langle \psi_{\nu\Lambda\pi}(\xi,\eta,\phi) | r^2 Y_{20} | \psi_{\nu\Lambda\pi}(\xi,\eta,\phi) \rangle}{\mathcal{N}^2_{\nu\Lambda\pi}} \tag{B.23}$$

$$= \frac{3a^5}{\mathcal{N}^2_{\nu\Lambda\pi}} \sqrt{\frac{5}{16\pi}} \int_1^{+\infty} d\xi \int_0^{\pi} d\eta \int_0^{2\pi} d\phi |\psi_{\nu\Lambda\pi}(\xi,\eta,\phi)|^2 (\xi^4\eta^2 - \xi^2\eta^4) \tag{B.24}$$

$$-\sqrt{\frac{5}{16\pi}} \langle \nu\Lambda\pi | r^2 | \nu\Lambda\pi \rangle \tag{B.25}$$

$$= \frac{3a^5}{\mathcal{N}^2_{\nu\Lambda\pi}} \sqrt{\frac{5}{16\pi}} \left[ \int_1^{\xi_0} d\xi \int_0^{\pi} d\eta \int_0^{2\pi} d\phi |\psi_{\nu\Lambda\pi}(\xi,\eta,\phi)|^2 (\xi^4\eta^2 - \xi^2\eta^4) \right.$$
$$\left. + \int_{\xi_0}^{+\infty} d\xi \int_0^{\pi} d\eta \int_0^{2\pi} d\phi |\psi_{\nu\Lambda\pi}(\xi,\eta,\phi)|^2 (\xi^4\eta^2 - \xi^2\eta^4) \right]$$
$$-\sqrt{\frac{5}{16\pi}} \langle \nu\Lambda\pi | r^2 | \nu\Lambda\pi \rangle \tag{B.26}$$

$$= \frac{a^5}{\mathcal{N}^2_{\nu\Lambda\pi}} \sqrt{\frac{5}{16\pi}} \left\{ 3 \sum_{l,l'}{}' \left[ O_{\nu\Lambda 4ll'} \bar{S}_{\Lambda 2ll'}(ic_{\text{ext}}) - O_{\nu\Lambda 2ll'} \bar{S}_{\Lambda 4ll'}(ic_{\text{ext}}) \right] \right.$$
$$\left. - \sum_{l,l'}{}' \left\{ O_{\nu\Lambda 4ll'} \bar{S}_{\Lambda 0ll'}(ic_{\text{ext}}) - O_{\nu\Lambda 0ll'} \bar{S}_{\Lambda 4ll'}(ic_{\text{ext}}) \right\} + \text{const.} \right\} \tag{B.27}$$

$$= \frac{a^5}{\mathcal{N}^2_{\nu\Lambda\pi}} \sqrt{\frac{5}{16\pi}} \left\{ \sum_{l,l'}{}' O_{\nu\Lambda 4ll'} \left[ 3\bar{S}_{\Lambda 2ll'}(ic_{\text{ext}}) - \bar{S}_{\Lambda 0ll'}(ic_{\text{ext}}) \right] \right.$$
$$\left. - 3 \sum_{l,l'}{}' O_{\nu\Lambda 2ll'} \bar{S}_{\Lambda 4ll'}(ic_{\text{ext}}) + \sum_{l,l'}{}' O_{\nu\Lambda 0ll'} \bar{S}_{\Lambda 4ll'}(ic_{\text{ext}}) + \text{const.} \right\} . \tag{B.28}$$

For a positive-parity halo orbital, the only diverging elements in Eq. (B.28) are the terms with $O_{\nu 0400}$, $O_{\nu 0200}$, $O_{\nu 0420}$, and $O_{\nu 0402}$. However, since

$$3\bar{S}_{0200}(ic_{\text{ext}}) - \bar{S}_{0000}(ic_{\text{ext}}) \stackrel{c_{\text{ext}} \to 0}{\longrightarrow} 3\langle P_0(\eta) | \eta^2 | P_0(\eta) \rangle - \langle P_0(\eta) | P_0(\eta) \rangle = 0, \tag{B.29}$$

the term containing $O_{\nu 0400}$ vanishes. According to the asymptotic limit (B.11), in the limit of small binding the terms containing $O_{\nu 0200}$, $O_{\nu 0420}$, and $O_{\nu 0402}$ behave as $(-\epsilon_\nu)^{-1/2}$. Since $\mathcal{N}_{\nu 0+}^2$ also diverges as $(-\epsilon_\nu)^{-1/2}$, the quadrupole moment for positive-parity halos remains finite at vanishing values of $\epsilon_\nu$.

On the other hand, the quadrupole moment of negative-parity halo orbitals diverges due to the presence of the $O_{\nu\Lambda 411}$ term. Keeping only the diverging elements in Eq.(B.28), one obtains

$$\langle \nu\Lambda - | \, r^2 Y_{20} \, | \nu\Lambda - \rangle \to \frac{a^5}{\mathcal{N}_{\nu\Lambda-}^2} \sqrt{\frac{5}{16\pi}} O_{\nu\Lambda 411} \left[ 3\bar{S}_{\Lambda 211}(ic_{\text{ext}}) - \bar{S}_{\Lambda 011}(ic_{\text{ext}}) \right] \tag{B.30}$$

$$= \sqrt{\frac{5}{16\pi}} \left[ \frac{a^5}{\mathcal{N}_{\nu\Lambda-}^2} O_{\nu\Lambda 411} \bar{S}_{\Lambda 011}(ic_{\text{ext}}) \right] \left[ \frac{3\bar{S}_{\Lambda 211}(ic_{\text{ext}})}{\bar{S}_{\Lambda 011}(ic_{\text{ext}})} - 1 \right] \tag{B.31}$$

$$= \frac{1}{\sqrt{5\pi}} \left( \lim_{c_{\text{ext}} \to 0} \langle \nu\Lambda - | r^2 | \nu\Lambda - \rangle \right) \left( 1 - \frac{3}{2}\Lambda^2 \right). \tag{B.32}$$

Therefore,

$$\lim_{\epsilon_\nu \to 0} \langle \nu\Lambda\pi | r^2 Y_{20} | \nu\Lambda\pi \rangle \propto \begin{cases} (-\epsilon_\nu)^{-1/2} & \text{for } \pi = -, \Lambda = 0 \text{ or } 1 \\ \text{finite} & \text{otherwise} \end{cases} \tag{B.33}$$

and

$$\lim_{\epsilon_\nu \to 0} \beta_2(\nu\Lambda\pi) = \begin{cases} 0 & \text{for } \pi = +, \Lambda = 0 \\ \frac{4}{5}\sqrt{\frac{\pi}{5}} \left(1 - \frac{3}{2}\Lambda^2\right) & \text{for } \pi = -, \Lambda = 0 \text{ or } 1 \end{cases} . \tag{B.34}$$

Of course, the above results coincide with those of Chapter 3.

## B.2 Radial Form Factors

The radial form factors $R_{\nu l\Lambda}(r)$

$$R_{\nu\ell\Lambda}(r) = \frac{1}{\mathcal{N}_{\nu\Lambda\pi}} \int Y_{\ell\Lambda}^*(\theta, \phi) \psi_{\nu\Lambda\pi}(\vec{r}) d\Omega \tag{B.35}$$

are useful to examine the spatial extention and the multipole decomposition of deformed halo wave functions $\psi_{\nu\Lambda\pi}(\vec{r})$ [Eq. (3.2)]. With decreasing binding energy, the external part ($\xi > \xi_0$) of deformed wave function $\psi_{\nu\Lambda\pi}(\vec{r})$ takes a simple form

$$\psi_{\nu\Lambda\pi}(\xi,\eta,\phi) \rightarrow \frac{1}{\sqrt{2\pi}}\left(\frac{\xi^2-1}{\xi^2}\right)^{\Lambda/2} \sum_l{}' B_{\nu\Lambda l} h_l^{(1)}(ic_{\rm ext}\xi) P_l^\Lambda(\eta) e^{\pm\Lambda\phi}. \tag{B.36}$$

For large values of $\xi$, one can put

$$r = a\sqrt{\xi^2+\eta^2-1} \rightarrow a\xi, \tag{B.37}$$

$$\cos\theta = \frac{a\xi\eta}{r} \rightarrow \eta, \tag{B.38}$$

and, consequently,

$$R_{\nu\ell\Lambda}(r) \cong \frac{(-1)^\Lambda}{\mathcal{N}_{\nu\Lambda\pi}} \sum_l{}' \sqrt{\frac{2\ell+1}{2}\frac{(\ell-\Lambda)!}{(\ell+\Lambda)!}} B_{\nu\Lambda l} h_l^{(1)}(ic_{\rm ext}r/a) \langle P_\ell^\Lambda(\eta)|P_l^\Lambda(\eta)\rangle \tag{B.39}$$

$$\propto \frac{B_{\nu\Lambda\ell}}{\mathcal{N}_{\nu\Lambda\pi}}\frac{e^{-c_{\rm ext}r}}{r} \propto (-\epsilon_\nu)^{\ell/2+\frac{1}{4}\delta_{\ell,0}}/r. \tag{B.40}$$

This expression indicates that at large distances the amplitudes of radial form factors are proportional to $(-\epsilon_\nu)^{\ell/2+\frac{1}{4}\delta_{\ell,0}}$. This also suggests that the $\ell = 0$ partial wave has the largest spatial extention and thus exhibits the most pronounced halo effect.

Similarly, the probability to find the partial wave $\ell$ in the state $[\nu\Lambda\pi]$, Eq. (4.22), can be written as

$$P_\ell(\nu\Lambda\pi) = \int_0^{+\infty} |R_{\nu\ell}(r)|^2 r^2 dr \tag{B.41}$$

$$= \frac{1}{\mathcal{N}_{\nu\Lambda\pi}^2}\left\{\int_0^{r_\gg} r^2 dr \left|\int Y_{\ell\Lambda}^*(\theta,\phi)\psi_{\nu\Lambda\pi}(\vec{r})d\Omega\right|^2 + \int_{r_\gg}^{+\infty} r^2 dr \left|\int Y_{\ell\Lambda}^*(\theta,\phi)\psi_{\nu\Lambda\pi}(\vec{r})d\Omega\right|^2\right\}, \tag{B.42}$$

where $r_{\gg}$ denotes a large, but arbitrary, value of $r$. At the limit of low binding energy, one obtains

$$
\begin{aligned}
P_\ell(\nu\Lambda\pi) &\cong \frac{1}{\mathcal{N}^2_{\nu\Lambda\pi}}\left[\int_{\xi_{\gg}}^{+\infty}\left|B_{\nu\Lambda\ell}h_\ell^{(1)}(ic_{\rm ext}\xi)\right|^2 a^3\xi^2 d\xi + \text{const.}\right] && \text{(B.43)}\\
&\cong \frac{1}{\mathcal{N}^2_{\nu\Lambda\pi}}\left(\mathcal{N}^2_{\nu 0+}\delta_{\ell,0} + \text{const.}\right) && \text{(B.44)}\\
&= \begin{cases} \delta_{\ell,0} & \text{for } \pi=+, \Lambda=0 \\ \text{finite } (<1) & \text{otherwise} \end{cases} . && \text{(B.45)}
\end{aligned}
$$

According to this asymptotic limit, for positive-parity halo orbitals an $s$-wave component dominates, whereas the negative-parity halo orbitals consist of all partial waves even at very small binding energies. Figures 4.14 and 4.15 illustrate this effect quantitatively.

# Appendix C

# Examples of Deformed Single-Particle Wave Functions

This section contains graphic representations of deformed single-particle wave functions of a finite square-well model of Chapter 4. The wave functions shown in Fig. C.1 were calculated at $U_0 = -45$ MeV and $\delta = 0.6$.

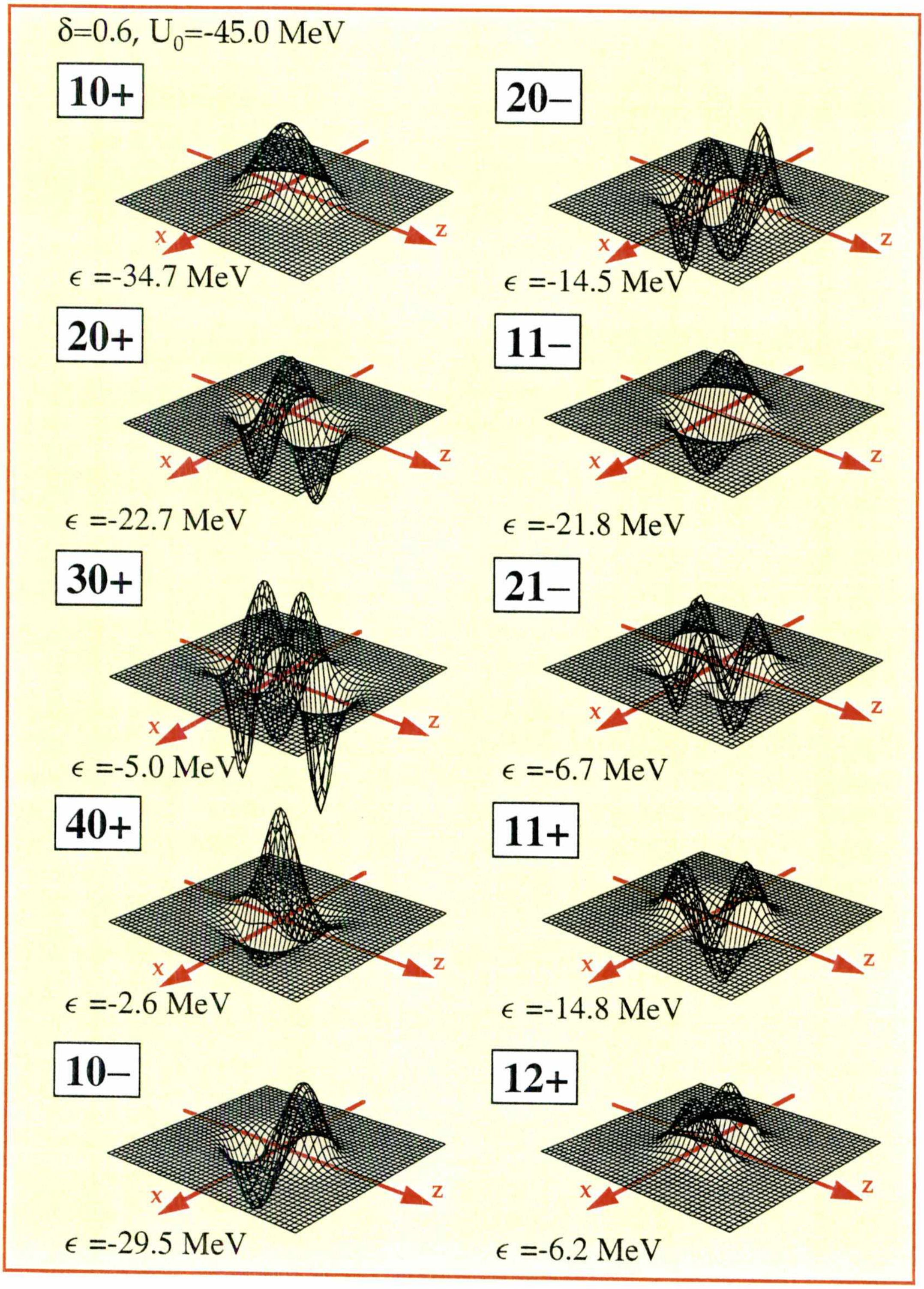


**Figure C.1**: Deformed single-particle wave functions, projected onto $x$-$z$ plane, obtained for a finite square-well model of Chapter 4 ($U_0 = -45$ MeV, $\delta = 0.6$).

# Vita

**Toshiyuki "Max" Misu** was born in Hiroshima, Japan on December 5, 1965. He first came to United States in the summer of 1985, after thirteen years of attending Japanese school systems. He graduated from Pacific University, Forest Grove, Oregon in May, 1988 with Bachelor of Science degree in Physics. He returned to Hiroshima and worked for Miyoshi Electronics Corporation from 1988 to 1990. As an engineer, he developed and gained a patent for one of the most advanced commercial technologies, the Auto Vehicle Monitor (known as AVM system). This design was the first of its kind using phase-modulated pseudo-random EM signals at high frequency (1 GHz). Because of his strong interest in fundamental physics, he entered the Master's program in Physics at the University of Tennessee in September of 1990, and received Master of Science degree in May, 1992. He continued the doctoral program at the University of Tennessee and worked with Dr. W. Nazarewicz at Oak Ridge National Laboratory. His research focus has been the study of nuclear structure near particle drip lines (the present dissertation topic).